Production Cross Sections of J/Ψ(1S) and Υ(1S) at $\sqrt{s}$ = 7 TeV with CMS

von Sarah Beranek

Diplomarbeit in Physik
vorgelegt der

Fakultät für Mathematik, Informatik und Naturwissenschaften
der Rheinisch-Westfälischen Technischen Hochschule Aachen

im April 2011 angefertigt im
I. Physikalischen Institut (IB)
bei Prof. Dr. Stefan Schael

Abstract

Measurements of the production cross sections of $J/\Psi(1S)$ and $\Upsilon(1S)$ resonances in the dimuon channel in proton-proton collisions with a $\sqrt{s} = 7$ TeV at the CMS experiment at LHC (CERN) are presented. The efficiencies are obtained via data driven methods. The differential cross sections are presented as a function of the transverse momentum. The total inclusive $J/\Psi(1S)$ production cross section for an integrated luminosity of 36 pb^{-1} is measured with $(50.61 \pm 0.04_{stat} \pm 3.09_{sys} \pm 2.02_{lumi})$ nb for a transverse momentum between 8 and 30 GeV/c and a rapidity range of $|y| < 2.4$. The total production cross section for the $\Upsilon(1S)$ resonance is measured for an integrated luminosity of 36 pb^{-1} in the rapidity range of $|y| < 2.0$ and a transverse momentum range between 3 and 30 GeV/c with $(4.96 \pm 0.06_{stat} \pm 0.47_{sys} \pm 0.20_{lumi})$ nb.

Zusammenfassung

Es werden Messungen des Produktionswirkungsquerschnittes der $J/\Psi(1S)$ und $\Upsilon(1S)$ Resonanzen in zwei Muonen in Proton-Proton Kollisonen mit $\sqrt{s} = 7$ TeV am CMS Experiment des LHC (CERN) präsentiert. Die Effizienzen werden mit auf Daten beruhenden Methoden bestimmt. Die differentiellen Wirkungsquerschnitte werden in Abhängigkeit des Transversalimpulses präsentiert. Der totale inklusive $J/\Psi(1S)$ Produktionswirkungsquerschnitt ist für eine integrierte Luminosität von 36 pb^{-1} mit $(50.61 \pm 0.04_{stat} \pm 3.09_{sys} \pm 2.02_{lumi})$ nb mit einen Transversalimpuls zwischen 8 und 30 GeV/c und in einem Rapiditätsbereich von $|y| < 2.4$ gemessen worden. Der totale inklusive Produktionswirkungsquerschnitt für die $\Upsilon(1S)$ Resonanz wurde für eine integrierte Luminosität von 36 pb^{-1} für $|y| < 2.0$ und einem Transversalimpuls zwischen 3 und 30 GeV/c mit $(4.96 \pm 0.06_{stat} \pm 0.47_{sys} \pm 0.20_{lumi})$ nb bestimmt.

Contents

CHAPTER 1

Introduction

The discovery of the $J/\Psi(1S)$ resonance was announced on November 11th, 1974 simultaneously at the BNL (Brookhaven National Laboratory) [1] and the SLAC (Stanford Linear Accelerator Center) [2]. This paved the path for a revolutionary change in the understanding of quarks and their interactions. The discovery confirmed the existence of the charmed quark, which had been predicted ten years earlier [3] and fullfilled the need for unifying the electromagnetic and the weak forces [4, 5]. This was one of the many accomplishments that guided the completion of the standard model (SM) of particle physics in the 1970's.

Despite of its remarkable success, the SM leaves several unanswered questions: What is mass and how do particles get mass? Why is there more matter than antimatter in our universe? What is dark matter made of?

The first proton-proton collisions at a center of mass energy of $\sqrt{s} = 7\ \text{TeV}$ took place on March 30th, 2010 at the Large Hadron Collider. The $J/\Psi(1S)$ and also the $\Upsilon(1S)$ resonance are studied, because none of the theoretical approaches describe both the differential cross sections and the polarization simultaneously, which have been measured in previous experiments [6–8]. Expanding to higher energy and larger transverse momentum regions of the $J/\Psi(1S)$ and $\Upsilon(1S)$, the LHC provides an important instrument on the way to the clarification of these production mechanisms in hadronic collisions. Moreover $J/\Psi(1S)$ and $\Upsilon(1S)$ are important standard candles, which are used for efficiency measurements, alignment and detector calibration in this early stage of data taking at the LHC.

In this diploma thesis a measurement of the differential and total cross section of the $J/\Psi(1S)$ and $\Upsilon(1S)$ resonances in the dimuon channel is presented. The data was taken by the CMS experiment at LHC during 2010 and corresponds to an integrated luminosity of 36 pb^{-1} .

After a short theoretical introduction of the particles under study, an overview of the Large Hadron Collider and the CMS experiment is shown. In the following chapters the event and data selection for this analysis and the quantities needed to obtain the cross sections are described. All efficiencies are determined using the data driven tag and probe method. The resulting cross section depends on the polarization of the $J/\Psi(1S)$ and $\Upsilon(1S)$ meson. In this analysis the unpolarized production scenario is used for the kinematical detector acceptance obtained via Monte Carlo Simulations. The resulting cross sections are compared to former CMS results, which were performed with less integrated luminosity. Additional the differential cross sections are compared to theoretical predictions from next to leading order non-relativistic quantumchromodynamic calculations.

CHAPTER 2

Theory

This analysis focuses on the dimuon decay of $J/\Psi(1S)$ and $\Upsilon(1S)$ mesons. Therefore some general aspects of these mesons and their properties are discussed in this chapter.

2.1 The Charmonium and the Bottomonium

Quarkonia are mesons (two quark bound states), which consist of a quark and the corresponding anti-quark. At BNL the $J/\Psi(1S)$ was discovered measuring the e^-e^+ mass spectrum in the reaction $p + \mathrm{Be} \rightarrow e^+ + e^- + X$ with a mass of 3.1 GeV/c^2 and a mass resolution of 20 MeV/c^2 [1]. Simultaneously at the Stanford Positron Electron Asymmetric Ring (Spear) at SLAC the $J/\Psi(1S)$ was discovered with a mass of 3.105 ± 0.003 GeV and an upper limit to the full width at half-maximum (FWHM) of 1.3 MeV [2]. Here it was quickly identified as the 1^3S_1 state of the charmonium ($c\bar{c}$), hence it was produced through a virtual photon: $e^+ + e^- \rightarrow \gamma \rightarrow J/\Psi(1S)$. The $J/\Psi(1S)$ therefore has the same quantum numbers as the photon, e.g. Spin 1, and can not be the ground state of the charmonium. In Table 2.1 the properties of the $J/\Psi(1S)$ and the $\Upsilon(1S)$ are shown. The dominant part of the $J/\Psi(1S)$ decay is hadronically ($87.7 \pm 0.5\%$). The studied decays into leptons have branching ratios of $5.94 \pm 0.06\%$ for electrons and $5.93 \pm 0.06\%$ for muons respectively [9]. The unusual long lifetime of the $J/\Psi(1S)$ of 10^{-20} s needed a new theoretical approach for its explanation. Strong interactions have lifetimes of 10^{-23} s (compared to 10^{-16} s for electromagnetic and 10^{-13} s to 15 min for weak decays). An explanation was proposed by Okuba, Zweig and Iizuba and resulted in the OZI-rule. The OZI rules states: if a Feynman diagram can be separated in two pieces only by

	quarks	mass	width	J^{PC}	$^{2S+1}L_J$
J/Ψ(1S)	$c\bar{c}$	3096.916 ± 0.011 MeV/c^2	92.9 ± 2.8 keV/c^2	1^{--}	1^3S_1
ϒ(1S)	$b\bar{b}$	9460.3 ± 0.26 MeV/c^2	54.02 ± 1.25 keV/c^2	1^{--}	1^3S_1

Table 2.1: *Properties of the J/Ψ(1S) and ϒ(1S) mesons, where J is the total angular momentum, S the total spin and L the total orbital quantum number. P and C refer to the parity and the charge symmetry. The mass and width values are the world average [9].*

cutting gluon lines, this process is not forbidden, but suppressed (see Fig. 2.1 a). The suppressed channel, related to the asymptotic freedom, must have high energetic gluons (*hard* gluons) and hence a weaker coupling. Instead the OZI-allowed processes are typically of low energy (*soft* gluons) with a stronger coupling. In Fig. 2.1 a) the energetically favored decay of a J/Ψ(1S) in three π mesons is pictured. This decay is OZI-suppressed due to the cutable gluon lines. The process shown in Fig. 2.1 b) J/Ψ(1S) → $D^+ + D^-$ is kinematically forbidden, because the combined mass of the D mesons is larger than the J/Ψ(1S) meson mass. Both effects lead to a lifetime of 10^{-20} s of the J/Ψ(1S) meson [5].

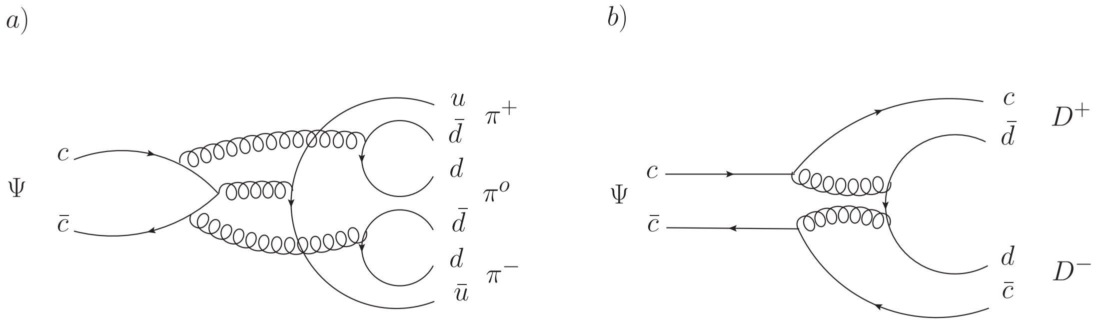

Figure 2.1: *Charmonium: a) OZI-suppressed decay below $D\bar{D}$ threshold, b) kinematical allowed decay for charmonium states only above $D\bar{D}$ threshold, when the decaying particle mass is larger than the sum of the D mesons mass.*

In 1976 the prediction had been made by Eichten and Gottfried, that the bottomonium ($b\bar{b}$) features a richer hierarchy of bound states (up to n = 3) than the charmonium due to the larger mass of the b quark, which is more than 2 times heavier than the charm quark [10]. One year later the ϒ(1S) was discovered at Fermilab in 400 GeV proton-nucleus collisions and measured with a mass of 9.54 ± 0.04 GeV and a FWHM of 0.5 ± 0.1 GeV . The resonance was also quickly interpreted as the 1^3S_1 state [11]. The ϒ(1S) meson decays mostly hadronically with ≈ 87% branching ratio. The leptonic decay channel divides into the electron channel with 2.48 ± 0.07%, the tau channel with 2.60 ± 0.10% and the dimuon channel with 2.48 ± 0.05% [9].

In Fig. 2.2 and 2.3 the spectrum of energy levels of charmonium and bottomonium are

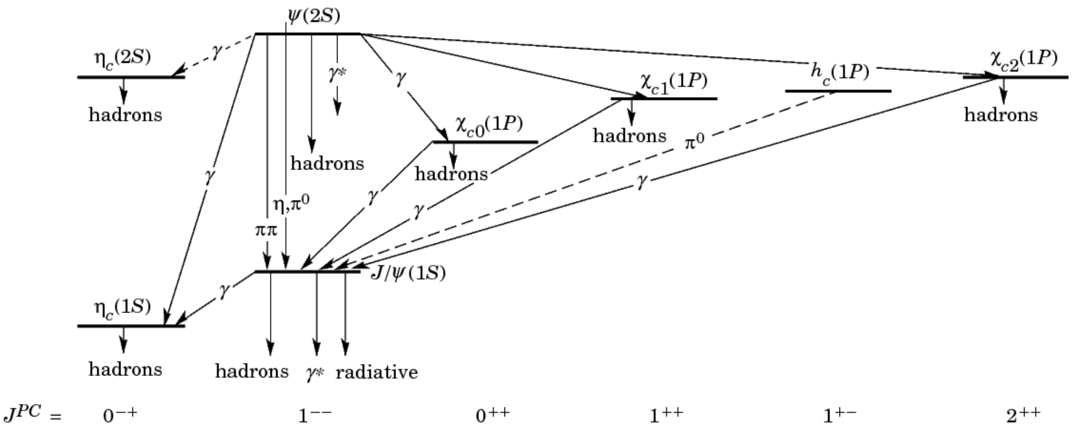

Figure 2.2: *Spectrum of energy levels of charmonium [9].*

shown with their possible decay modes. The level spacing between the charmonium and the bottomonium systems are remarkably similar. The J/Ψ(1S) and the Υ(1S) meson are the lowest possible state with the total angular momentum 1. For charmonium states with n≥3 the kinematically forbidden D meson production can occur due to the larger mass of the decaying charmonium resonance (not shown in the picture). For bottomonium a similar case arises and has been measured for B meson production above n=4, which results in much shorter lifetimes of these quasi-bound states. [5]

2.2 Quarkonium Production at Hadron Colliders

The J/Ψ(1S) and Υ(1S) mesons in hadron hadron collisions are produced via direct and indirect prompt production. Some generic Feynman diagrams for J/Ψ(1S) direct prompt production can be found in Fig. 2.4. The Υ(1S) Feynman diagrams for direct prompt production are similar. The indirect prompt production occurs via the decay of heavier states of the charmonium or bottomonium respectively (see Fig. 2.2 and 2.3). The J/Ψ(1S) meson is additional produced via nonprompt production from b meson decays (see Fig. 2.5).

The production mechanism of quarkonia itself is still under study and can not yet explain the data. A lot of progress has been made with a factorization approach using non-relativistic quantumchromodynamics (NRQCD), an effective field theory that includes the color-octet mechanism. If the mass of the quarks is large enough, the velocities of the quarks and antiquarks are non-relativistic ($v << c$). Quark potential models calculated an average value of $\beta = 0.3$ for charmonium and $\beta = 0.1$ for bottomonium, which means that the hypothe-

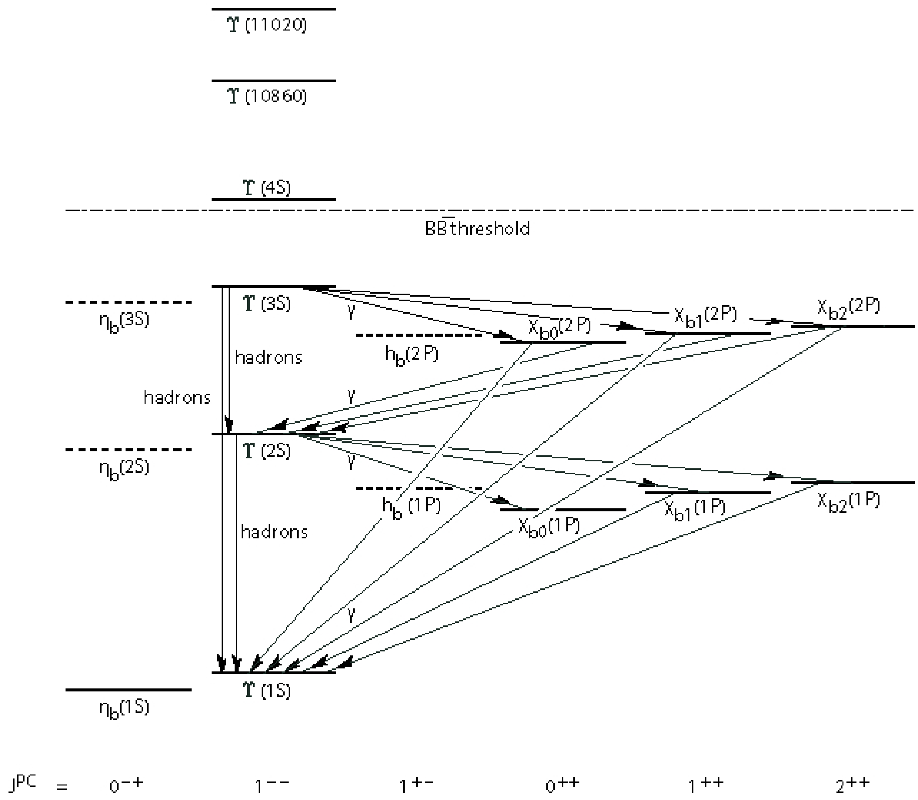

Figure 2.3: *Spectrum of energy levels of bottomonium [9].*

sis is reasonable for charmonium and in agreement for bottomonium [12–14]. Within the NRQCD the ansatz to calculate the quarkonium production is the following: the QCD is modified in the way that the relativistic and non-relativistic terms and the quark and antiquark components are separated automatically and the quark and antiquark are treated non-relativistically:

$$\mathscr{L}_{NRQCD} = \psi^\dagger(iD_o + \frac{\overrightarrow{D}^2}{2M})\psi + \chi^\dagger(iD_o - \frac{\overrightarrow{D}^2}{2M})\chi + \mathscr{L}_{Light} + \delta\mathscr{L}, \tag{2.1}$$

where ψ and χ are the Pauli spinor fields which create the heavy quark and the antiquark respectively. $\mathscr{L}_{Light}$ describes the usual QCD term for gluons and light quarks. $\delta\mathscr{L}$ takes the relativistic corrections of the full QCD into account. D_o and $\overrightarrow{D}$ are the time and space components of the gauge-covariant derivative $D^\mu = \delta^\mu + igA^\mu$, where g is the QCD coupling constant and $A^\mu = (\Phi, \overrightarrow{A})$ the SU(3) gauge field.

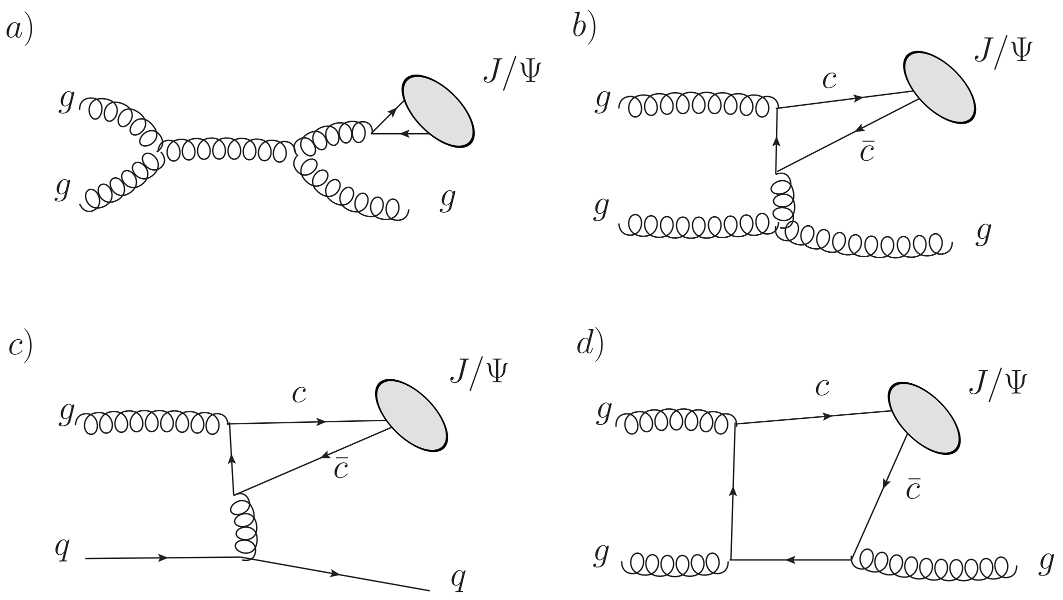

Figure 2.4: *Generic Feynman diagrams for prompt* J/Ψ(1S) *production in hadron-hadron collisions. The Feynman diagrams for* Υ(1S) *production are similar.*

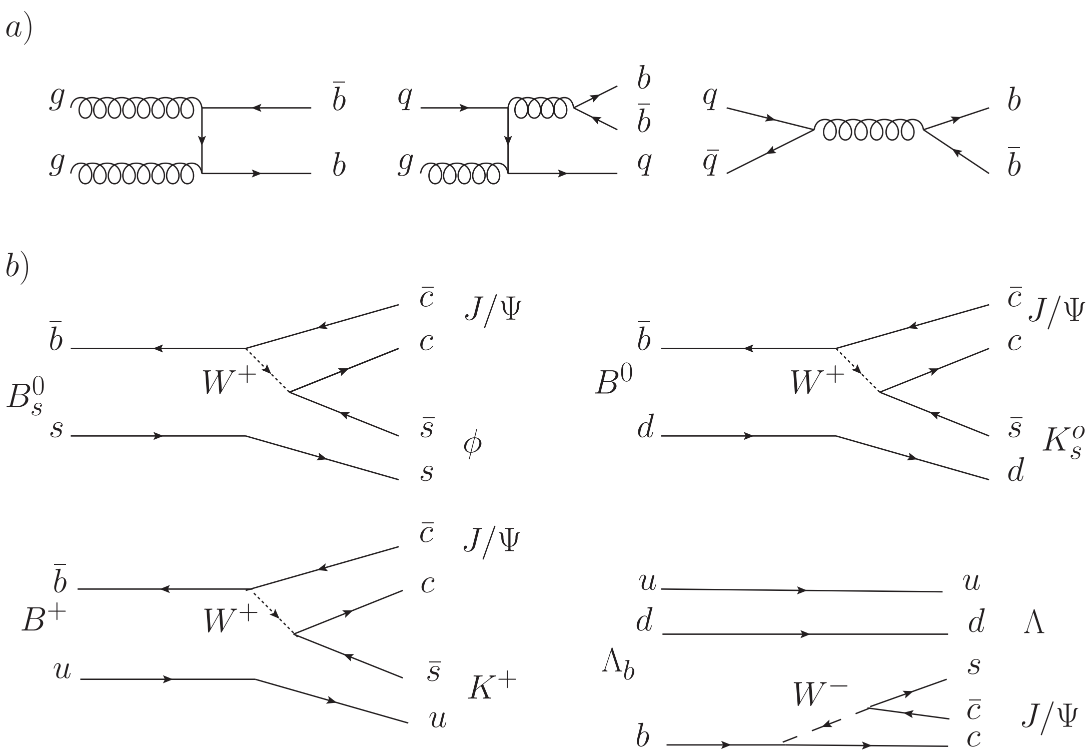

Figure 2.5: *Generic Feynman diagrams for a) b production in hadron-hadron collisions, b) nonprompt* J/Ψ(1S) *production via a b-meson decay.*

The NRQCD describes the results for J/Ψ(1S) and Υ(1S) (in high p_T regions) p_T-differential cross sections measured by the CDF experiment [6] in the dimuon channel, which was failed by former theoretical approaches.

The J/Ψ(1S) and the Υ(1S) differential cross section can be seen in Fig. 2.6, where the theoretical calculations are compared to the CDF data of RUN I ($\sqrt{s} = 1.8$ TeV). In NRQCD the long distance color octet matrix elements are freely adapted to data, therefore the results are correlated with data.

More details on different theoretical quarkonium production frameworks can be found in [12–14].

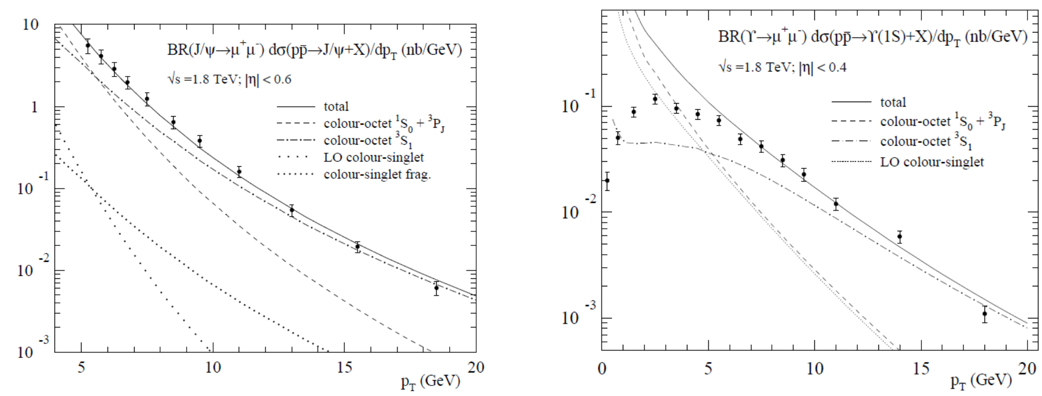

Figure 2.6: *Comparison of the CDF results [6] with the NRQCD approach using different color-singlet and color-octet contributions for the direct* J/Ψ(1S) *and inclusive* Υ(1S) *results [14].*

2.2.1 Polarization

The cross section depends on the polarization of the quarkonium, because this affects the muons kinematical properties. The polarization is defined as the alignment of the J/Ψ(1S) or Υ(1S) direction of motion and their Spin. Different theoretical approaches are resulting in different polarizations for the produced particles. In the NRQCD dominated by the color-octet component the directly produced J/Ψ(1S) spin is calculated to be fully transversely with respect to the Helicity frame (see Fig. 2.7). In the next to leading order (NLO) QCD dominated by the color-singlet production the same states possesses a large longitudinal component. For bottomonium, where the non-relativistic approach shows better agreement, there are additional contradictions between the data of the CDF [15] experiment and the D0 [16] experiment at Tevatron. The CDF data adverts to unpolarized and the D0 data to longitudinally polarized $\Upsilon(1S)$ mesons in the Helicity frame [8].

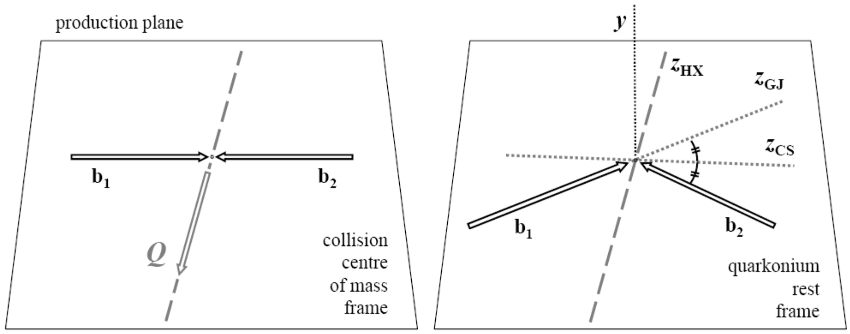

Figure 2.7: *Picture of the different reference frames used in polarization. The Helicity frame (HX): own flight/momentum direction of the quarkonium, the Collins-Soper frame (CS): bisecting angle between one beam and the opposite of the other beam and the Gottfried-Jackson frame (GJ): direction of the momentum of one of the two colliding beams [8].*

In this analysis the unpolarized scenario is used in the Monte Carlo simulations. This fact has to be kept in mind, as the unknown polarization of the charmonium and bottomonium will lead to the largest systematic uncertainty on the obtained results.

2.2.2 Definition of the Differential Cross section

The cross section calculates the probability for producing certain particles in the hadron collisions. The differential production cross section $\frac{d^2\sigma}{dp_T dy}$ for a collision process is the cross section at a certain rapidity and transverse momentum unit. The differential production cross section for $Q\bar{Q} = J/\Psi(1S)$ and $\Upsilon(1S)$ respectively is defined as:

$$\frac{d^2\sigma\left(pp \to Q\bar{Q}X\right)}{dp_T dy} \cdot \mathscr{BR}\left(Q\bar{Q} \to \mu^+\mu^-\right) = \frac{N^{\text{fit}}_{Q\bar{Q}}(p_T; \mathscr{A}, \epsilon_{\text{track}}, \epsilon_{\text{muon id}}, \epsilon_{\text{trig}})}{\int \mathscr{L} \cdot \Delta p_T \Delta y}, \tag{2.2}$$

where

$$N^{\text{fit}}_{Q\bar{Q}} = \frac{N^{\text{fit,uncorr}}_{Q\bar{Q}}}{\epsilon\mathscr{A}} = \frac{N^{\text{fit,uncorr}}_{Q\bar{Q}}}{(\epsilon_{\text{track}})^2 \cdot (\epsilon_{\text{id}})^2 \cdot \epsilon_{\text{trig}} \cdot \mathscr{A}} \tag{2.3}$$

is the corrected signal yield in a given p_T bin obtained from a weighted 1-dimensional fit to the invariant mass $M_{\mu^+\mu^-}$ distribution. $\mathscr{A}$ is the geometrical and kinematical acceptance for $J/\Psi(1S)$ and $\Upsilon(1S)$ obtained via Monte-Carlo simulations. ϵ_{track} is the tracking reconstruction efficiency, $\epsilon_{\text{muon id}}$ the muon identification efficiency and $\epsilon_{\text{trigger}}$ the trigger efficiency obtained via data driven methods. The corrected yield is normalized to the integrated luminosity $\int \mathscr{L}$, the transverse momentum Δp_T and rapidity Δy bin size of the $J/\Psi(1S)$ and $\Upsilon(1S)$ meson, respectively. The individual quantities used in the cross section calculation are described in more details in the related section.

CHAPTER 3

The Compact Muon Solenoid Experiment at the Large Hadron Collider

The **L**arge **H**adron **C**ollider (LHC) is a particle collider at the European Organization for Nuclear Research laboratory (CERN) in Geneva. The LHC is designed to accelerate protons and also heavy ions. With a circumference of 26.7 km and a designed nominal center of mass energy of 14 TeV for proton-proton collisions, the LHC is the world's largest and highest energy collider.

Protons, extracted from H_2 atoms, are accelerated in the **lin**ear **ac**celerator (LINAC) and then formed to bunches. Further they are accelerated to an energy of 26 GeV in the **P**roton **S**ynchrotron (PS). The energy is furthermore increased via the the **S**uper **P**roton **S**ynchrotron (SPS) to an energy of 450 GeV before being transferred to the LHC, where the protons shall be accelerated up to the designed energy of 7 TeV . The particles are kept on a circular orbit via 1232 superconducting dipole magnets, which are cooled with 96 t of fluid helium to a temperature of 1.9 K to generate the required magnetic field of 8.33 T. The dipole magnets increase the proton energy by 0.5 MeV per turn. Additionally 392 superconducting quadrupol magnets are used to focus the particles. At design luminosity of $\mathscr{L} = 10^{34}\ \mathrm{cm}^{-2}\,\mathrm{s}^{-1}$ the particles will be bundled in 2808 bunches, separated via 25 ns, which contain $1.15 \cdot 10^{11}$ particles each. The proton beams are brought to collision at four collision points to be further investigated by the experiments ALICE, ATLAS, CMS and LHC-b. In Fig. 3.1 the accelerator complex at CERN is shown with its different preaccelerators and experiments. The four experiments at LHC, which investigate the proton and heavy ion collisions respectively, are the ALICE, ATLAS, CMS and LHC-b detectors. ATLAS (**A** **T**oroidal **L**HC **A**pparatu**S**) and CMS (**C**ompact **M**uon **S**olenoid), located at opposite places at the LHC (Point 1 and 5 respectively), explore a wide range of physics phenomena. ALICE (**A** **L**arge **I**on **C**ollider **E**xperiment) and LHCb (**LHC**-**b**eauty) on the contrary are meant for more specific purposes. ALICE, located at point 2, will investigate quark-gluon plasma and LHCb, located at point 8, focus on b-quarks and the CP-symmetry violation. At the design luminosity of $\mathscr{L} = 10^{34}\ \mathrm{cm}^{-2}\,\mathrm{s}^{-1}$ up to 20 collisions per bunch crossing are expected. Fast electronic read-out channels are needed to match the resulting particles to the associated collisions, which are produced with a frequency of 40 MHz.

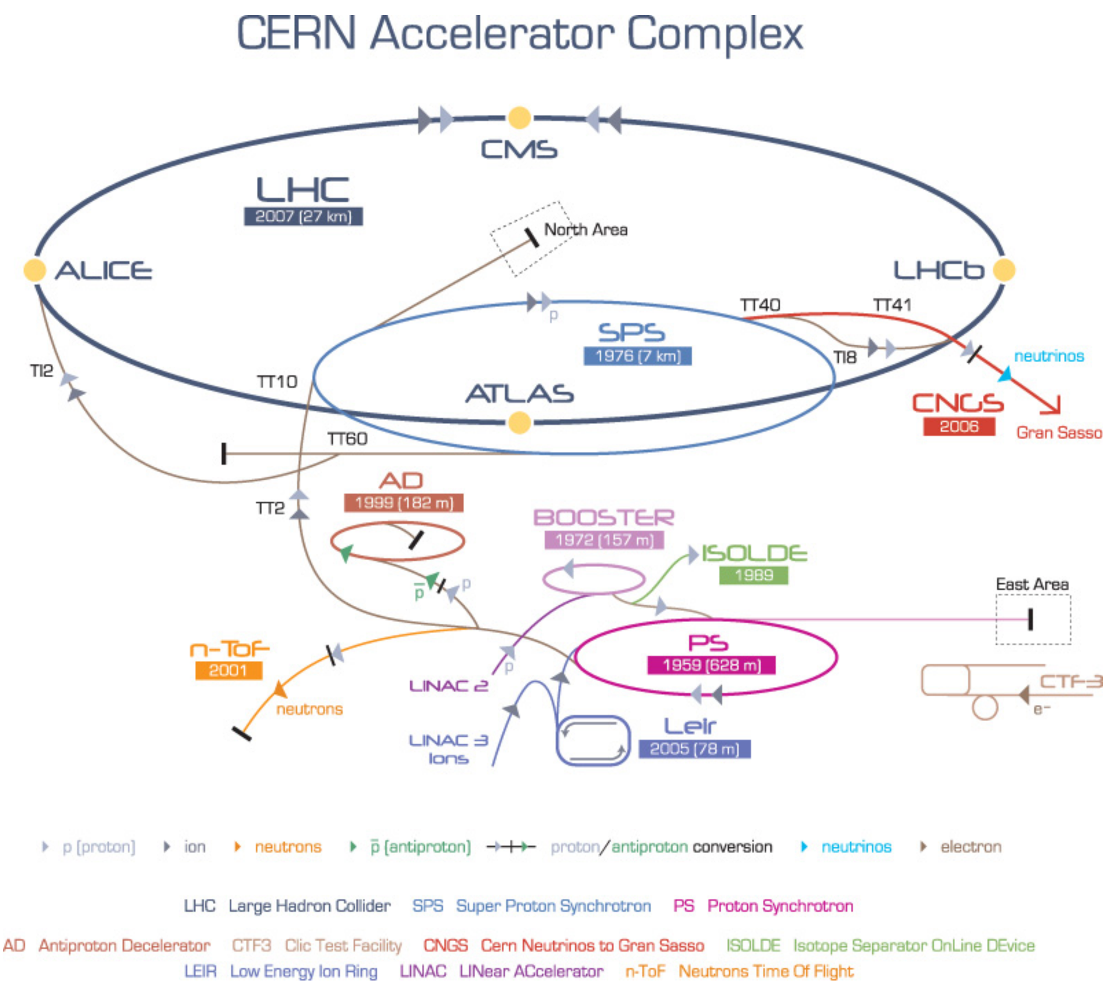

Figure 3.1: *Overview of the accelerator complex and the different experiments at CERN [17].*

On March 30th, 2010 the first proton-proton collisions with a center of mass energy of $\sqrt{s} = 7$ TeV took place. By the end of the year 2010 a maximum instantaneous luminosity of $2 \cdot 10^{32}$ cm^{-2} s^{-1} and a recorded integrated luminosity of 43.17 pb^{-1} was achieved for pp collisions (see Fig. 3.2).

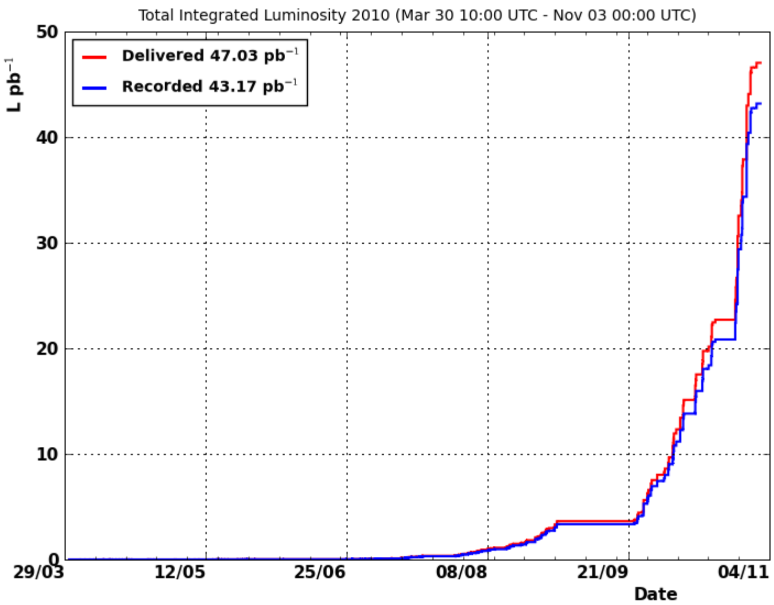

Figure 3.2: *Integrated luminosity versus time during stable beams at 7 TeV center-of-mass energy; delivered (red) and recorded by the CMS detector (blue) [18].*

3.1 Overview of the CMS Detector

The CMS experiment is 21.6 m long, has a diameter of 14.6 m and weights 12500 t. The detector has to meet several physical requirements in order to ensure a good identification and reconstruction of particles in a wide range of momenta and energy. These challenges are fullfilled due to the high magnetic field of up to 3.8 T and high performance subdetectors containing different kind of trackers and calorimeters assembled in the cylinder symmetrical structure of CMS. A schematic overview of the CMS detector can be found in Fig. 3.3.

CMS has a superconducting solenoid with a length of 12.9 m and an inner diameter of 5.9 m. Some of the properties of the solenoid can be found in Table 3.1. The large magnetic field of up to 3.8 T allows a strong track bending of charged particles for momentum measurements. The diameter of the magnet coil is large enough to accommodate the tracker and the calorimetry inside. In the center of the CMS detector close to the interaction point

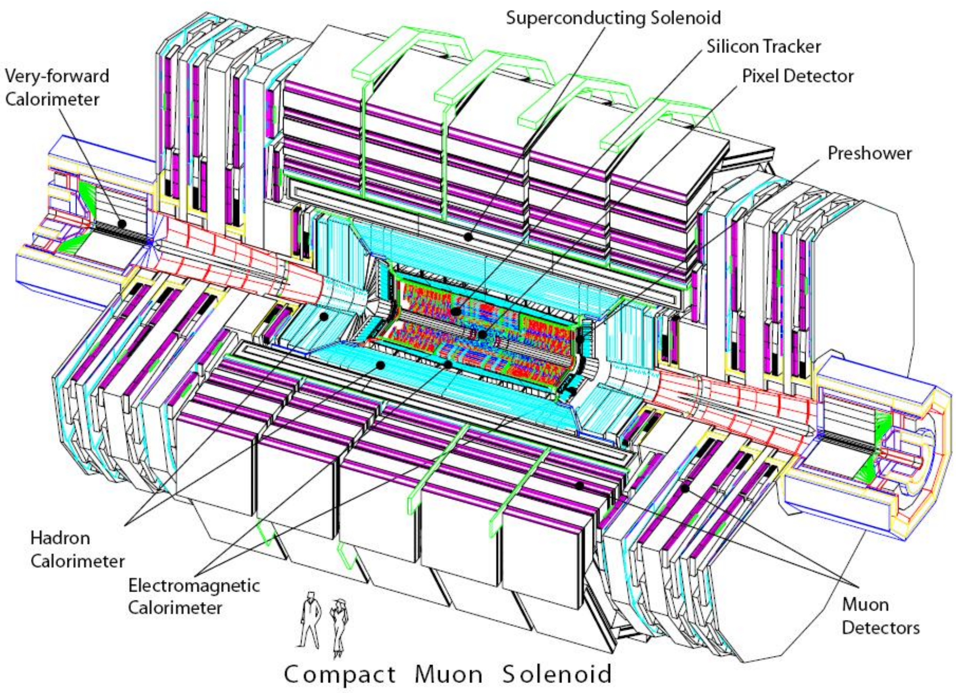

Figure 3.3: *Schematic overview of the CMS detector [19].*

the silicon pixel tracker detector is placed, enclosed from the silicon microstrip detector. Overall the cylindrical tracking volume has a length of 5.8 m and a diameter of 1.6 m. The tracker system of the CMS experiment is coated by the calorimeter. The electromagnetic calorimeter (ECAL) is made of lead tungstate ($PbWO_4$) crystals and surrounded by the brass and scintillator sampling hadron calorimeter (HCAL). Additionally to the ECAL, a preshower system is placed in front of the endcap to discriminate between high energetic photons and two closely-spaced lower energy photons coming from $\pi^0 \rightarrow \gamma\gamma$ decays. The central HCAL is completed by hadronic forward calorimeters in the endcaps. The return field core saturates 1.5 m of iron yoke, in which the muon chambers are located. The CMS detector focus on a good muon reconstruction, as muons with their clear signature are objects used in the new physics analyzes e.g. the Higgs boson with a mass bigger than 180 GeV can decay in four muons within the standard model. The muon chambers consist of three different kind of detectors: aluminum **d**rift **t**ubes (DT) in the barrel region, **c**athode **s**trip **c**hambers (CSC) in the endcaps and **r**esisitve **p**late **c**hambers (RPC) additionally [19].

This analysis is based on muon reconstruction, which is performed in the tracker and the muon chambers of the CMS detector. Therefore in the next sections, after a short summary of the coordinate conventions in CMS, the subdetectors needed for this analysis will be discussed.

Magnetic Field	3.8 T
Number of coil windings	2168
Current	19.5 kA
Stored energy	2.9 GJ

Table 3.1: *Properties of the superconducting solenoid [19].*

3.1.1 Coordinate system conventions

The coordinate system has its origin at the nominal interaction point inside the CMS detector and is defined in the following way: the x-axis points radially toward the center of the LHC, the y-axis is orientated vertically upward and the z-axis is defined along the beam axis. The azimuthal angle ϕ is measured from the x-axis in the $x-y$-plane and the polar space angle θ is zero at the positive and π at the negative z-axis. Because the polar angle θ is not Lorentz invariant, another coordinate is used, pseudorapidity η.

Rapidity and Pseudorapidity

The pseudorapidity η can be derived from the rapidity y of the particle. In collider physics, the rapidity y is more advantageous in comparison to the polarangle θ, because in the laboratory frame for a high energetic particle the decay products are closer to each other due to the Lorentz transformation than in the rest frame of the particle. The rapidity y is Lorentz space invariant and therefore independent of the choice of the reference frame.

$$y = \tanh^{-1}(\frac{v}{c}) = \frac{1}{2}\ln\left(\frac{E+p_{||}c}{E-p_{||}c}\right) = \frac{1}{2}\ln\left(\frac{E+p_{||}c}{\sqrt{p_T^2c^2+m^2c^4}}\right) = \frac{1}{2}\ln\left(\frac{\cos^2(\frac{\theta}{2})+\frac{m^2}{4p^2}+...}{\sin^2(\frac{\theta}{2})+\frac{m^2}{4p^2}+...}\right) \tag{3.1}$$

whereby E = $\sqrt{p_{||}^2c^2+p_T^2c^2+m^2c^4}$ is the energy, m the rest mass, θ the angle between the beam axis and the momentum, $p_{||}$ the longitudinal (or parallel) and p_T the perpendicular (or transverse) momentum of the produced secondary particle.
For rapidities close to the speed of light and negligible particle masses ($p >> mc$ and $\theta >> \frac{1}{\gamma}$) they can be approximated with the pseudorapidity η [20]:

$$y \approx -\ln\left[\tan\left(\frac{\theta}{2}\right)\right] \equiv \eta \tag{3.2}$$

In Fig. 3.4 the slice of one quarter of the CMS detector with the different values of the pseudorapidity is pictured. The CMS detector can be divided in three regions of pseudorapidity η. The barrel region is defined for an absolute value of $|\eta|$ smaller than 1.3, the endcap region is defined for an $|\eta|$ bigger than 1.6. and in between the transition region is placed.

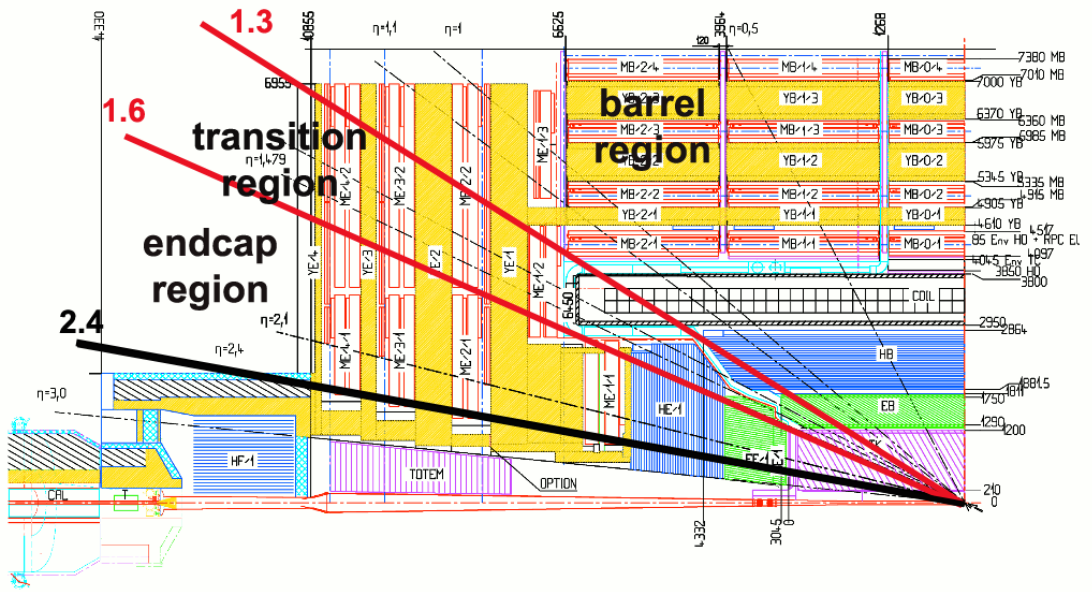

Figure 3.4: *Slice of one quarter of the CMS detector with rapidity definitions [19].*

3.2 Tracker System

The tracker system is placed around the interaction point at the innermost layer of the CMS detector, where the particle flux has around 10^7 particles per second (at a radius of $\approx$ 10 cm). This high track multiplicity requires high granularity detectors. Therefor three layers of silicon pixel detectors with 66 million pixel and 10 layers of silicon microstrip detectors with 9.6 million silicon strips are installed to measure the particle trajectories and decay vertices. The whole silicon tracker has a radius of 110 cm, a length of 540 cm and reaches a region of up to a pseudorapidity of 2.5. In Fig. 3.5 the modules distribution in a quarter of the CMS detector is presented.

Pixel Tracker Detector

The Pixel detector contains 3 barrel layers and 2 endcap layers at each side in a total surface of approximately 1 m^2. The barrel layers have a length of 53 cm and radii of 4.4 cm, 7.3 cm and 10.2 cm. The endcap disks are placed at 34.5 cm and 46.5 cm in each z direction and have radii between 6 and 15 cm. Each pixel has a volume of 100 x 150 μm^2, heading to an occupancy of 10^{-4} per pixel per bunch crossing and therefore 16000 readout chips are used. In the barrel a large Lorentz effect occurs due to a Lorentz angle of 23^o. This effect appears, if the magnetic field is not parallel to the electric field. The ionization charge is bend due to the Lorentz force and therefore spread over more pixels which leads to a better spatial resolution in the r-ϕ plane. In the endcap the pixel detector is rotated by 20^o to benefit from the same effect. The spatial resolution is expected to be 10 μm in the r-ϕ plane and 20 μm in

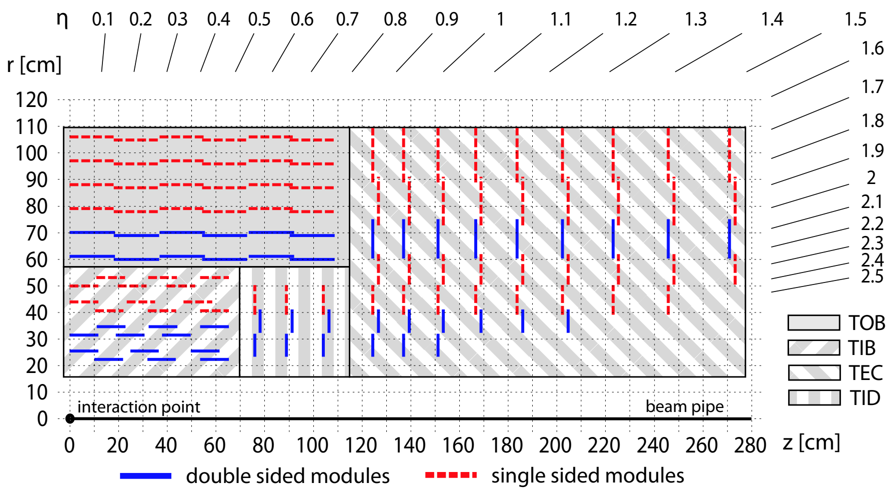

Figure 3.5: *The tracker layout of the CMS detector (one quarter of the z view) with the different subdetectors: double sided modules (blue) and single sided modules (red) of the strip detectors and the pixel detectors [21].*

the $r-z$ plane.

Silicon Strip Tracker Detector

In a radius around the interaction point of 20 to 55 cm the flux of the particles is low enough to facilitate the use of silicon strip detectors with a minimum cell size of 10 cm x 80 μm, leading to an occupancy of 2-3 % per bunch crossing. In a radius of 55 to 110 cm the approximate occupancy is around 1 % and therefore the silicon microstrips have a maximum cell size of 25 cm x 180 μm. The 9.3 million strip detectors are structured in around 15400 modules, which are planned to be cooled to 253 K and contain a total surface of 200 m^2. The silicon strip detector can be divided in four categories (see Fig. 3.5): the **t**racker **i**nner **b**arrel (TIB), the **t**racker **o**uter **b**arrel (TOB), the **t**racker **i**nner **d**isks (TID) and **t**he **t**racker **e**ndcap (TEC). The TIB contains of 4 layers in a distance smaller than 65 cm in both z directions parallel to the beamline. Each silicon sensor is 320 μm thick. The single point resolution in this detector part varies from 23-24 μm in the r-ϕ plane and is 230 μm in z direction. To fill the gap between TIB and TEC 3 small disks, the TID are used. The TOB on the other hand consists of 6 layers surrounding the TIB until a distance of 110 cm in z direction. Due to smaller radiation levels in this distance lower granularity silicon sensors (about 500 μm) can be used. The single point resolution in the TOB varies in the r-ϕ plane from 35 to 52 μm and is 530 μm in the z direction. The barrel SiStrip tracker is completed by the TEC at each end of the CMS detector. The TEC consists of 9 disks, which are placed perpendicular to the beam line between 120 and 280 cm in z direction. The blue color-coded modules in Fig. 3.5 are the double-sided stereo modules, which are twisted 100 mrad to each other to measure the missing component (z in TIB/TOB and r in TID/TEC) [19].

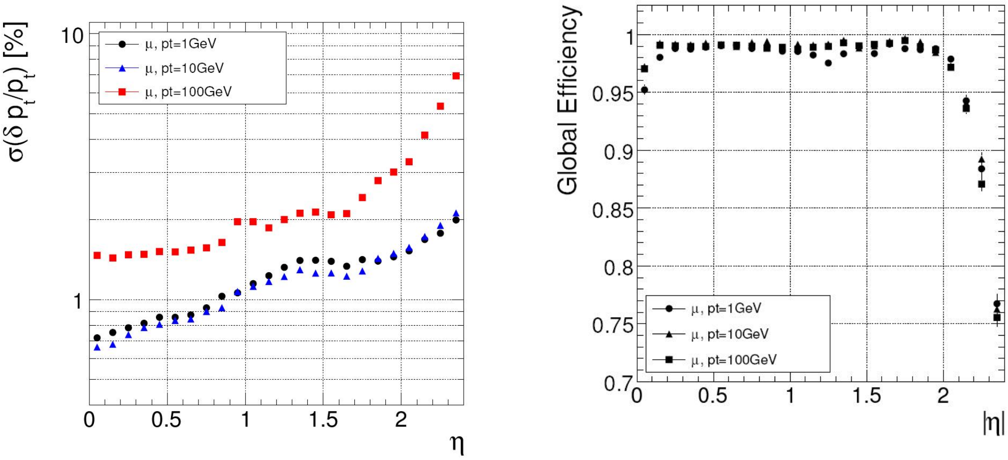

Figure 3.6: *The tracker resolution (left) and the global track reconstruction efficiency (right) for single muons with transverse momenta of 1, 10 and 100 GeV/c in dependence of η [19].*

The performance of the whole inner tracker system is presented in Fig. 3.6 [19] in dependence of η and for different energetic muons.

3.3 Muon Chambers

In the CMS detector three different types of gaseous detectors are used for muon identification and momentum measurement, which are all located in the return yoke. In Fig. 3.7 the layout of the muon system in the CMS detector is pictured. In the barrel region, where neutrons are the main source of background, the muon rate and the residual magnetic field are small, layers of aluminum **d**rift **t**ubes (DT), green-coded in the overview, are used of up to $\eta = 1.2$. The forward region is dominated by a high energetic neutrons induced backround, a high muon rate and high magnetic field. **C**athode **s**trip **c**hambers (CSC), pictured in blue in Fig. 3.7, are utilized in this region of up to a pseudorapidity of 2.4. Additionally to the DTs and CSCs **r**esistive **p**late **c**hambers (RPCs) are installed (colored in red in Fig. 3.7). The position resolution is coarser than the resolution in the RPCs and CSCs, but with a faster time response. The muon chambers have a total surface of 25000 m^2 with about 1 million electronic channels.

Drift Tube Chambers

The muon barrel detector consists of 250 drift tube chambers, located in 4 layers inside the return yoke, labeled as MB1-4, at a distance of 4.0, 4.9, 5.9 and 7.0 m around the beam axis.

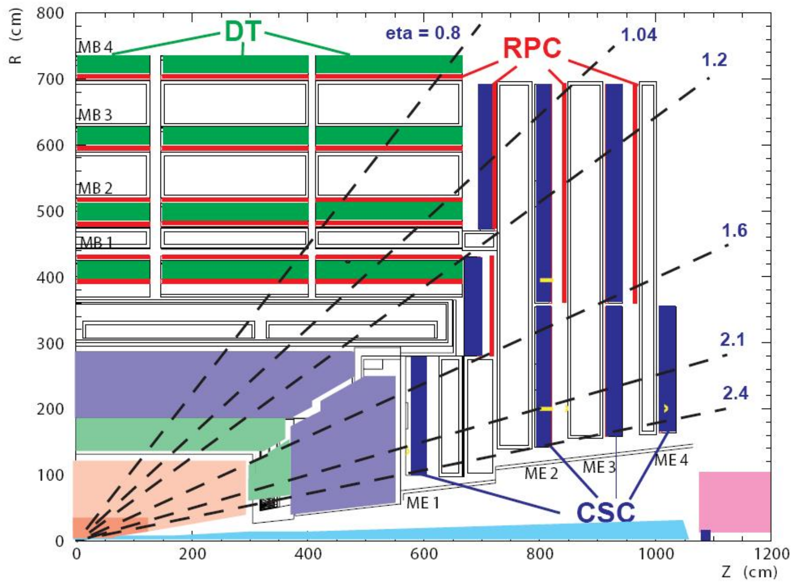

Figure 3.7: *Layout of the CMS muon system (one quarter of z view) [19].*

Each layer is divided into 5 wheels, labeled as YB-2 to YB+2 (in z), and subdivided into 12 sectors each covering an azimuthal angle of 30^o. The chambers in the different stations are arranged, that a high energetic muon, which is produced at the boundaries of the sectors, crosses at least 3 of 4 stations. The 2 layers MB1 and MB2 are encased by 2 RPCs and the outermost layers MB3 and MB4 are combined with one RPC each. In the drift tube chambers the single point resolution is around 200 μm with a maximum drift length of 2 cm. For each reconstructed muon the position resolution in ϕ is designed to be better than 1 mrad and the resolution in direction to be around 100 μm. If a high energetic muon crosses all 4 DTs and all 6 RPCs, it can produce up to 44 measurements for the muon reconstruction.

Cathode Strip Chambers

The muon endcap detector is made of 486 CSCs in the 2 endcaps, distributed in 4 stations perpendicular to the beam axis (labeled as ME1 to ME4). Up to a pseudorapidity of 1.6 additionally to the CSCs, RPCs are installed. Each CSC is built in trapezoidal shape to accommodate 6 gas gaps with planes of radial cathode strips and planes of anode wires almost perpendicular to the strips ensuing a good muon acceptance. A charged particle traversing through the chamber produces a charge in the anode wire and an image charge in a group of cathode strips due to the gas ionization and the consequently following electron avalanche. The center of gravity at this charge distribution in the cathode strips is taken for precise position measurement. In each CSC up to 6 space coordinates (r, ϕ, z) are computed in all 6 layers. The spatial resolution is about 100 μm and the angular resolution in ϕ about 10 mrad.

Resistive Plate Chambers

In the barrel region 480 RPCs are mounted. Each endcap is built out of 36 RPCs. The RPCs consists of double gap bakelite chambers with gas gaps of 2 mm. The RPCs operate in avalanche mode, where the electric field is reduced across the gap and therefore also the gas amplification, which results in a robust signal intensification at the front-end electronics to guarantee good operation at rates of up to 10 kHz/cm^2 in order to ensure good distinction between different bunch crossings. The good time resolution of the RPCs makes them good for the triggers used at level 1 and in the high level triggers [22].

In Fig. 3.8 the muon resolution in the barrel and endcap region is pictured. The blue color-coded line is the momentum resolution measured only in the muon system. This means that the resolution is obtained by the bending angle in the muon chambers, whereby the interaction point is taken as the origin of the muon. The green coded line belongs to the muon resolution, which is determined by the tracker system only. Due to the Silicon Strip and Pixel detectors the best momentum resolution for low p_T muons is achieved. For the full system (red line) the trajectory of the muon is extrapolated backwards to the interaction point. [19]

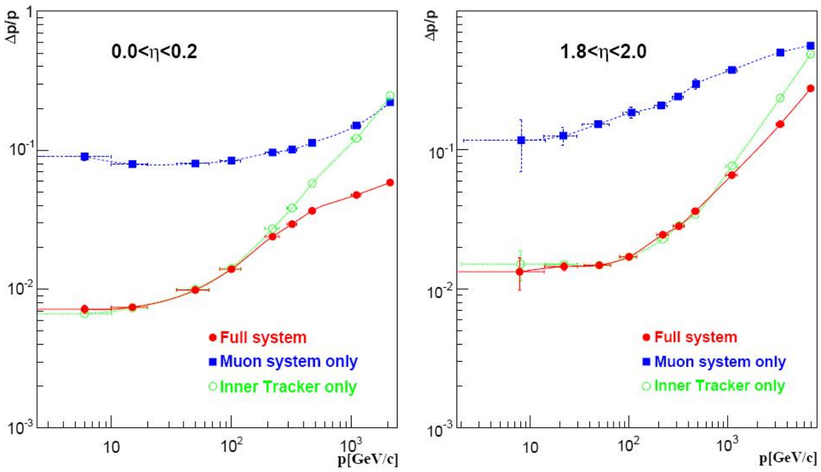

Figure 3.8: *The muon resolution in dependence of the momentum using the muon system only, the inner tracker only and both systems for two different η regions (barrel and endcap) [19].*

3.4 Trigger in CMS

At the design luminosity and nominal center of mass energy of 14 TeV around 10^9 interactions per second at a rate of 40 MHz are produced, but only 100 events/s can be read-out. These have to be reduced for further storaging via online selection processes (trigger). LHC is designed for 25 ns bunch crossing space , therefore to reduce the number of events where the interactions under study are coming together with those coming from other interactions from the same bunch crossing (pile up) the response time of the detector elements are obliged to have a good time resolution. The CMS trigger system relies therefore on four parts: the electronics, the LEVEL-1 trigger processors, the readout network and the online event filter system, the high level triggers (HLT). After 3.2 μs the detector data, which was held in buffers, is transferred to front end read out devices. During this time the decision whether to keep or discard an event from a certain bunch crossing must be made. The LEVEL-1 trigger needs less than 1 μs for the decision and its purpose is to identify certain objects such as muons, calculate their momentum and location and match them to a certain bunch crossing. The LEVEL-1 trigger relies on the calorimetry, the muon systems and correlation between the two systems. All muon detectors operate within the LEVEL-1 trigger system to supply independent and complete sources of information. After the LEVEL-1 trigger system the rate of around 100 kHz is again reduced via the HLT system to around 100 Hz for further data storaging with a size for each event of about 1.5 MB for proton-proton interactions. At HLT the information of the whole detector is used, based on the LEVEL-1 trigger objects and calculated with reconstruction algorithms similar to those used in the later accurate reconstruction for the data analysis [19].

3.5 Muon reconstruction

The raw data accumulated from the CMS experiment has to be further processed for physics analysis. The reconstruction process can be classified in three steps: local reconstruction within a certain detector module, global reconstruction within a whole detector and the combination of those to obtain physics objects. The **local** reconstruction within a muon drift tube chamber for example is received by muon hits in the drift cell, obtained from the the drift velocity, to built 3-D track segments from the layers. The cathode strip chambers on the other hand provides the position and time of arrival of the muon hits from the charge distribution induced in the strips. In each chamber 3-D track segments can be determined via 2-D segments in each layer combined with more layers. The local reconstruction of the RPCs provides only the position of the muon hit. Similar local reconstruction is done in the tracker and the calorimeters.

The **global** reconstruction is based on the local reconstruction in individual modules of a subdetector and combine them with algorithms to objects in this subdetector. In the muon system, if the information of all different muon chambers is used to reconstruct a physics object, this is defined as a **Standalone** muon. The track reconstruction takes into account the information of the magnetic field and the energy loss due to the material budget, which is primarily coming from the iron return yoke.

The **combined** reconstruction of physics objects relies on the whole CMS detector. If a muon object is reconstructed in the muon stations and then matched to a track reconstructed in the silicon tracker system, this is defined as a **Global** muon. The matching of silicon tracker tracks to standalone muon tracks is done by at first defining a region of interest for the matching due to the large track multiplicity in the tracker. Over the residual tracks in this region of interest, defined rectangular in $\eta - \phi$ space, is then iterated with more stringent momentum and spatial matching criteria to choose the best combination between silicon tracker track and standalone muon track. Global muons have therefore a minimum p_T cut of 4 GeV/c in the barrel and 1 GeV/c in the endcap region.

The **Tracker** muons are objects which are reconstructed in the tracking system and then matched to at least one tracklet in one muon station. The matching criteria between the silicon tracker tracks and the muon chamber segments is kept very loose, therefore further quality cuts have to be applied in the analysis itself (see Section 4.1). The algorithm for tracker muons uses a minimum p_T cut of 0.5 GeV/c and takes like all muon reconstruction algorithms the magnetic field and the multiple scattering into account. The maximum distance from a chamber edge for a extrapolated tracker muon, that misses the active detector volume, is 5 cm in x and y. Between the extrapolated track and the matching segment, the matching quality demands 3 cm in x direction [19, 23–25].

CHAPTER 4

Analysis

The data used in this analysis were taken during RUN B (Run number 146428 to 149294) of proton-proton collisions at $\sqrt{s} = 7$ TeV . RUN B collected an integrated luminosity of $36.38 \pm 1.46\ \text{pb}^{-1}$. It was preferred to a combination of RUN A + RUN B due to developments on synchronization between DT's and CSC's and algorithm improvements for the LEVEL-1 Triggers, which were implemented first in this runs [26].

The luminosity in CMS is measured using signals from the forward calorimeters (see Section 3.1) to obtain the instantaneous luminosity. Two online methods are used based on the forward calorimeters. One of them is the zero-counting method and takes the average fraction of empty towers to infer the mean number of interactions per bunch crossing. The second method uses the proportionality between average transverse energy per tower and luminosity. The final normalization of the luminosity measurements is made by LHC using the Van-der-Meer-scans. This scan determines the width of the colliding beams. A more detailed description can be found in [27]. The systematic uncertainty from luminosity measurements is 4 %, whereby the beam current measurement uncertainty dominates the total error [27].

For Monte Carlo (MC) simulations Pythia 6.421 was used. Pythia generates events based on the NRQCD with leading order color-singlet and color octet mechanisms (see Section 2.2). The matrix elements are tuned using Tevatron data. The non-prompt decays are generated using the Evtgen package. The final state Bremsstrahlung was simulated with PHOTOS package. The detector response is performed with GEANT4 [28]. In Table 4.1 the used simulated MC samples are listed. The total effective cross sections σ_{tot} for the different prompt and non-prompt decays include the dimuon branching fractions and filter efficiencies. The event filter requires two muons within the tracker acceptance $|\eta_{\mu}| < 2.5$ [29]. The used MC signal samples are added by scaling them to the same integrated luminosity $\mathscr{L}$ in data:

$$\text{scale} = \frac{\sigma_{tot} \cdot \mathscr{L}}{N_{\text{Events}}}, \tag{4.1}$$

where σ_{tot} is the total effective production cross section and N_{Events} is the number of generated events from Table 4.1.

Decay	MC sample	Events	σ_{tot} [nb]
prompt	JPsiToMuMu_2MuPEtaFilter_7TeV_pythia6_evtgen	8948960	543.42
$B^0 \to J/\Psi X$	B0ToJPsiToMuMu_2MuPEtaFilter_7TeV_pythia6_evtgen	2062640	32.07
$B^{\pm} \to J/\Psi X$	BpToJPsiToMuMu_2MuPEtaFilter_7TeV_pythia6_evtgen	2200122	35.46
$B_s^0 \to J/\Psi X$	BsJPsiToMuMu_2MuPEtaFilter_7TeV_pythia6_evtgen	517955	10.12
$\Lambda_b^0 \to J/\Psi X$	LambdaBToJPsiToMuMu_2MuPEtaFilter_7TeV_pythia6_evtgen	529547	2.08
prompt	Upsilon1SToMuMu_2MuPEtaFilter_7TeV_pythia6_evtgen	2308191	14.29

Table 4.1: *Used Monte Carlo samples, where the total effective cross section σ_{tot} includes the dimuon branching fractions and filter efficiencies [29].*

4.1 Event Selection

The events for this analysis are selected using the *HLTDoubleMu0* or the former replacing *HLTDoubleMu0_Quarkonium* HLT trigger path. This double muon HLT require two muons with opposite charge sign. The *HLTDoubleMu0_Quarkonium*, which is defined since run 147196, demands in addition that the invariant mass of the two muons is between $1.5 < M_{inv} < 14.5$ GeV/c^2. After offline cuts and background substractions the amount of reconstructed $J/\Psi(1S)$ events in double muon HLT skimmed datasets is halved with respect to the “single” muon HLT skimmed datasets [30]. Nevertheless due to the fact that they remain unprescaled[1] during these runs they are preferred to the “single” muon triggers. The prescale on a trigger can even change within a certain run, therefore a prescale on the trigger would complicate the cross section estimation.

The muons in the event, which survive the double muon trigger, have to be **Global** and **Tracker** muons simultaneously to ensure good muon reconstruction. The tracker muons are reconstructed from the collision point in the center of CMS outwards to the muon chamber and the global muon reconstruction starts from the muon chamber, then going inwards to the center of CMS. In Fig. 4.1 the muon distributions in dependence of η and p_T for muons

[1] Prescale "x" on trigger: every "x" event which fires the trigger is saved.

coming from the $J/\Psi(1S)$ and the $\Upsilon(1S)$ mesons are shown, where no further cuts are applied. It is obvious, that the muons need certain momenta to reach the different muon detectors in the barrel and endcap region (see Section 3.5). The $\Upsilon(1S)$ mesons coming from prompt decays are predominantly produced in the barrel region. The b production is enhanced in the forward-backward region. Muons from $J/\Psi(1S)$ resonances are therefore produced mostly in the forward-backward region due to the nonprompt fraction coming from b decays.

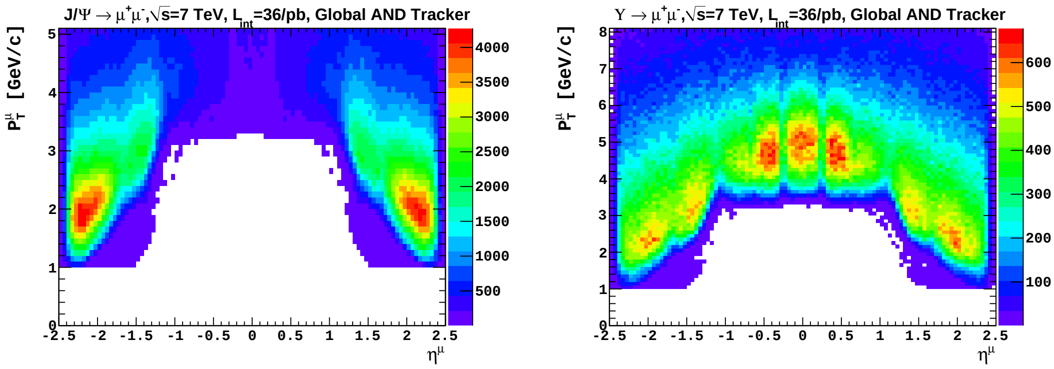

Figure 4.1: *The* $J/\Psi(1S)$ *(left) and* $\Upsilon(1S)$ *(right) muon distribution in dependence of* η *and* p_T *for Tracker and Global muons (simultaneously) in 36* pb^{-1} *of data. No further cuts are applied.*

Arbitration

If tracks are close to each other in the silicon tracker, it is possible, that the same segment or set of segments in the muon chamber is matched to more than one track reconstructed in the silicon tracker. A default arbitration algorithm is used to avoid this and improve the muon quality:

$$\Delta r^2 = \Delta x^2 + \Delta y^2 \tag{4.2}$$

where x and y are the distances between the extrapolated track and the segment in local x and y coordinates. The combination with the smallest Δr is selected [25, 31].

Momentum Scale Corrections

The measurement of the track momentum has systematic uncertainties due to limited knowledge and modeling of the detector material, the magnetic field, the alignment and the reconstruction algorithms. This has been studied by a working group within the CMS Collaboration using the well known mass of the $J/\Psi(1S)$ resonance. The method is still developing and is based on a likelihood fit to a model of the $J/\Psi(1S)$ mass lineshape [32]. This p_T correction, which is applied in both the $J/\Psi(1S)$ and $\Upsilon(1S)$ cross section results, depends on p_T, η and φ. The φ-dependence is different for negative and positive charged muons. [33]. The calibration function is described in Appendix A. The invariant mass of the two muons with and without the momentum scale correction in dependence of η, p_T and φ of the J/Ψ(1S) is compared to the world average value in Fig. 4.2. The mass values of the J/Ψ(1S) resonance in dependence of the different parameters are obtained fitting a Gauß function. The calibration function still has to be improved in forward and low p_T regions. A good agreement can be seen in the barrel region and for the higher momentum of the J/Ψ(1S) meson ($P_T^{J/\Psi(1S)}$>10 GeV/c). The mass values in φ-dependence are improved with the calibration function, but are systematically too low. The same plots in dependence of η, p_T, φ^{μ^-} and φ^{μ^+} of the muons can be found in Appendix A.

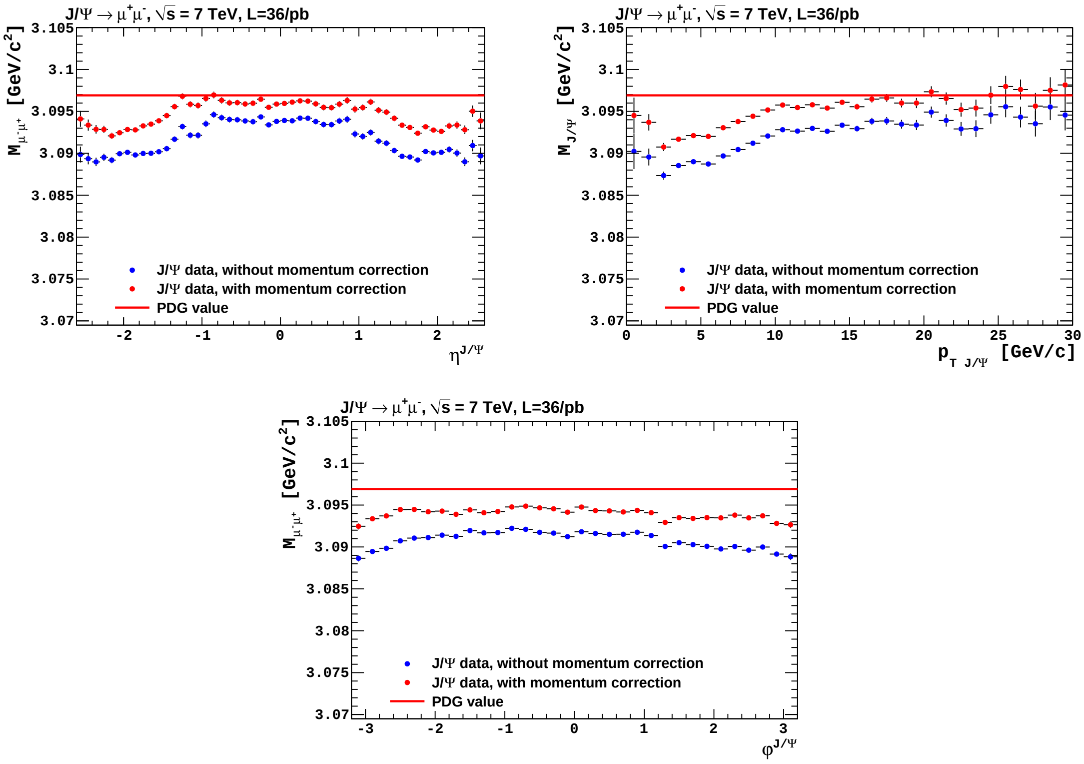

Figure 4.2: *Momentum scale corrections using the* J/Ψ(1S) *resonance in dependence of* η, p_T *and* φ *of the* J/Ψ(1S) . *The red line refers to the world average value [9] of the* J/Ψ(1S) *mass. The blue dots are the uncorrected and the red ones are the corrected data values. The uncertainties refer to the statistical uncertainty.*

4.1.1 Reconstruction of the $J/\Psi(1S)$ Meson

The quality of the reconstructed muon track can be improved applying reconstruction related selection cuts. The selection requires at least 12 hits in the tracker detector, whereby 2 hits have to be in the pixel detector. A normalized χ^2/ndf smaller than 4 for Tracker muons and smaller than 20 for Global muons are demanded additionally to reject both decay in flight and punch-through. The muons are required to have their origin in a cylinder of 3 cm-radius and 30 cm-length around the primary vertex and parallel to the beam pipe in order to remove cosmic muons. The radius (dxy) is quite loose in comparison to the suggestions in [31] to make sure, that muons from non-prompt $J/\Psi(1S)$'s coming from b decays remain in the event. A summary of the track quality cuts can be found in Table 4.2.

Number of valid hits	> 11
Number of pixel hits	> 1
Tracker χ^2/ndf	< 4
Global χ^2/ndf	< 20
$\lvert dxy \rvert$	< 3 cm
$\lvert dz \rvert$	< 15 cm

Table 4.2: *Used track quality cuts for the* $J/\Psi(1S)$ *analysis.*

Kinematical acceptance cuts are applied to ensure a high reconstruction efficiency in the phase-space of the analysis. The kinematical acceptance cuts were determined within the B-Physics Analysis Group of the CMS Collaboration and they are used for all analyzes in the Collaboration using $J/\Psi(1S)$'s [34]. The kinematical acceptance cuts are:

$$
\begin{aligned}
|\eta^\mu| < 1.3 \quad & p_T^\mu > 3.3 \text{ GeV/c} \\
1.3 < |\eta^\mu| < 2.2 \quad & p^\mu > 2.9 \text{ GeV/c} \\
2.2 < |\eta^\mu| < 2.4 \quad & p_T^\mu > 0.8 \text{ GeV/c}
\end{aligned}
$$

In the left plot of Fig. 4.3 opposite charge muons which are originating in a mass window of 1 GeV/c^2 around the $J/\Psi(1S)$ mass in an unpolarized MC, used for the acceptance estimation, are shown. There are no additional cuts applied for the muons, so all type of muons are shown. In the right plot in Fig. 4.3 the same distribution with the kinematical acceptance cuts mentioned above is shown.

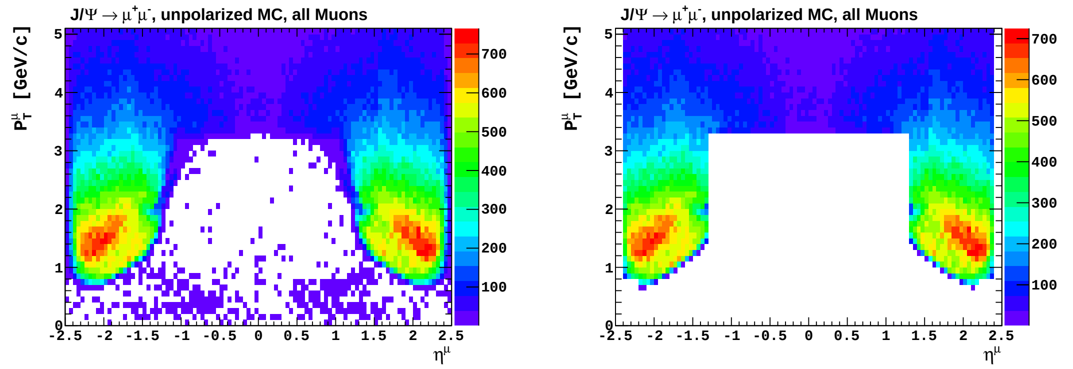

Figure 4.3: *Muon distribution in dependence of η and p_T in the* J/Ψ(1S) *mass window for the unpolarized MC for all kind of muons without any further cuts (left) and with the kinematical acceptance cuts (right).*

In the J/Ψ(1S) analysis only mesons within a rapidity range of $|y_{J/\Psi}| < 2.4$ are analyzed. A data/MC comparison is presented for the J/Ψ(1S) candidates and their muons. For each φ, η and p_T bin the invariant mass of the J/Ψ(1S) candidates in data is fitted using a Gauß fit for the signal and a linear fit for the background contribution (see Eq. 4.4). Two generic dimuon mass distribution with the fit function can be found in Fig. 4.4. The various MC contributions are added by scaling them to the same integrated luminosity. Afterwards the whole MC simulation distribution is normalized to the number of J/Ψ(1S) candidates in data. The data/MC comparisons can be seen in Fig. 4.5. In general the MC simulation describe the shape in data, except for high η and low p_T regions in the J/Ψ(1S) distributions. In both cases the data is underestimated by the MC.

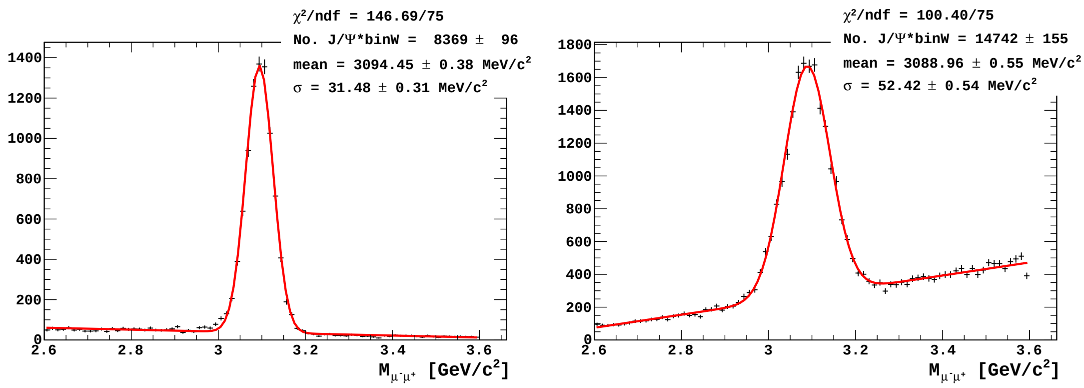

Figure 4.4: *Generic dimuon invariant mass plots, where the fit function is a Gauß function for the signal and a polynom of 1st order for the background:* $0.4 < \eta_\mu < 0.5$ *(left) and* $1.0 < p_{T\ J\Psi} < 2.0$ *GeV/c (right) obtained with 36* pb^{-1} *of CMS data. Momentum scale correction is not applied.*

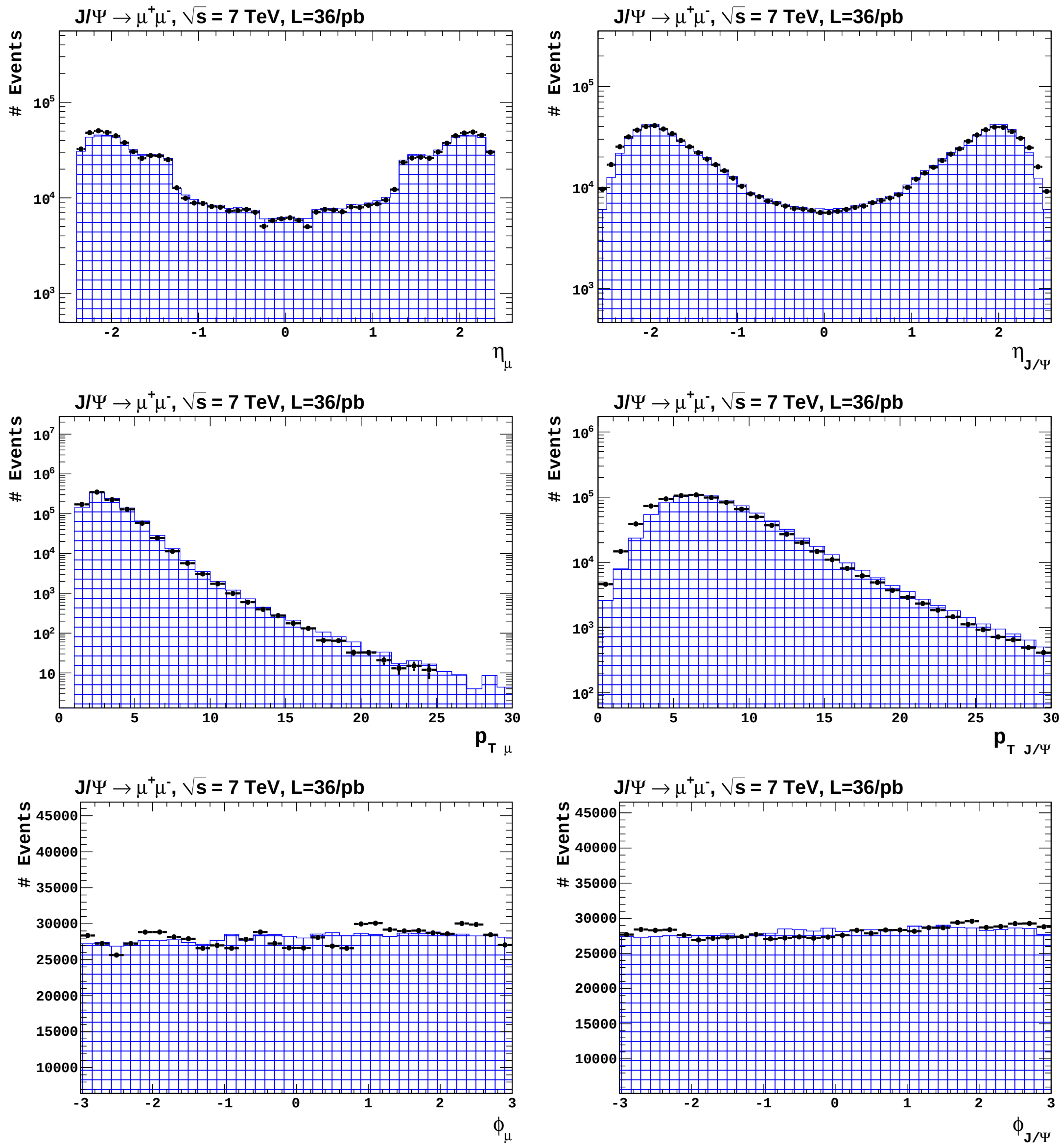

Figure 4.5: *Side-band subtracted distributions of muons from J/Ψ candidates (first column) and* J/Ψ(1S) *candidates (second column) in dependence of* η, p_T *and* φ *data (black dots) compared to MC (blue histograms, see Table 4.1). The MC is normalized to the yield in data.*

Yield extraction

The number of J/Ψ(1S) events (yield) for the cross section estimation is obtained in three steps. First of all a function is fitted to the dimuon invariant mass distribution in a range from 2.6 GeV/c^2 to 3.6 GeV/c^2. The invariant mass distribution $M_{\mu_+\mu_-}$ includes all kinematical acceptance cuts, track quality cuts and the momentum scale correction used in this analysis. The function has a Gauß function to fit the signal and a linear function to fit the background:

$$\begin{aligned} f_{Signal+Bkg}(M_{\mu^+\mu^-}) &= f_{Signal}(M_{\mu^+\mu^-}) && + f_{Bkg}(M_{\mu^+\mu^-}) && (4.3) \\ &= \frac{N_{signal}}{\sqrt{2\pi}\cdot\sigma}\cdot\exp\left(-\frac{1}{2}\cdot\frac{(M_{\mu^+\mu^-}-\mu)^2}{\sigma^2}\right) && + a\cdot M_{\mu^+\mu^-} + b && (4.4) \end{aligned}$$

where N_{signal} is the number of J/Ψ(1S) mesons, σ and μ are the width and the mean value of the Gaußian distribution. This fit is only used to estimate the slope and the y-intercept freely for the background fit. Due to final state radiation and different mass resolutions in the different η regions of the CMS detector this *signal+background* fit function cannot describe the data completely.

In the second step of this approach the optimal background fit interval is determined. For this reason a line function in the range of 2.6 to 3.1 GeV/c^2 is fitted. If the normalized χ^2 of this fit is not smaller than 2 the function is fitted again in a 0.1 GeV/c^2 smaller fit range, subtracted from the upper fit range value. The same method is used to determine the upper point of the signal region, where a linear fit is applied in the range of 3.1 to 3.6 GeV/c^2. If the normalized χ^2 is not smaller than 2 the fit is performed again in a smaller range, which is obtained by adding 0.1 GeV/c^2 to the lower fit range value. After determining the background fit region a fit is performed in which the signal peak is excluded. The number of signal and background $N_{Signal+Bkg}$ events is obtained by counting the entries of the histogram in the obtained signal region, where the uncertainty $\sigma_{N_{Signal+Bkg}}$ is the square root of the number of entries. The number of background events N_{Bkg} is determined by integrating the line fit in the same signal region, while the signal region is not excluded anymore and the former obtained covariance error matrix of the background fit is used to evaluate the uncertainty of the number of backgrounds $\sigma_{N_{Bkg}}$. The acquired number of J/Ψ(1S) signal events N_{signal} is then obtained by subtracting the numbers and the corresponding uncertainty $\sigma_{N_{signal}}$ is propagated.

$$N_{signal} = |N_{Signal+Bkg} - N_{Bkg}| \tag{4.5}$$

$$\sigma_{N_{signal}} = \sqrt{\sigma^2_{N_{Signal+Bkg}} + \sigma^2_{N_{Bkg}}} \tag{4.6}$$

In the last step, the value of the mean and the width of the signal peak is extracted in order to obtain the mass and its resolution. Therefore only a Gauß fit function is applied in the central part of the peak in order to avoid a bias from the non-Gaußian tails, which originate from final state radiation. The Gauß fit is repeated in a 1 to 3 σ region around the mean of the Gauß function to optimize the fit results with respect to the former fit results. The different steps are shown for different p_T and η regions in Fig. 4.6 and 4.7, where the first step corresponds to the first column.

The obtained mass of the $\mathrm{J}/\Psi(1\mathrm{S})$ meson and the mass resolutions in the different pseudorapidity and transverse momentum ranges can be found in Table 4.3. The mass values in low p_T and high rapidity regions deviate from the world average value of 3096.916 ± 0.011 MeV/c^2 hence the p_T correction formula still needs improvements in this regions (see Section 4.1). As expected the mass value optimizes in comparison to the PDG value in high p_T regions and small η regions. The mass resolution improves due to the different used detectors from the forward region to the barrel region by more than 40 %.

	$p_T^{J/\Psi}$ [GeV/c]	mean [MeV/c^2]	sigma [MeV/c^2]
$\lvert\eta^{J/\Psi}\rvert < 1.3$	> 10	3095.85 ± 0.20	26.75 ± 0.35
	< 10	3096.93 ± 0.13	24.54 ± 0.20
$1.3 < \lvert\eta^{J/\Psi}\rvert < 1.6$	> 10	3094.39 ± 0.26	37.67 ± 0.44
	< 10	3096.03 ± 0.45	40.02 ± 0.80
$1.6 < \lvert\eta^{J/\Psi}\rvert < 2.4$	< 10	3092.99 ± 0.14	46.07 ± 0.22
	> 10	3094.41 ± 0.34	45.90 ± 0.54

Table 4.3: *Measured mean and sigma of the Gauß function in the different pseudorapidity and transverse momentum bins for the* $\mathrm{J}/\Psi(1\mathrm{S})$ *meson using 36* pb^{-1} *of CMS data.*

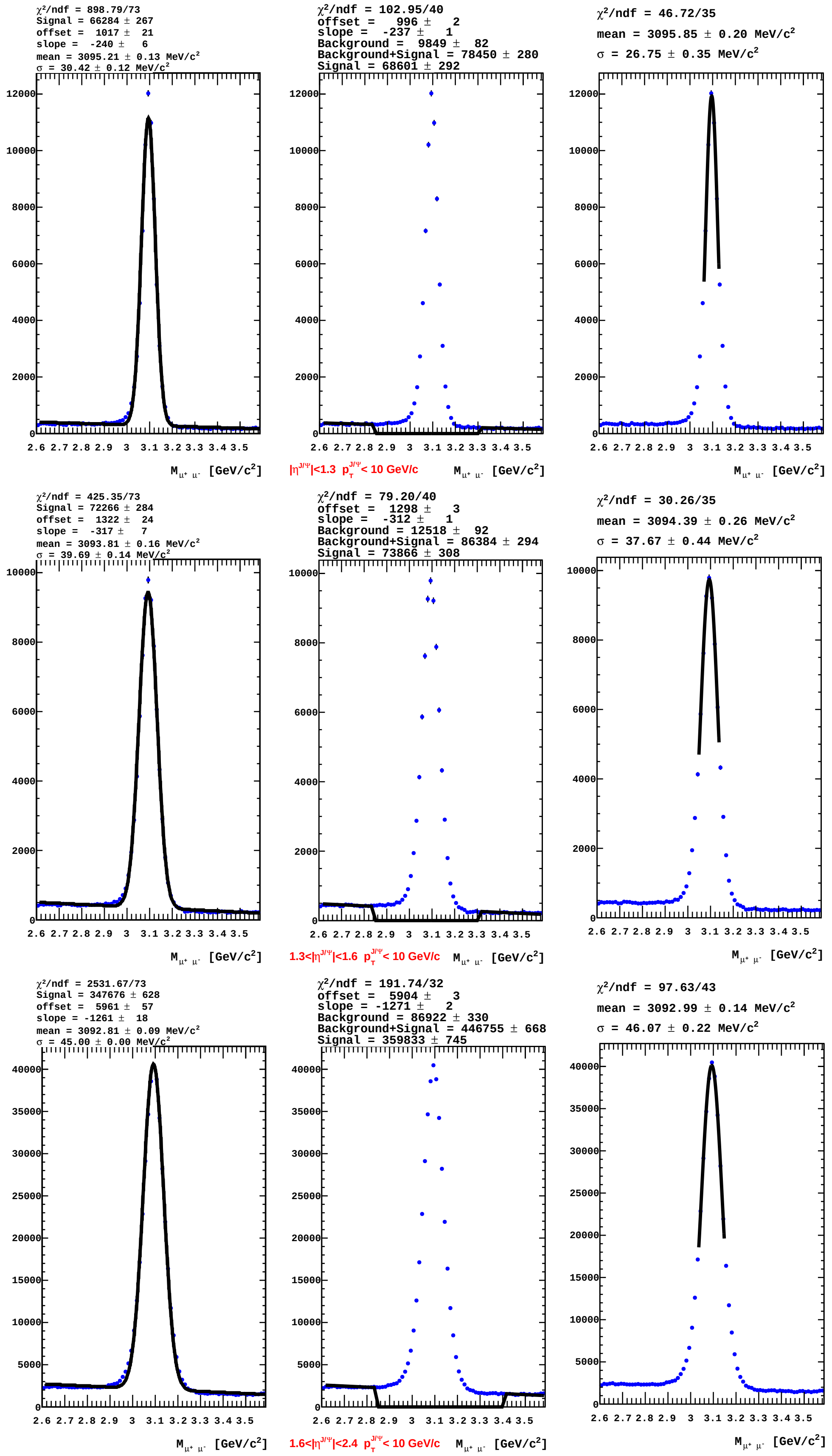

Figure 4.6: *Dimuon invariant mass distribution for* $p_T^{J/\Psi(1S)} < 10$ *GeV/c in the* η*-regions:* $|\eta^{J/\Psi(1S)}| < 1.3$, $1.3 < |\eta^{J/\Psi(1S)}| < 1.6$ *and* $1.6 < |\eta^{J/\Psi(1S)}| < 2.4$ *(rows) and the 3 steps (columns) used to determine the number of J/ψ events with 36* pb^{-1} *of CMS data.*

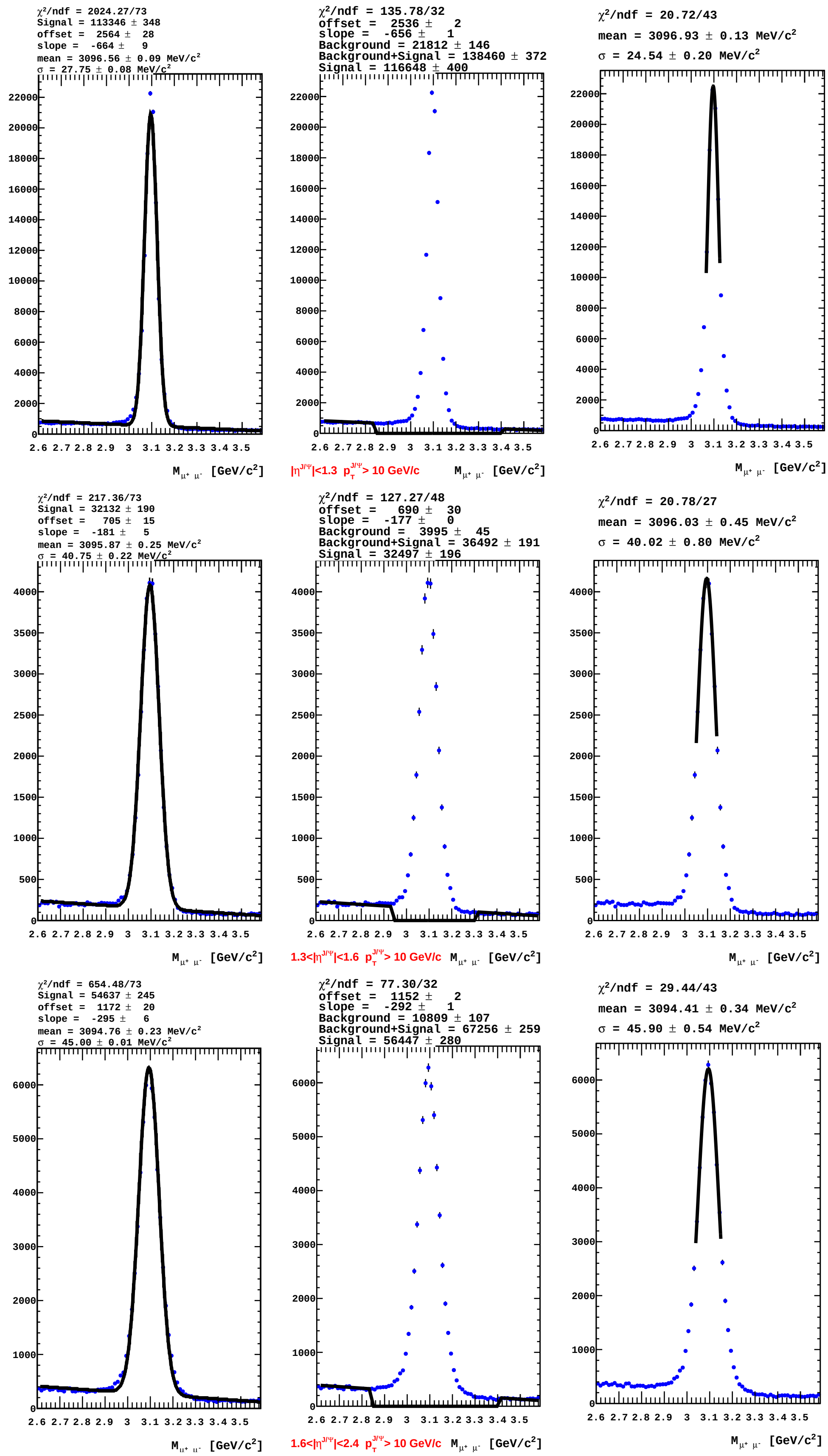

Figure 4.7: *Dimuon invariant mass distribution for $p_T^{J/\Psi(1S)} > 10$ GeV/c in the η-regions: $|\eta^{J/\Psi(1S)}| < 1.3$, $1.3 < |\eta^{J/\Psi(1S)}| < 1.6$ and $1.6 < |\eta^{J/\Psi(1S)}| < 2.4$ (rows) and the 3 steps (columns) used to determine the number of J/ψ events with 36 pb^{-1} of CMS data.*

4.1.2 Reconstruction of the $\Upsilon(1S)$ Meson

Similar track quality cuts are applied in the $\Upsilon(1S)$ analysis. In the tracker detector at least 12 hits are required, with at least one originating from the pixel detector. A vertex cut is demanded as well requiring the muons coming from an origin around the primary vertex in a cylinder of 0.2 cm radius and 50 cm length parallel to beam line. The radius is kept smaller than the one from the $J/\Psi(1S)$ analysis, hence $\Upsilon(1S)$ mesons are only coming from prompt decays. The track quality cuts are summarized in table 4.4. The analysis is performed in a rapidity window of $|y_\Upsilon| < 2.0$, hence the acceptance is decreasing at high rapidity (see Fig. 4.13 in Section 4.2).

Number of valid hits	> 11
Number of pixel hits	> 0
Tracker χ^2/ndf	< 5
Global χ^2/ndf	< 20
$\lvert dxy \rvert$	< 0.2 cm
$\lvert dz \rvert$	< 25 cm

Table 4.4: *Used track quality cuts for the* $\Upsilon(1S)$ *analysis.*

A good reconstruction in the analysis phase-space is ensured applying following kinematical acceptance cuts, obtained within the B Physics Analysis Group of the CMS Collaboration [34]:

$$\begin{aligned} |\eta^\mu| < 1.6 \quad & p_T^\mu > 3.5 \text{ GeV/c} \\ 1.6 < |\eta^\mu| < 2.4 \quad & p_T^\mu > 2.5 \text{ GeV/c} \end{aligned}$$

The η-p_T reconstruction efficiency of muons in a mass window of 3 GeV/c^2 around the $\Upsilon(1S)$ mass is shown in Fig. 4.8. The $\Upsilon(1S)$ decay mostly in the barrel region and the momentum cuts are compared to the $J/\Psi(1S)$ analysis higher to ensure good reconstruction of the muons.

A comparison of the η, p_T and φ distributions of $\Upsilon(1S)$ candidate kinematic parameters between data and MC is performed. The number of $\Upsilon(1S)$ candidates in data for each φ, η and p_T bin is obtained by using a Gauß fit for the signal and a linear fit for the background (see Eq. 4.4) to the dimuon invariant mass distribution. Some generic dimuon mass distributions with the fit function can be found in Fig. 4.9. The MC samples, which are used in this

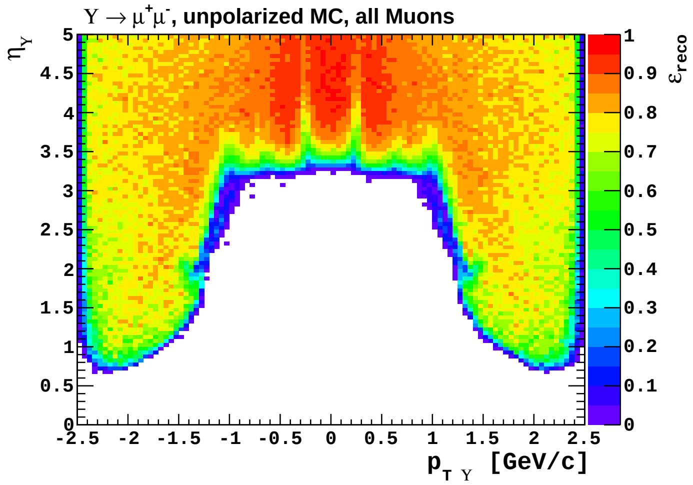

Figure 4.8: *Muon reconstruction efficiency in dependence of η and p_T in the $\Upsilon(1S)$ mass window for the unpolarized MC without any further cuts .*

analysis, are listed in Table 4.1. The comparison can be found in Fig. 4.10. The MC distributions are normalized to the data yield. The MC simulations describe the shape in data, except for high and low p_T regions. The p_T distribution is divided to avoid normalization effects coming from the discrepancies in low p_T regions, where the data is underestimated.

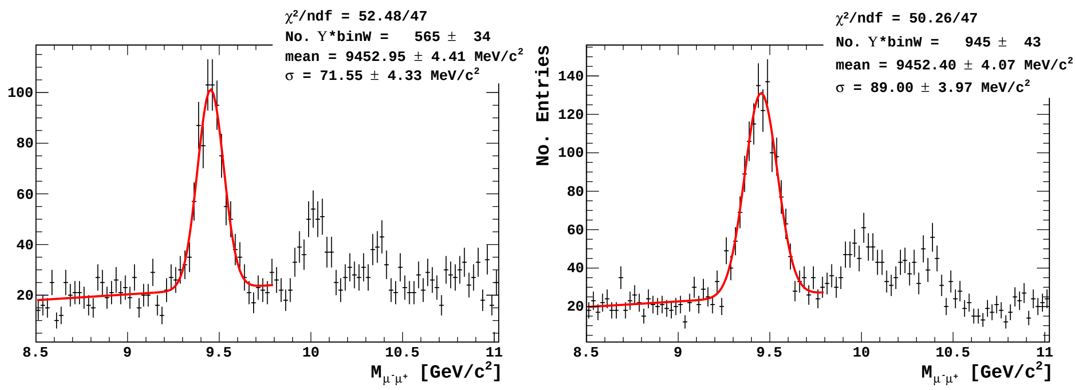

Figure 4.9: *Generic dimuon invariant mass plots, where the fit function is a Gauß function for the signal and a linear line for the background:* $-0.7 < \eta_\Upsilon < -0.6$ *(left) and* $13.0 < p_{T\,\Upsilon} <$ 14.0 *GeV/c (right) obtained with 36* pb^{-1} *of CMS data. Momentum scale correction is not applied.*

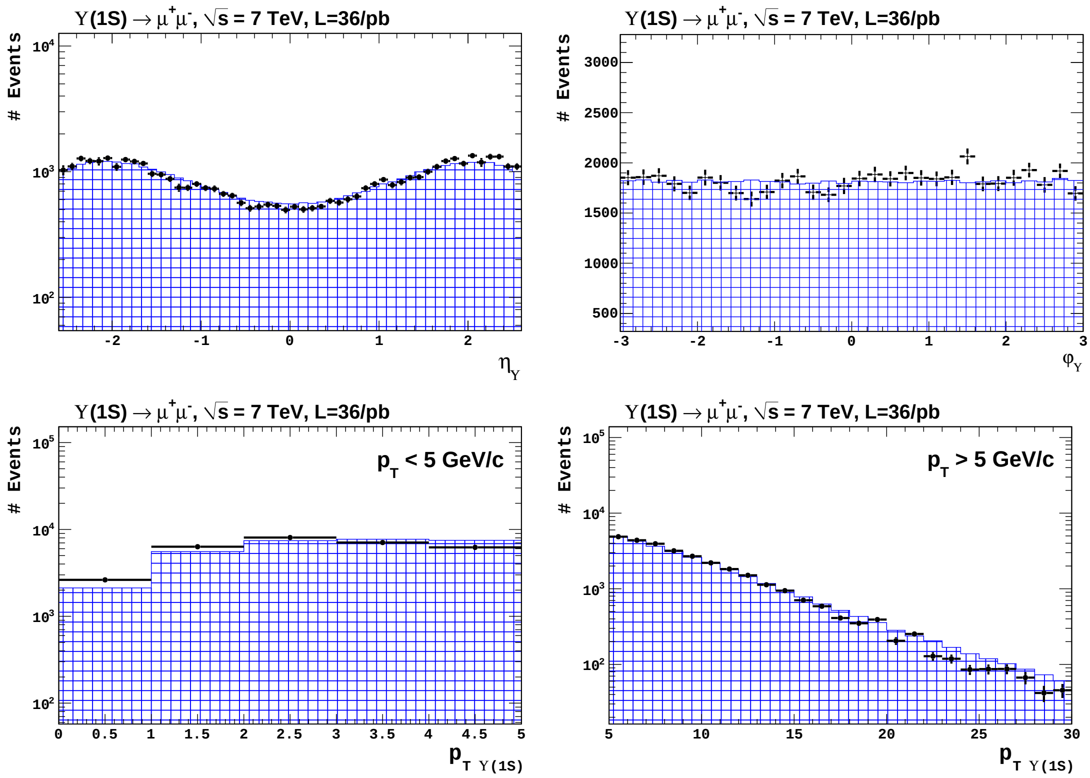

Figure 4.10: *Side-band subtracted distributions of* $\Upsilon(1S)$ *candidates in dependence of* η, p_T *and* φ. *Data (black dots) compared to MC (blue histograms, see Table 4.1). The MC is normalized to the yield in data.*

Yield extraction

The number of $\Upsilon(nS)$ events (yield) for the cross section estimation is obtained using a fit to the dimuon invariant mass distribution, where all kinematical acceptance cuts, track quality cuts and the momentum scale correction are applied. The function has four Gauß functions to fit the $\Upsilon(nS)$ resonances and an exponential or linear function to fit the background. Two Gauß functions are used to fit the $\Upsilon(1S)$ resonance. Due to the different momentum resolutions in the different η regions of the CMS detector a single Gauß function cannot describe completely the data. The mean is the same for both Gauß functions and the widths are free parameter. The second and the third Gauß function of the fit function are used to fit the $\Upsilon(2S)$ and $\Upsilon(3S)$ resonance, respectively. The means and widths are kept as free parameters. For this reason the uncertainties of the number of $\Upsilon(nS)$ events contain the statistic uncertainty and the systematic uncertainty due to the fit. The fit functions integrated over the whole p_T range in the central, transition and barrel region can be found in Fig. 4.11.

The obtained masses of the Υ(nS) mesons in the different pseudorapidity ranges can be found in Table 4.5. The mass values are determined by integrating over the whole p_T region. Therefore the obtained values deviate from the PDG values [9] due to the variations in large pseudorapidity and low momentum regions (see Fig. 4.2). It has to be taken into account that the uncertainties are the statistical only and no systematics are obtained.

	PDG	$\lvert\eta^{\Upsilon(1S)}\rvert < 1.3$	$1.3 < \lvert\eta^{\Upsilon(1S)}\rvert < 1.6$	$1.6 < \lvert\eta^{\Upsilon(1S)}\rvert < 2.4$
Υ(1S)	9460.30 ± 0.26	9457.37 ± 0.87	9456.06 ± 2.04	9455.42 ± 1.40
Υ(2S)	10023.26 ± 0.31	10019.87 ± 2.07	10011.84 ± 6.13	10014.84 ± 7.45
Υ(3S)	10355.2 ± 0.5	10350.73 ± 3.45	10355.23 ± 9.76	10337.49 ± 13.11

Table 4.5: *Measured mean in MeV/c^2 of the Υ(nS) resonances in the different pseudorapidity bins compared to the PDG values [9] using 36 pb^{-1} of CMS data.*

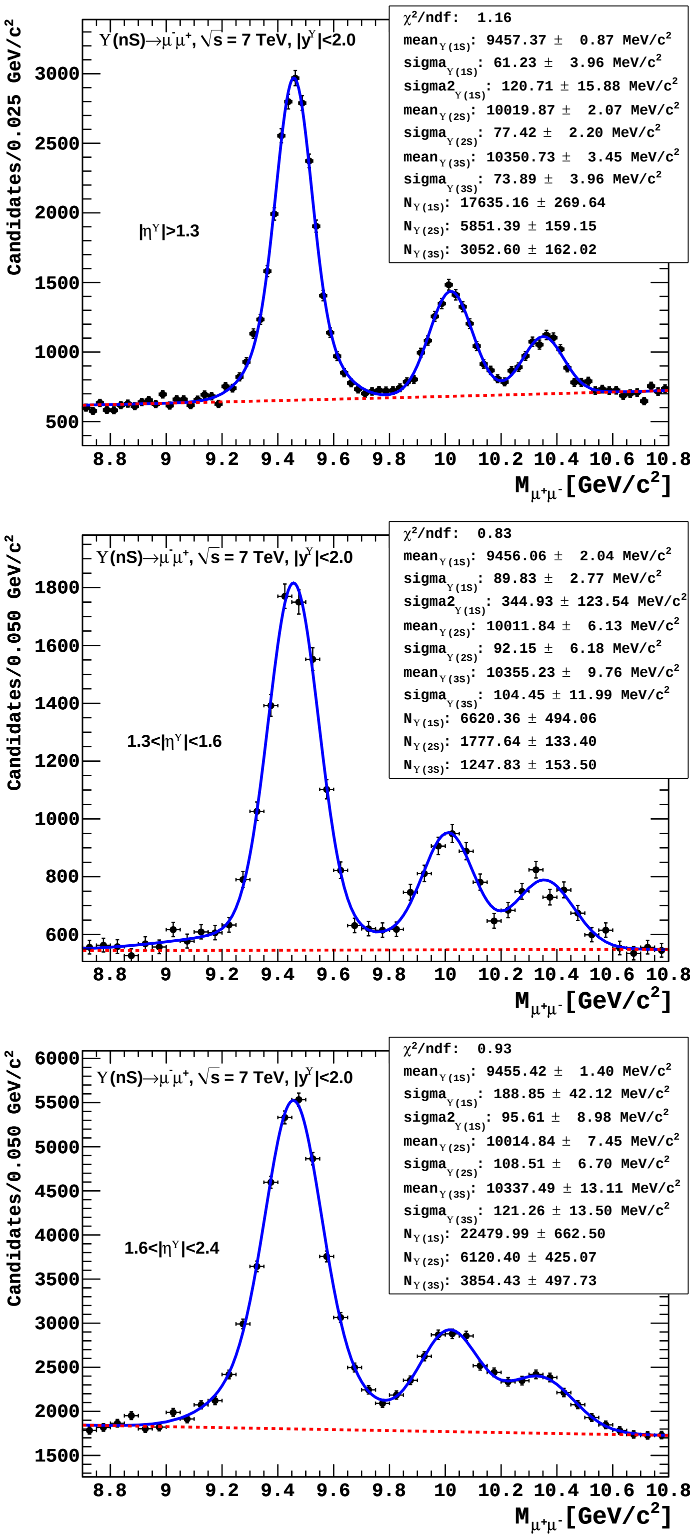

Figure 4.11: *Dimuon invariant mass distribution integrated over the whole p_T range in the 3 η regions used to determine the number of $\Upsilon(\mathrm{nS})$ events with 36 pb^{-1} of CMS data.*

4.2 Acceptance

The Muons need certain momenta to reach the different muon chambers (see Fig. 4.1 in Section 4.1.1). Additional the CMS detector limits the detection of muons in a pseudorapidity range of $|\eta| < 2.4$. The acceptance is the probability, that each muon leaves a detectable track limited via this geometrical and kinematical acceptance of the CMS detector. The acceptance contains also the kinematical acceptance cuts for $J/\Psi(1S)$ and $\Upsilon(1S)$ mesons, which are defined in Section 4.1.1. The acceptance is obtained via an unpolarized Monte Carlo sample including only muons coming from $J/\Psi(1S)$, $\Upsilon(1S)$, $\Upsilon(2S)$ and $\Upsilon(3S)$ decays. The acceptance is defined as the fraction of the number of detectable events $N_{\mathrm{Det}}(p_T, y)$ in a given (p_T, y) bin of $J/\Psi(1S)$ or $\Upsilon(1S)$ divided by the corresponding number of generated events $N_{\mathrm{Gen}}(p_T, y)$ in the MC simulation (see Eq. 4.7). For both numbers the generated muon kinematical properties are taken to avoid binning effects.

$$\mathscr{A}(p_T, y) = \frac{N_{Det}(p_T, y)}{N_{Gen}(p_T, y)} \tag{4.7}$$

The reconstructed muons are matched to generated muons within a cone[1] of $\Delta R < 0.05$.

The acceptance depends on the polarization of the $J/\Psi(1S)$ and $\Upsilon(1S)$ meson, which affects the kinematical properties of the muons. For this analysis only the unpolarized scenario is used. In Fig. 4.12 the unpolarized $J/\Psi(1S)$ and $\Upsilon(1S)$ acceptance in dependence of $|y|$ and p_T is shown. The difference at low momentum for $J/\Psi(1S)$ and $\Upsilon(1S)$ arises from the different kinematics of the daughter muons due to the mass difference of the mesons. The muons coming from $\Upsilon(1S)$ decays have enough momentum (E ~ 5 GeV) to pass the minimum p_T cut, but for the lower $J/\Psi(1S)$ mass the muons do not reach the muon chambers. In the $\Upsilon(1S)$ acceptance, the dip at around 5 GeV/c - half of the $\Upsilon(1S)$ mass, comes from events where one of the muons is boosted in opposite direction to the $\Upsilon(1S)$. In these events the muon energy is too low and the muon do not reach the muon chambers (see the right plot in Fig. 4.13). At higher p_T the trailing muon is getting enough boost to meet the p_T cut of the muon detector acceptance more often again. The unpolarized $\Upsilon(1S)$ acceptance integrated over p_T as a function of $|y|$ is shown in Fig. 4.13 to motivate the rapidity cut $|y| < 2$ for the $\Upsilon(1S)$ analysis, hence the acceptance decreases in this region. The acceptance values in p_T bins are presented in Appendix B.

[1] The ΔR is defined as: $\Delta R = \sqrt{(\Delta\eta)^2 + (\Delta\varphi)^2}$, where $\Delta\eta$ and $\Delta\varphi$ is the distance between the generated and reconstructed muon in η and φ, respectively.

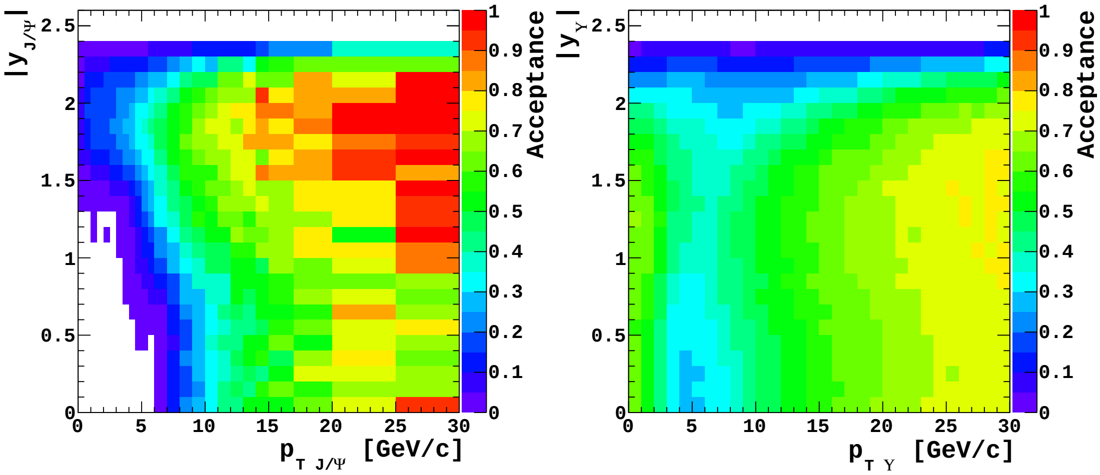

Figure 4.12: *Unpolarized* $J/\Psi(1S)$ *(left) and* $\Upsilon(1S)$ *(right) acceptance in dependence of* $|y|$ *and* p_T.

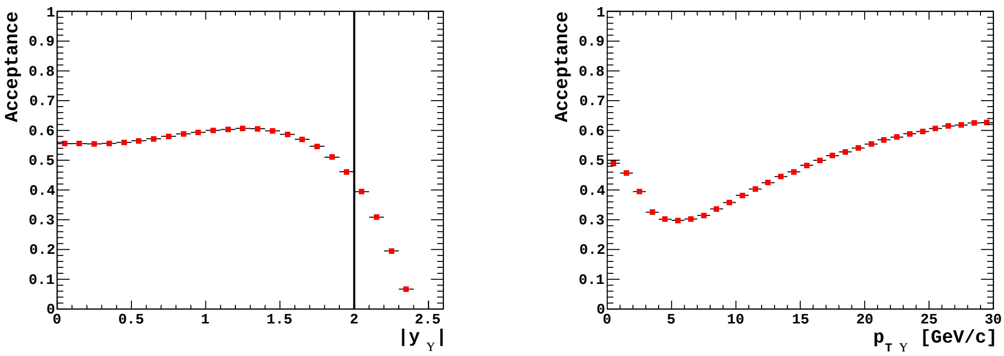

Figure 4.13: *Unpolarized* $\Upsilon(1S)$ *acceptance integrated over* p_T *as a function of* $|y|$ *(left) and integrated over* $|y|$ *as a function of* p_T *(right).*

4.3 Efficiency

The efficiency measurements used for the final cross section results are related to instrumental effects. The efficiency gives the number of how many $J/\Psi(1S)$ or $\Upsilon(1S)$ events are surviving due to the reconstruction algorithms, trigger or track quality cuts. The overall efficiency for a $J/\Psi(1S)$ and $\Upsilon(nS)$ meson ($Q\bar{Q}$), respectively is defined as:

$$\varepsilon^{Q\bar{Q}}(p_T,\eta) = (\varepsilon^{\mu}_{\text{reco}}(p_T,\eta))^2 \cdot \varepsilon^{Q\bar{Q}}_{\text{trigger}}(p_T,\eta) \tag{4.8}$$

where $\varepsilon^{\mu}_{\text{reco}}(p_T,\eta)$ is the reconstruction efficiency for a muon. This is the probability that a muon passing all muon requirements is found. The trigger efficiency $\varepsilon^{Q\bar{Q}}_{\text{trigger}}(p_T,\eta)$ is the probability that the detected dimuon event fires the double muon trigger.

The efficiencies are all determined using the **tag and probe** method. This is a data driven method that do not rely on MC simulations and therefore different theoretical approaches have no influence. In the tag and probe method a well identified muon (called **tag**) is combined with a second object in the event (called **probe**) and the invariant mass is computed. The invariant mass is required to be in a certain mass window around the resonance under consideration. The probes that fulfill the criteria under consideration are labeled as **selected probes**. The efficiency ε than is the number of selected probes n divided by the total number of probes N. In each case the number of $Q\bar{Q}$ events is obtained by a fit to the dimuon invariant mass distribution in order to substract the background:

$$\varepsilon = \frac{n}{N}, \qquad \sigma_\varepsilon = \frac{1}{N}\sqrt{N\varepsilon(1-\varepsilon)} = \sqrt{\frac{n(N-n)}{N^3}}, \tag{4.9}$$

where σ_ε is the statistical uncertainty given by the binomial error.

4.3.1 $J/\Psi(1S)$ Reconstruction Efficiency

In this analysis only global muons are considered to determine the cross sections. The reconstruction efficiency $\varepsilon^{\mu}_{\text{reco}}(p_T,\eta)$ for a global muon is the probability that a track in the tracker $\varepsilon^{\mu}_{\text{track}}(p_T,\eta)$ is found and that this track is matched to a muon object $\varepsilon^{\mu}_{\text{muon id}}(p_T,\eta)$ detected in the muon chambers. The reconstruction efficiency is determined using different disjoint probe categories to assure, that all kind of muons are treated and a fit is performed to the invariant mass of each category separately [35].

The reconstruction efficiency can be defined as:

$$\varepsilon^{\mu}_{\text{reco}}(p_T,\eta) = \epsilon^{\mu}_{\text{track}}(p_T,\eta) \cdot \epsilon^{\mu}_{\text{muon id}}(p_T,\eta) \tag{4.10}$$

$$= \varepsilon^{\mu}_{\text{track}}(p_T,\eta) \cdot \varepsilon^{\mu}_{\text{match}}(p_T,\eta) \cdot \varepsilon^{\mu}_{\text{standalone}}(p_T,\eta), \tag{4.11}$$

where $\varepsilon^{\mu}_{\text{track}}(p_T,\eta)$ is the efficiency for a muon candidate in the silicon tracker within the track quality cuts and $\varepsilon^{\mu}_{\text{standalone}}(p_T,\eta)$ is the efficiency for a muon candidate in the muon chambers, which is then matched correctly $\varepsilon^{\mu}_{\text{match}}(p_T,\eta)$ to a global muon.

A **tag** is defined as a muon, that is both tracker and global muon with a $p_T \geq 3$ GeV/c to ensure a well reconstructed muon. One **tag** muon is selected for the whole event. The muon has to satisfy all muon requirements, kinematical acceptance cuts and track quality cuts mentioned in Section 4.1.1. The same applies for the **probe** candidate, if possible: e.g. a standalone muon does not have to satisfy the track quality cuts for the inner tracker track. This means that the track quality cut efficiency is included in the tracking efficiency (compare Appendix D). All **probe** candidates are required to have an opposite charge sign compared to the **tag** candidate. The invariant mass of the **probe** and the **tag** have to be in a mass window around 1 GeV/c^2 with respect to the PDG value [9]. The different **probe** categories are summarized in Table 4.6.

Probe type	Definition	x
Golden	a global muon satisfying tag criteria is found	G
Matched	a global muon is found, but does not satisfy tag criteria	M
Unmatched	track and standalone muon exist, but no global muon is found	U
Tracker only	only a tracker track is found	T
Standalone only	only a standalone muon is found	S

Table 4.6: *Probe types and their definitions used to obtain the reconstruction efficiency [35].*

If the **probe** muon also meets the criteria of a tag muon this probe category is defined as a **golden** (G) probe. The second probe type is the **matched** (M) probe category, where the probe muon is global and tracker, but does not satisfy the transverse momentum cut of the golden category. If the muon probe candidate is a standalone muon only and can be matched to a tracker track with the same charge sign within a cone of $\Delta R < 0.3$ this probe is added to the **unmatched** (U) probe category. Otherwise this probe candidate falls into the **standalone only** (S) category. The last probe category is the **tracker only** one (T), where all tracker tracks, which can not be matched to another muon are stored. The tracks are required to fulfill all track quality cuts and have opposite charge to the tag muon.

These probe categories are used to obtain the standalone, tracker and matching efficiency using the following equations [35].

$$\epsilon_{standalone} = \frac{2N_{GG}+N_{GM}+N_{GU}}{2N_{GG}+N_{GM}+N_{GU}+N_{GT}} \tag{4.12}$$

$$\epsilon_{tracker} = \frac{2N_{GG}+N_{GM}+N_{GU}}{2N_{GG}+N_{GM}+N_{GU}+N_{GS}} \tag{4.13}$$

$$\epsilon_{matching} = \frac{2N_{GG}+N_{GM}}{2N_{GG}+N_{GM}+N_{GU}} \tag{4.14}$$

where N_{Gx} corresponds to the tag and probe events containing a probe of type x (see Table 4.6). The factor 2 corresponds to the fact that in the golden category, the tag can also be a probe and vice versa. This method obtains the same results as if one would require e.g. for the standalone efficiency, a tracker track as a probe and a global muon as a selected probe. In contrast the used method assures that every probe category and its mass resolution is treated correctly. The number of events is obtained by a fit to the invariant mass distribution, where the signal is described by a Gauß-function and the background is described by a polynom function of 1st or 2nd order. If the statistic in a certain $\eta - p_T$ bin is large enough the number of events is obtained by using the same method, which is also used to obtain the yield of the cross section described in Section 4.1.1. This method is used in order to account for the tail of the dimuon invariant mass distribution due to final state radiation.

For the reconstruction efficiency another HLtrigger has to be used in order not to bias the reconstruction efficiency. For the muon related efficiencies ($\epsilon_{standalone}$ and $\epsilon_{matching}$) the *HLT_Mu5_Track0_Jpsi* trigger path is used, which requires any kind of muon with a $p_T > 5$ GeV/c and a track only without any p_T cut, but unbiased with respect to the muon system. The invariant mass of the muon and the track is required to be $2.5 < M_{inv} < 4.1$ GeV/c^2. The track related efficiencies ($\epsilon_{tracker}$ with track quality cut efficiency) is measured by using a dataset selected by the *HLT_Mu5_L2Mu0* trigger path, which requires any muon with a $p_T > 5$ GeV/c and a second muon object only identified in the muon chamber. Both HLT triggers have high prescales, therefore RUN A+RUN B combination and only four p_T bins are used to ensure that the statistic in all probe categories is reasonably high. The whole approach to obtain the reconstruction efficiency is obtained for both HLT triggers exclusively to avoid errors coming from prescales. This means, that the Golden, Matched and Unmatched category is filled for both HLT triggers separatly. The standalone category is only filled for the *HLT_Mu5_L2Mu0* trigger and the tracker category with events fired by the *HLT_Mu5_Track0_Jpsi* trigger. The number of events in each category and all invariant mass fits can be found in Appendix C. The tag and probe method is also performed with the MC samples listed in Table 4.1 to cross check the resulting reconstruction efficiency.

The tracking efficiency in the different η regions in dependence of the p_T of the probe muon can be found in Fig. 4.14 (and values in Appendix C). In the barrel region in the first p_T bin

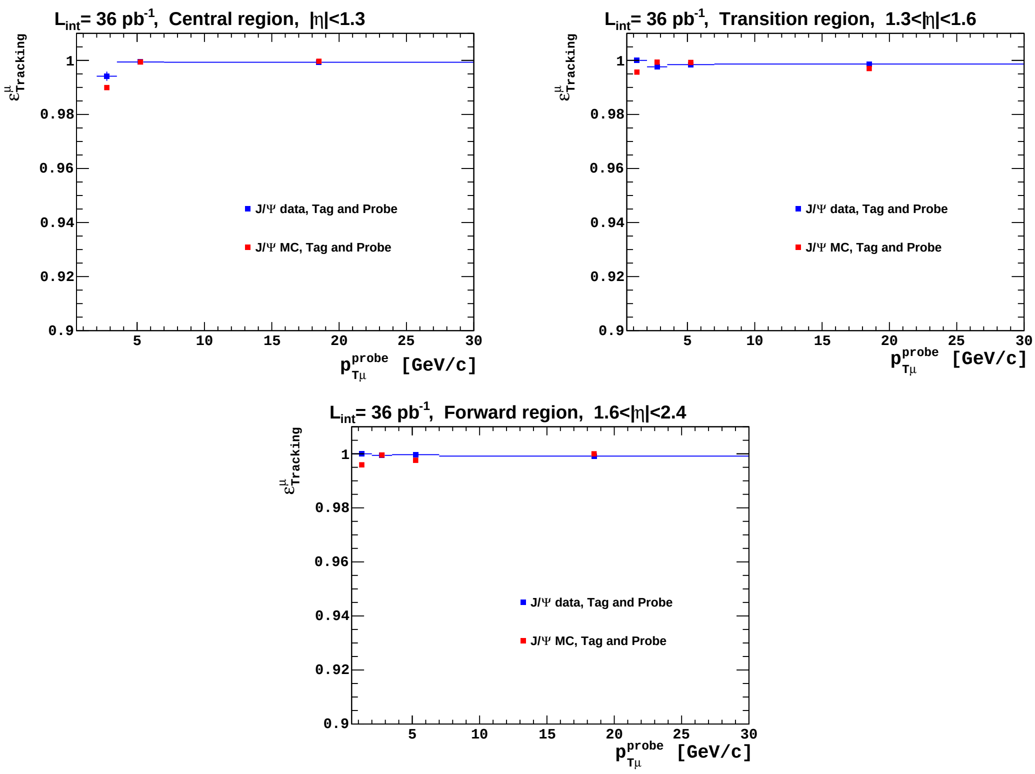

Figure 4.14: *Tracking efficiency using the* J/Ψ(1S) *resonance determined by the tag and probe method with 36* pb^{-1} *of CMS data.*

the standalone muons, which are used to obtain the tracking efficiency, have not enough energy to reach the muon chambers. In the transition and forward region in the same transverse momentum range standalone muons are detected, but the statistic is too low in comparison to the other probe categories, therefore the efficiency in this region is 100 %. The tracking efficiency exceeds in all bins 99 %, which points to the excellent performance of the tracker detector for muons in CMS.

In Fig. 4.15 (and values in Appendix C) the matching efficiency in the different η regions in dependence of the p_T of the probe muon is shown. In the central region for a p_T<2.0 GeV/c the muons have not enough energy to be detected by the muon chambers, therefore this bin is empty. In the subsequent bins in the unmatched category the statistic is too low, due to this the matching efficiency raises to 100 %. The matching efficiency transcends in all bins 99 % and stands for the good performance of the muon matching algorithms in CMS.

The standalone efficiency, shown in Fig. 4.16 (and values in Appendix C), is the probability that a muon leaves a track in the muon chambers. The leading probe category for the standalone efficiency is the tracker only category. The standalone efficiency is lower than

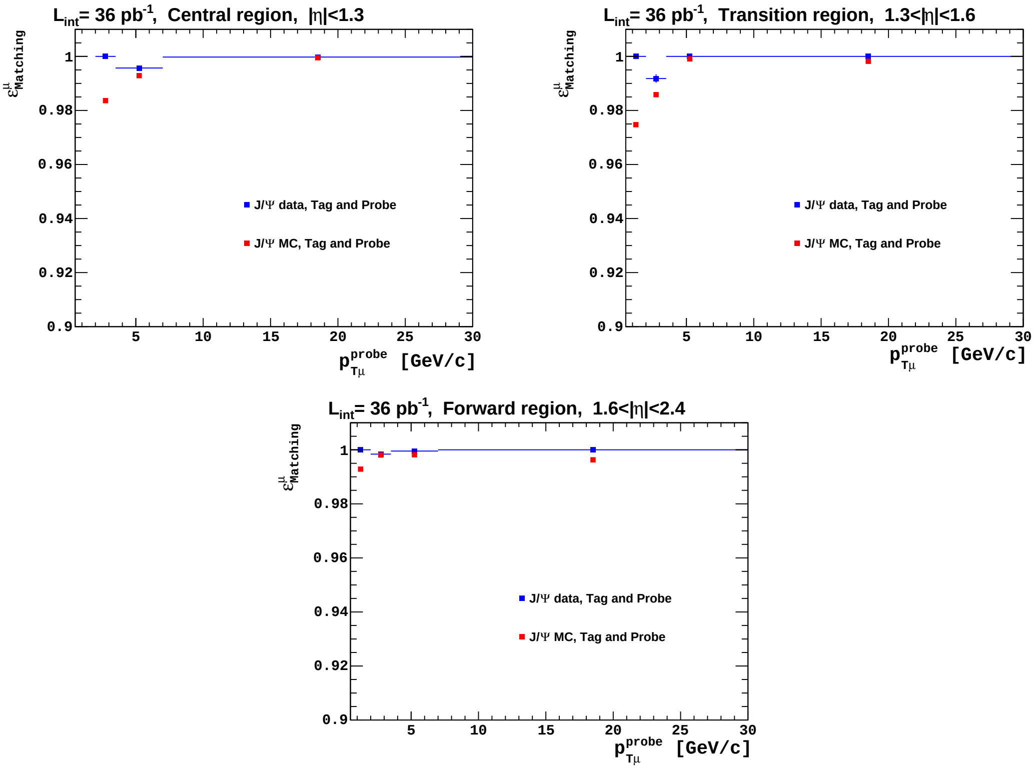

Figure 4.15: *Matching efficiency using the* J/Ψ(1S) *resonance determined by the tag and probe method with 36* pb^{-1} *of CMS data.*

the tracking efficiency due to the higher performance of the silicon tracker and the fact, that the silicon tracker is closer to the interaction point and lower momentum muons can reach the tracker. The standalone efficiency dominates the whole muon reconstruction efficiency. The discrepancies of the standalone efficiency (see Fig. 4.16) in the central region in comparison to the same method obtained with MC signal samples causes the discrepancies in the reconstruction efficiency in the central region in comparison to MC simulations.

The muon reconstruction efficiency is obtained by multiplying the tracking, matching and standalone efficiency. The statistical uncertainty of the reconstruction efficiency is propageted from the binomial errors of each efficiency. The reconstruction efficiency in all detector regions in dependence of the p_T of the probe muon compared to MC Truth and MC Tag and Probe is presented in Fig. 4.17. The MC Truth is obtained by the prompt and non-prompt J/Ψ(1S) signal MC samples, where the generator information of the muon is used to ensure that the reconstructed muon is coming from a J/Ψ(1S) decay. The number of matched reconstructed muons is divided by the corresponding number of generated muons from J/Ψ(1S) decays. All track quality cuts are applied for the reconstructed muon to obtain the MC Truth reconstruction and track quality cut efficiency at the same time.

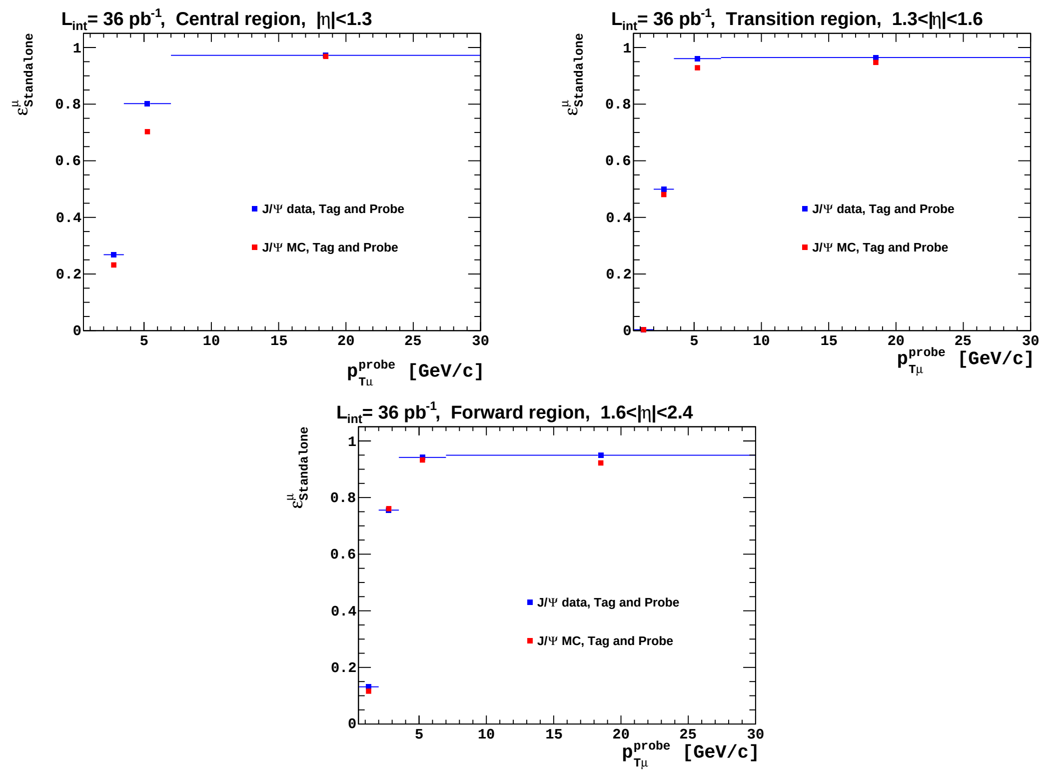

Figure 4.16: *Standalone efficiency using the* $J/\Psi(1S)$ *resonance determined by the tag and probe method with 36* pb^{-1} *of CMS data.*

It has to be taken into account, that for the MC Tag & Probe efficiencies the statistic in the MC samples is quite low (compare Table 4.1). Regarding statistical uncertainties only the MC Truth and the MC Tag & Probe values lie within an 1 σ range, which shows the reliability of the tag and probe method. For this reason the statistical uncertainty from tag and probe in data is taken as a systematic uncertainty in the resulting cross section measurements. The reconstruction efficiency with the uncertainties can be found in Table 4.7.

p_T^μ [GeV/c]	$\|\eta^\mu\| < 1.3$	$\Delta_{MC\ T\&P-Data\ T\&P}$	$\Delta_{MC\ Truth-Data\ T\&P}$
2.0-3.5	26.67 ± 0.83	4.36	5.78
3.5-7.0	79.90 ± 0.22	10.22	12.14
7.0-30.0	97.18 ± 0.15	0.39	0.86
p_T^μ [GeV/c]	$1.3 < \|\eta^\mu\| < 1.6$	$\Delta_{MC\ T\&P-Data\ T\&P}$	$\Delta_{MC\ Truth-Data\ T\&P}$
0.5-2.0	0.34 ± 0.08	0.02	0.12
2.0-3.5	49.53 ± 0.61	2.17	0.59
3.5-7.0	95.97 ± 0.24	3.26	2.00
7.0-30.0	96.44 ± 0.35	2.06	0.82
p_T^μ [GeV/c]	$1.6 < \|\eta^\mu\| < 2.4$	$\Delta_{MC\ T\&P-Data\ T\&P}$	$\Delta_{MC\ Truth-Data\ T\&P}$
0.5-2.0	13.32 ± 0.26	0.02	0.42
2.0-3.5	75.57 ± 0.44	2.17	1.43
3.5-7.0	94.13 ± 0.24	3.26	2.56
7.0-30.0	94.90 ± 0.36	2.06	1.09

Table 4.7: *Reconstruction efficiency in % obtained by the tag and probe method for the* $J/\Psi(1S)$ *resonance in bins of* η *and* p_T *of the probe muon in data, where the uncertainty is statistical and the difference between MC tag and probe (T&P) and the MC Truth with respect to the efficiency obtained by data.*

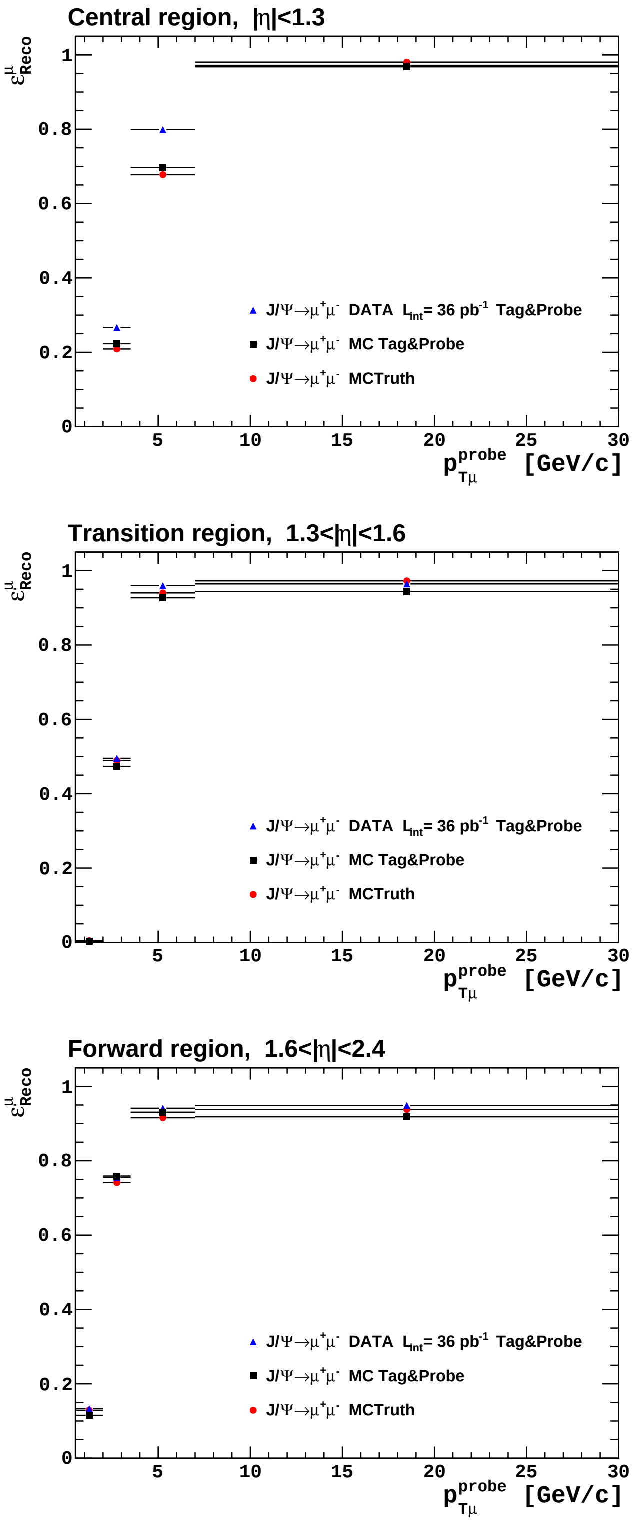

Figure 4.17: *Reconstruction efficiency using the* $J/\Psi(1S)$ *resonance determined by the tag and probe method with 36* pb^{-1} *of CMS data compared to MC Truth.*

4.3.2 Υ(1S) Reconstruction Efficiency

Due to the available offline trigger at this stage of data taking, the reconstruction (and track quality cut) efficiency for the Υ(1S) analysis is performed using the reconstruction efficiency obtained with the J/Ψ(1S) resonance. The J/Ψ(1S) reconstruction efficiency is weighted using a map determined by dividing the MC Truth reconstruction efficiency for Υ(1S) and J/Ψ(1S) . This is done to take the different p_T distributions of muons from J/Ψ(1S) and Υ(1S) decays into account:

$$\varepsilon^{\mu}_{reco\ data\ \Upsilon(1S)} = \frac{\varepsilon^{\mu}_{reco\ MC\ \Upsilon(1S)}}{\varepsilon^{\mu}_{reco\ MC\ J/\Psi(1S)}} \cdot \varepsilon^{\mu}_{reco\ data\ J/\Psi(1S)} \tag{4.15}$$

The map used to obtain the Υ(1S) reconstruction efficiency is shown in Fig. 4.18.

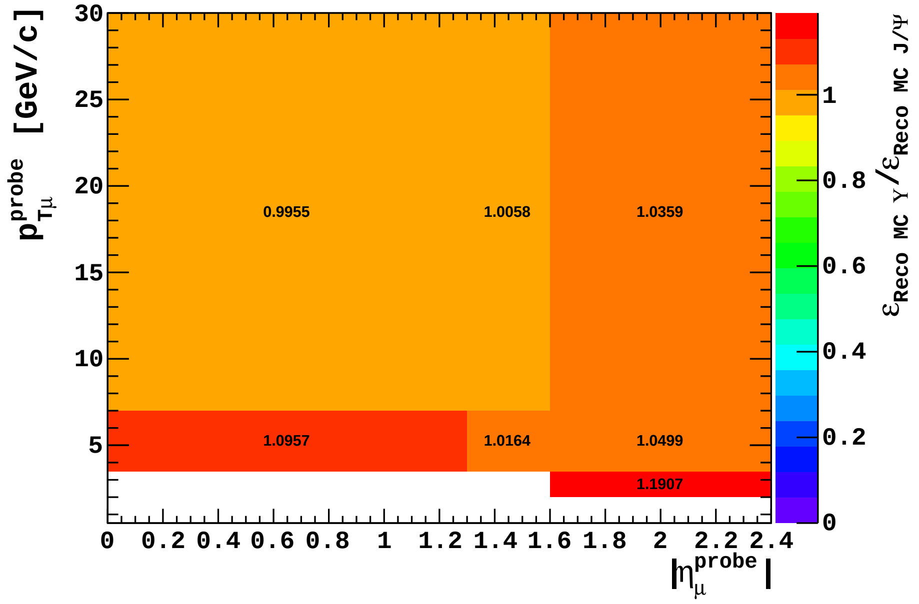

Figure 4.18: *MC Truth reconstruction map needed to obtain the* Υ(1S) *reconstruction efficiency.*

The determined values for the Υ(1S) reconstruction efficiency are shown in Fig. 4.19, where the MC Truth reconstruction efficiency for both J/Ψ(1S) and Υ(1S) , respectively, and the used data driven efficiencies are shown. The Υ(1S) reconstruction efficiency can additional be found in Table 4.8, where the second uncertainty refers to the difference to the Υ(1S) MC Truth reconstruction efficiency. As expected from the J/Ψ(1S) reconstruction efficiency the largest differences are in the barrel region. The statistical uncertainties from the weighted

J/Ψ(1S) reconstruction efficiency are used as a systematic uncertainty in the resulting ϒ(1S) cross section measurement.

p_T^{μ} [GeV/c]	$\lvert\eta^{\mu}\rvert < 1.3$	$\Delta_{MC\ Truth-Data\ T\&P}$
2.0-3.5	-	-
3.5-7.0	87.55 ± 0.25	13.30
7.0-30.0	96.74 ± 0.15	0.86
	$1.3<\lvert\eta^{\mu}\rvert < 1.6$	$\Delta_{MC\ Truth-Data\ T\&P}$
2.0-3.5	-	-
3.5-7.0	97.54 ± 0.24	1.99
7.0-30.0	96.99 ± 0.35	0.83
	$1.6 < \lvert\eta^{\mu}\rvert < 2.4$	$\Delta_{MC\ Truth-Data\ T\&P}$
2.0-3.5	89.98 ± 0.52	1.71
3.5-7.0	98.83 ± 0.25	2.69
7.0-30.0	98.30 ± 0.37	1.13

Table 4.8: *Reconstruction efficiency for* ϒ(1S) *in % using the weighted* J/Ψ(1S) *reconstruction efficiency values determined by the tag and probe method with 36* pb^{-1} *of CMS data. The uncertainty is statistical and the second column refers to the difference with respect to the* ϒ(1S) *MC Truth reconstruction efficiency.*

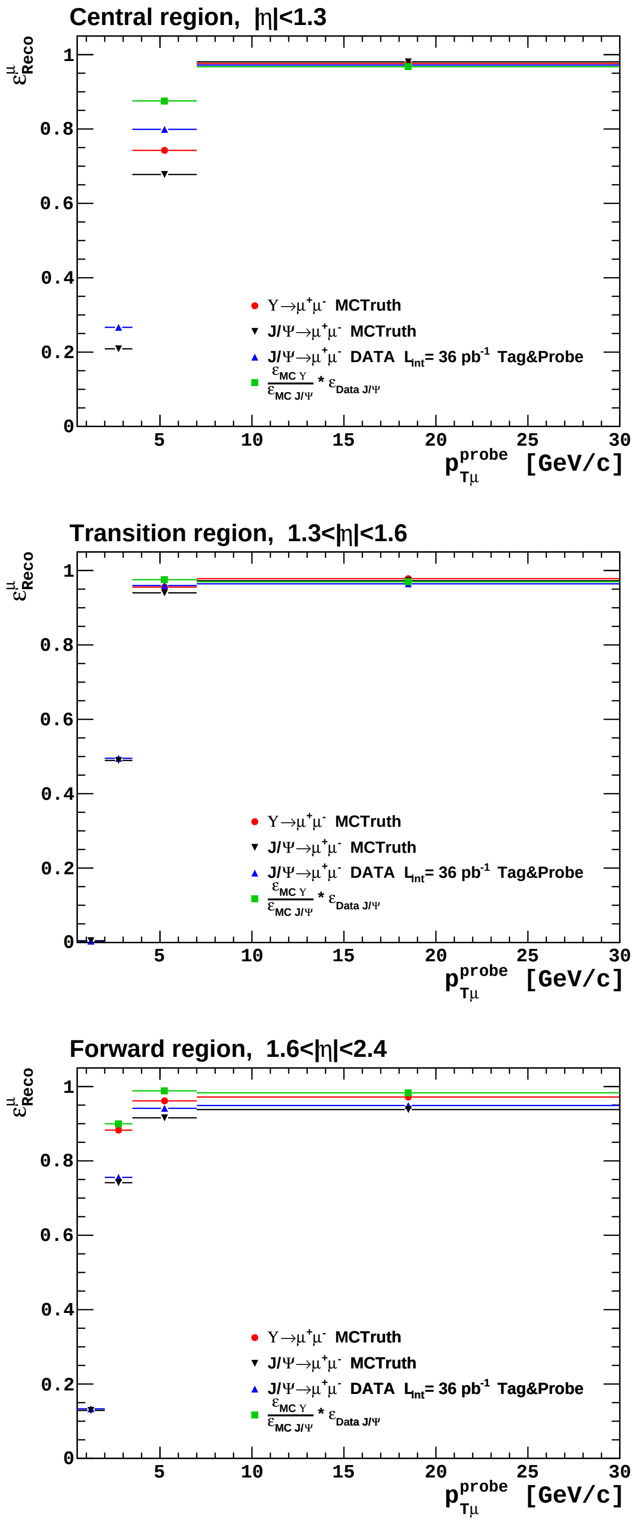

Figure 4.19: *Reconstruction efficiency for* $\Upsilon(1S)$ *using the* $J/\Psi(1S)$ *resonance determined by the tag and probe method with 36* pb^{-1} *of CMS data compared to MC Truth.*

4.3.3 $\mathrm{J}/\Psi(1\mathrm{S})$ Trigger Efficiency

The efficiency for the double muon trigger, which is used in this analysis, is obtained using another dataset in order not to be biased by the trigger selection. In the beginning of LHC data taking the muon trigger efficiency was obtained using a single muon trigger skimmed dataset, but hence the only remaining “single” muon trigger in this stage of data taking requires additional tracks or muons around the Jpsi mass, this would cause a bias on the double muon trigger efficiency. The dataset used for the trigger efficiency measurement in this analysis requires an electron or a jet trigger. Therefore it is orthogonal to the muon trigger under study.

The trigger efficiency is defined as:

$$\epsilon_{trigger,J/\Psi}(p_T^{\mathrm{J}/\Psi(1\mathrm{S})}) = \frac{N_{trigger}(p_T^{\mathrm{J}/\Psi(1\mathrm{S})})}{N(p_T^{\mathrm{J}/\Psi(1\mathrm{S})})}, \tag{4.16}$$

where $N(p_T^{\mathrm{J}/\Psi(1\mathrm{S})})$ is the number of reconstructed $\mathrm{J}/\Psi(1\mathrm{S})$ events in a given $p_T^{\mathrm{J}/\Psi(1\mathrm{S})}$ bin. The reconstructed muons have to fulfill the same criteria mentioned in Section 4.1.1. $N_{trigger}(p_T^{\mathrm{J}/\Psi(1\mathrm{S})})$ is the number of events in which the double muon Trigger fired.

The double muon triggers used in this analysis are the *HLTDoubleMu0* or the former replacing *HLTDoubleMu0_Quarkonium* HLT trigger (see Section 4.1). Due to the low statistic in the dataset (less than 10000 events in total) the trigger efficiency is only studied in dependence of the transverse momentum. In the MC simulation only the *HLTDoubleMu0* trigger path is included, but hence the *HLTDoubleMu0_Quarkonium* requires only additional a mass window cut of $1.5 < M_{inv} < 14.5$ GeV/c^2 , this has no effect in the comparison between data and MC. The number of events in each $p_T^{\mathrm{J}/\Psi(1\mathrm{S})}$ bin is determined fitting the dimuon invariant mass distribution. The fit function contains a Gauß function for the signal and a line function for the backround. All fits can be found in Appendix E.

The trigger efficiency as a function of $p_T^{\mathrm{J}/\Psi(1\mathrm{S})}$ of the $\mathrm{J}/\Psi(1\mathrm{S})$ resonance is shown in Fig. 4.20. Regarding statistical uncertainties only the MC trigger efficiency lies within a 2-5 σ range in comparison to the data.

One possible explanation for this discrepancy could be that the double muon trigger is not correctly described in the MC simulation. Another source of the discrepancy could also be a physical bias in the trigger efficiency measurements due to different datasets, electron and jet datasets. The later has been checked by using compatible MC signal samples and then fitting to the dimuon invariant mass distributions in the $\mathrm{J}/\Psi(1\mathrm{S})$ mass window. Due to low statistics in these MC datasets, a clear explanation about the discrepancy could not be given.

The statistical uncertainty in data is taken as systematics in the cross section measurements. The trigger efficiency is summarized in Table 4.9.

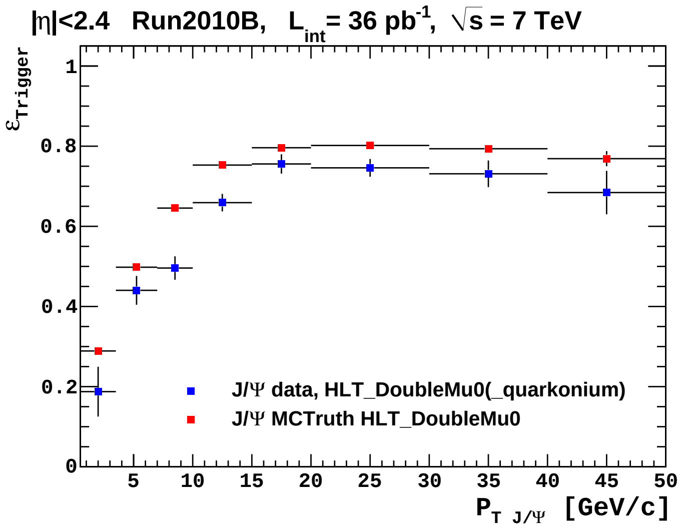

Figure 4.20: *Double muon trigger efficiency using the* $\mathrm{J}/\Psi(1\mathrm{S})$ *resonance in a dataset selected by electron and jet trigger to not bias the double muon trigger efficiency obtained with* $36\,\mathrm{pb}^{-1}$ *of CMS data compared to MC Truth.*

$p_T^{J/\Psi}$ [GeV/c]	$\lvert\eta^{J/\Psi}\rvert < 2.4$	$\Delta_{MC\ Truth-Data\ T\&P}$
0.5-3.5	18.75 ± 6.22	10.15
3.5-7.0	44.03 ± 3.59	5.77
7.0-10.0	49.56 ± 2.92	14.96
10.0-15.0	65.91 ± 2.19	9.37
15.0-20.0	75.56 ± 2.41	4.05
20.0-30.0	74.59 ± 2.21	5.58
30.0-40.0	73.11 ± 3.32	6.25
40.0-50.0	68.43 ± 5.42	8.46

Table 4.9: *Trigger efficiency* $\varepsilon_{Trigger}(p_T^{\mathrm{J}/\Psi(1\mathrm{S})})$ *in % in bins of* $p_T^{\mathrm{J}/\Psi(1\mathrm{S})}$ *of the* $\mathrm{J}/\Psi(1\mathrm{S})$ *resonance, where the uncertainty is statistical and the second column shows the difference to the* $\mathrm{J}/\Psi(1\mathrm{S})$ *MC Truth trigger efficiency.*

4.3.4 $\Upsilon(1S)$ Trigger Efficiency

The trigger efficiency for the $\Upsilon(1S)$ analysis is obtained as for the reconstruction efficiency using the data driven $J/\Psi(1S)$ trigger efficiency weighted by the MC Truth trigger efficiency to take the different kinematics of the $J/\Psi(1S)$ and $\Upsilon(1S)$ mesons into account. The used map in p_T dependence is shown in Fig. 4.21.

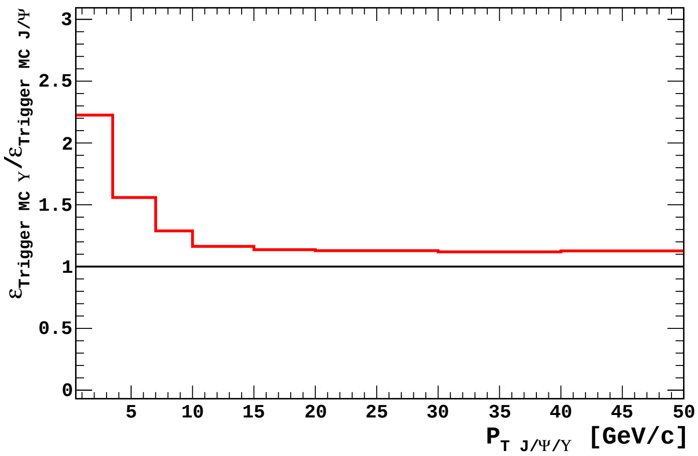

Figure 4.21: *MC Truth trigger efficiency map needed to obtain the* $\Upsilon(1S)$ *double muon trigger efficiency.*

The resulting double muon trigger efficiency for $\Upsilon(1S)$ compared to the trigger efficiency in MC can be found in Fig. 4.22 and Table 4.10. Due to the used method to obtain the $\Upsilon(1S)$ trigger efficiency the MC Truth trigger efficiency varies similarly to the $J/\Psi(1S)$ trigger efficiency in comparison to data. As a systematic uncertainty for the cross section measurements the statistic uncertainty is taken.

$p_T^{\Upsilon(1S)}$ [GeV/c]	$\lvert\eta^{\Upsilon(1S)}\rvert < 2.4$	$\Delta_{MC\ Truth-Data\ T\&P}$
0.5-3.5	41.73 $\pm$ 13.84	22.60 ,
3.5-7.0	68.63 $\pm$ 5.60	8.99
7.0-10.0	63.91 $\pm$ 3.77	19.27
10.0-15.0	76.68 $\pm$ 2.54	10.91
15.0-20.0	85.89 $\pm$ 2.74	4.60
20.0-30.0	84.19 $\pm$ 2.50	6.30
30.0-40.0	81.81 $\pm$ 3.72	6.99
40.0-50.0	77.10 $\pm$ 6.11	9.53

Table 4.10: *Trigger efficiency $\varepsilon_{Trigger}(p_T^{\Upsilon(1S)})$ in % in bins of $p_T^{\Upsilon(1S)}$ of the $\Upsilon(1S)$ resonance, where the uncertainty is statistical and the second column shows the difference to the $\Upsilon(1S)$ MC Truth trigger efficiency.*

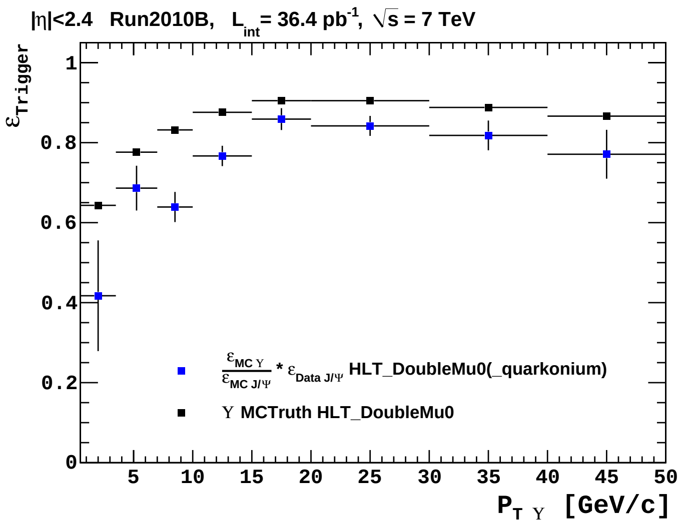

Figure 4.22: *double muon $\Upsilon(1S)$ trigger efficiency using the $J/\Psi(1S)$ resonance with 36 pb^{-1} of CMS data compared to MC Truth.*

CHAPTER 5

Results

The number of $Q\bar{Q}$ mesons ($\mathrm{J}/\Psi(1\mathrm{S})$ and $\Upsilon(\mathrm{nS})$ respectively) is obtained using weighted dimuon invariant mass distributions. The invariant mass distribution is weighted event-by-event with the factor $1/w$, which depends on the kinematical properties of the $Q\bar{Q}$ resonance and both daughter muons. The weighting factor takes the acceptance and detection efficiency in the bin under consideration into account. The average weighting factor $1/w$ for $Q\bar{Q}$ can be seen in Fig. 5.1.

$$w = \varepsilon^{Q\bar{Q}}(p_T,\eta)\cdot\mathscr{A}(p_T,y) \tag{5.1}$$

$$= \left(\varepsilon^{\mu_1}_{\mathrm{reco}}\cdot\varepsilon^{\mu_2}_{\mathrm{reco}}\right)\cdot\varepsilon^{Q\bar{Q}}_{\mathrm{trigger}}\cdot\mathscr{A} \tag{5.2}$$

5.1 Inclusive differential and total $\mathrm{J}/\Psi(1\mathrm{S})$ Cross Section

The number of $\mathrm{J}/\Psi(1\mathrm{S})$ mesons is obtained using the method explained in Section 4.1.1. The values are summarized in Table 5.1, where the uncertainty is statistical and contains also the uncertainty on the yield extraction method. For all $p_T^{\mathrm{J}/\Psi(1\mathrm{S})}$ and $|y^{\mathrm{J}/\Psi(1\mathrm{S})}|$ bins the fits can be found in Appendix F.

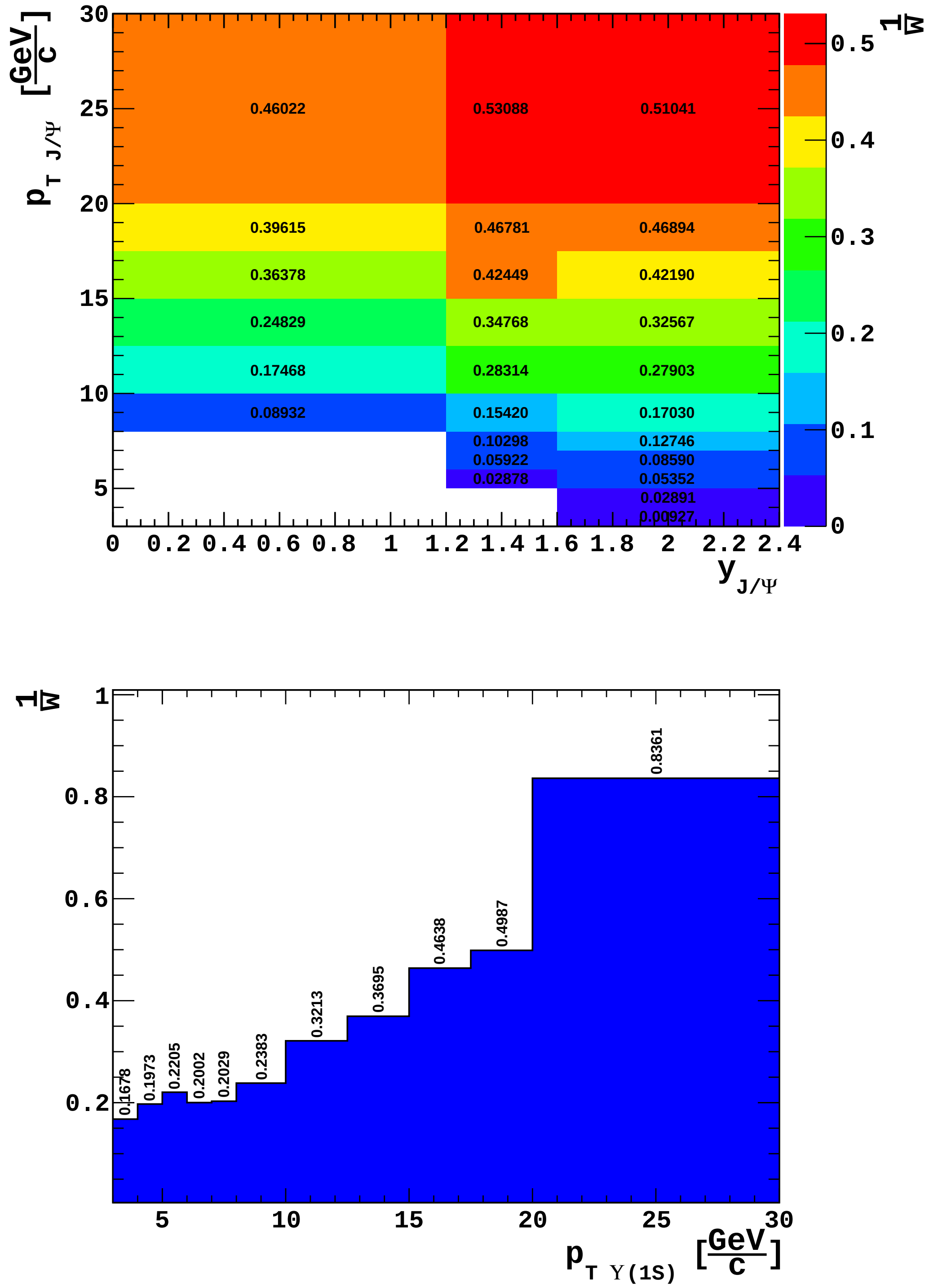

Figure 5.1: *Average weighting factor* $1/w$ *in dependence of the bins used in the* $J/\Psi(1S)$ *and* $\Upsilon(1S)$ *analysis, respectively.*

$p_T^{J/\Psi}$ [GeV/c]	$\lvert y^{J/\Psi}\rvert < 1.2$	$1.2 < \lvert y^{J/\Psi}\rvert < 1.6$	$1.6 < \lvert y^{J/\Psi}\rvert < 2.4$
3.0-4.0	-	-	3617200 ± 6741
4.0-5.0	-	-	2043700 ± 2662
5.0-6.0	-	553027 ± 1467	1237880 ± 2398
6.0-7.0	-	451812 ± 1025	701421 ± 1312
7.0-8.0	-	258234 ± 546	369234 ± 830
8.0-10.0	489813 ± 819	254798 ± 588	328773 ± 765
10.0-12.5	275250 ± 572	82586 ± 317	108267 ± 402
12.5-15.0	109325 ± 356	29653 ± 187	381412 ± 229
15.0-17.5	39379 ± 214	11148 ± 114	12745 ± 128
17.5-20.0	20188 ± 153	4989 ± 76	5370 ± 79
20.0-30.0	20717 ± 155	5087 ± 76	5002 ± 79

Table 5.1: *Measured weighted yield with the statistical uncertainty.*

The differential cross section in dependence of $p_T^{\mathrm{J}/\Psi(1\mathrm{S})}$ and $y^{\mathrm{J}/\Psi(1\mathrm{S})}$ is calculated via eq. 2.2 in Section 2.2.2. The number is normalized to the integrated luminosity $\int \mathscr{L}$ and the transverse momentum $\Delta p_T^{\mathrm{J}/\Psi(1\mathrm{S})}$ and rapidity bin size $\Delta y^{\mathrm{J}/\Psi(1\mathrm{S})}$.

The results are presented in Fig. 5.2 for all rapidity regions. The uncertainties in the plot are the statistical and systematical ones added in quadrature, where the luminosity uncertainty is not included. The systematics are obtained from the statistical uncertainty of the different efficiencies. The cross section is calculated again using the efficiencies shifted up and down by their statistical uncertainty. The systematic uncertainty related to the momentum scale correction is calculated by taking the difference in the cross section between the yield with and without the applied momentum scale correction. In the barrel region the daughter muons of the J/Ψ(1S) meson need more energy to reach the muon chambers in comparison to the forward region. Additional the weighting factor in the first p_T-bins are really high due to the low efficiencies in these p_T-regions (see Section 4.3). Fits to the weighted dimuon invariant mass distribution in this regions are complicated. Therefore in the barrel region the differential cross section starts at 8 GeV/c , in the transition region at 5 GeV/c and in the forward region at 3 GeV/c . The lower transverse momentum regions could be reached using tracker muons separately.

The total cross section is derived by integrating over all transverse momentum and rapidity bins:

$$\sigma_{tot}\left(pp \to \mathrm{J}/\Psi(1\mathrm{S})X\right) \cdot \mathscr{BR}\left(\mathrm{J}/\Psi(1\mathrm{S}) \to \mu^+\mu^-\right) = \int_y dy \int_{p_T} dp_T \frac{d^2\sigma}{dy\,dp_T} \tag{5.3}$$

All cross section values in a certain bin are summed up and multiplied by their rapidity and transverse momentum bin size.

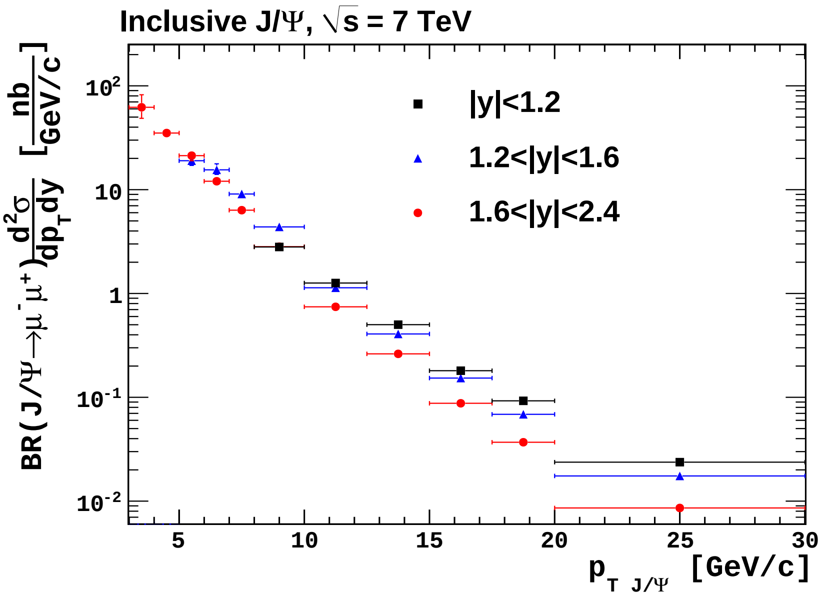

Figure 5.2: *Inclusive differential cross section for the* J/Ψ(1S) *meson as a function of* $p_T^{\mathrm{J}/\Psi(1\mathrm{S})}$ *for all rapidity regions.*

The total inclusive production cross section in a rapidity range of $|y| < 2.4$ and a transverse momentum of $8\ \mathrm{GeV/c} < p_T^{\mathrm{J}/\Psi(1\mathrm{S})} < 30\ \mathrm{GeV/c}$ is:

$$\sigma_{tot} = (50.61 \pm 0.04_{stat} \pm 3.09_{sys} \pm 2.02_{lumi})\ nb$$

The first uncertainty is statistical, the second is systematic and the third one is related to the uncertainty on the luminosity (compare Section 4). The dominant uncertainty is related to the cross section measurement from the up and downward shifted trigger efficiency with 4.8 % in average. The systematic uncertainty from the momentum scale correction amounts to 3.6 % and the systematic uncertainty from the reconstruction efficiency is 1 % in average.

A summary of the measured cross sections in the different $p_T^{\mathrm{J}/\Psi(1\mathrm{S})}$ and $y^{\mathrm{J}/\Psi(1\mathrm{S})}$ ranges can be found in Table 5.2, where the different systematics are written separately.

The published results by the CMS Collaboration for an integrated luminosity of 312 nb^{-1} in the same rapidity and transverse momentum region for an unpolarized production scenario was measured with [36]:

$$\sigma_{tot} = (46.31 \pm 0.81_{stat} \pm 2.39_{sys} \pm 1.85_{lumi})\ nb.$$

The result lies within an 1.2 σ range to the measured inclusive production cross section of this analysis. The differential cross section are compared in Fig. 5.3. In the CMS measurements obtained with an integrated luminosity of 312 nb^{-1} the cross sections were additional measured for four extreme polarization scenarios: fully transversal and longitudinal polarized with respect to the Collins-Soper and the Helicity reference frame (see Section 2.2.1). The cross section values vary by 20 % in comparison to the unpolarized scenario. The same was performed for an integrated luminosity of 3 pb^{-1} for the Υ(1S) cross sections with the same conclusions[36, 37].

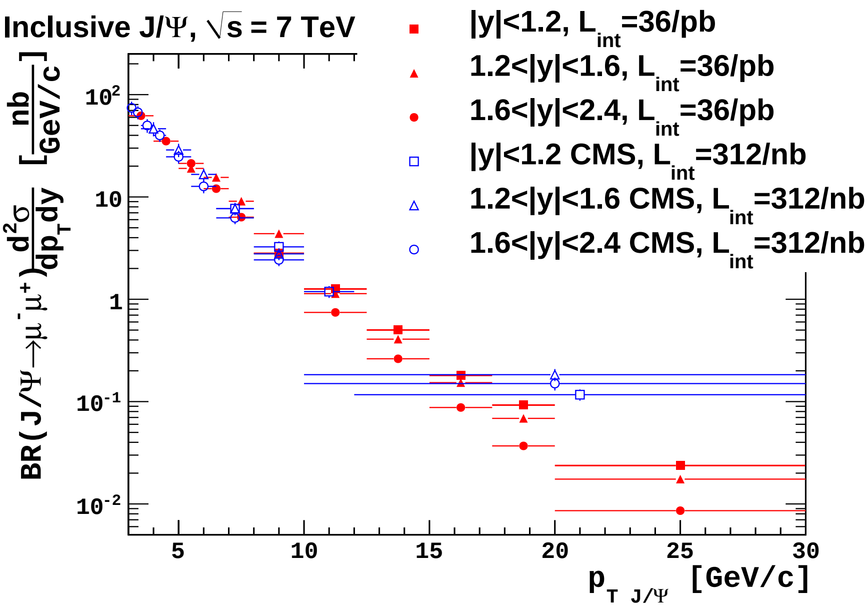

Figure 5.3: *Differential cross section for the* J/Ψ(1S) *meson as a function of* $p_T^{J/\Psi(1S)}$ *for all rapidity regions in comparison to the published CMS results (312* nb^{-1} *)[36].*

The measured inclusive production cross section is compared to theoretical predictions, which were performed within next to leading order non-relativistic quantumchromodynamics (NLO NRQCD) with color-octed contributions [38]. The theoretical calculations were performed only for the inclusive J/Ψ(1S) direct production, whereby the measured cross section contains also nonprompt contributions and indirect prompt production. The resulting error is small against the theoretical uncertainties, nevertheless for $p_T^{J/\Psi(1S)} < 5$ GeV/c the theoretical predictions fail to describe the data.

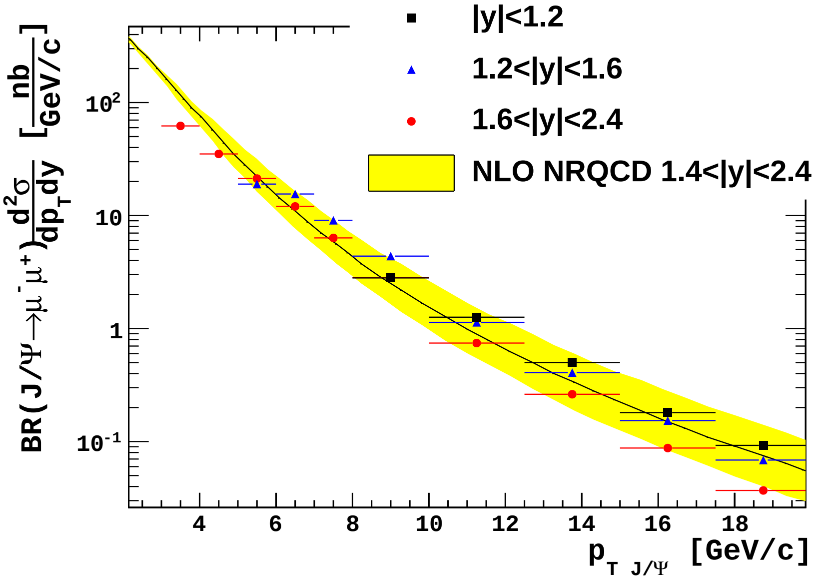

Figure 5.4: *Differential inclusive production cross section for the* J/Ψ(1S) *meson as a function of* p_T *in comparison to NLO NRQCD predictions [38].*

$\lvert y^{J/\Psi(1S)}\rvert < 1.2$				
$p_T^{J/\Psi(1S)}$ [GeV/c]	Xsec $\pm\ \sigma_{stat}$	$\sigma_{\text{reco eff}}$	$\sigma_{\text{trig eff}}$	$\sigma_{\text{pt corr}}$
8.0-10.0	2.805 ± 0.005	$^{+0.004}_{-0.045}$	$^{+0.154}_{-0.176}$	± 0.113
10.0-12.5	1.261 ± 0.003	$^{+0.006}_{-0.030}$	$^{+0.024}_{-0.059}$	± 0.032
12.5-15.0	0.501 ± 0.002	$^{+0.000}_{-0.008}$	$^{+0.012}_{-0.021}$	± 0.014
15.0-17.5	0.180 ± 0.001	$^{+0.000}_{-0.001}$	$^{+0.006}_{-0.006}$	± 0.007
17.5-20.0	0.092 ± 0.001	$^{+0.001}_{-0.001}$	$^{+0.003}_{-0.003}$	± 0.003
20.0-30.0	0.024 ± 0.000	$^{+0.000}_{-0.000}$	$^{+0.001}_{-0.001}$	± 0.001
$1.2 < \lvert y^{J/\Psi(1S)}\rvert < 1.6$				
$p_T^{J/\Psi(1S)}$ [GeV/c]	Xsec $\pm\ \sigma_{stat}$	$\sigma_{\text{reco eff}}$	$\sigma_{\text{trig eff}}$	$\sigma_{\text{pt corr}}$
5.0-6.0	19.002 ± 0.050	$^{+0.372}_{-0.609}$	$^{+1.535}_{-1.563}$	± 0.847
6.0-7.0	15.524 ± 0.035	$^{+0.632}_{-0.068}$	$^{+1.743}_{-0.868}$	± 1.221
7.0-8.0	9.082 ± 0.022	$^{+0.186}_{-0.157}$	$^{+0.569}_{-0.505}$	± 0.359
8.0-10.0	4.377 ± 0.010	$^{+0.053}_{-0.054}$	$^{+0.271}_{-0.246}$	± 0.172
10.0-12.5	1.135 ± 0.004	$^{+0.010}_{-0.010}$	$^{+0.039}_{-0.037}$	± 0.045
12.5-15.0	0.408 ± 0.003	$^{+0.003}_{-0.003}$	$^{+0.014}_{-0.013}$	± 0.016
15.0-17.5	0.153 ± 0.002	$^{+0.001}_{-0.001}$	$^{+0.005}_{-0.005}$	± 0.005
17.5-20.0	0.069 ± 0.001	$^{+0.001}_{-0.000}$	$^{+0.002}_{-0.002}$	± 0.003
20.0-30.0	0.0175 ± 0.000	$^{+0.000}_{-0.000}$	$^{+0.001}_{-0.001}$	± 0.001
$1.6 < \lvert y^{J/\Psi(1S)}\rvert < 2.4$				
$p_T^{J/\Psi(1S)}$ [GeV/c]	Xsec $\pm\ \sigma_{stat}$	$\sigma_{\text{reco eff}}$	$\sigma_{\text{trig eff}}$	$\sigma_{\text{pt corr}}$
3.0-4.0	62.142 ± 0.116	$^{+0.497}_{-3.377}$	$^{+19.847}_{-12.962}$	± 1.566
4.0-5.0	35.110 ± 0.046	$^{+0.776}_{-0.913}$	$^{+3.007}_{-2.743}$	± 1.428
5.0-6.0	21.266 ± 0.041	$^{+0.034}_{-0.836}$	$^{+1.397}_{-2.021}$	± 0.572
6.0-7.0	12.050 ± 0.023	$^{+0.094}_{-0.280}$	$^{+0.962}_{-1.001}$	± 0.411
7.0-8.0	6.343 ± 0.014	$^{+0.070}_{-0.109}$	$^{+0.372}_{-0.375}$	± 0.231
8.0-10.0	2.824 ± 0.007	$^{+0.031}_{-0.031}$	$^{+0.177}_{-0.157}$	± 0.108
10.0-12.5	0.744 ± 0.003	$^{+0.010}_{-0.009}$	$^{+0.026}_{-0.024}$	± 0.027
12.5-15.0	0.262 ± 0.002	$^{+0.003}_{-0.003}$	$^{+0.009}_{-0.008}$	± 0.010
15.0-17.5	0.088 ± 0.001	$^{+0.001}_{-0.003}$	$^{+0.001}_{-0.005}$	± 0.002
17.5-20.0	0.037 ± 0.001	$^{+0.000}_{-0.000}$	$^{+0.001}_{-0.001}$	± 0.001
20.0-30.0	0.009 ± 0.000	$^{+0.000}_{-0.000}$	$^{+0.000}_{-0.001}$	± 0.000

Table 5.2: *Differential cross section for the* J/Ψ(1S) *meson for different* $p_T^{J/\Psi(1S)}$ *and* $y^{J/\Psi(1S)}$ *regions with the statistical and systematical uncertainties.*

5.2 Inclusive differential and total $\Upsilon(1S)$ Cross Section

The number of Υ(nS) events for the resulting production cross section are obtained using the fit to the weighted dimuon invariant mass spectrum described in Section 4.1.2, where all fits used to obtain the Υ(nS) cross sections can be found in Appendix G. The measured yields for the three Υ(nS) resonances are summarized in Table 5.3 with their statistical uncertainty.

$p_T^{\Upsilon(1S)}$ [GeV/c]	$\Upsilon(1S)$	$\Upsilon(2S)$	$\Upsilon(3S)$
3.0-4.0	26288 $\pm$ 336	8713 $\pm$ 257	4050 $\pm$ 307
4.0-5.0	25702 $\pm$ 627	5709 $\pm$ 260	3100 $\pm$ 234
5.0-6.0	25011 $\pm$ 498	6784 $\pm$ 221	3567 $\pm$ 195
6.0-7.0	19766 $\pm$ 268	5748 $\pm$ 191	3056 $\pm$ 187
7.0-8.0	21966 $\pm$ 1833	4229 $\pm$ 209	2822 $\pm$ 263
8.0-10.0	27381 $\pm$ 316	7223 $\pm$ 212	4264 $\pm$ 213
10.0-12.5	17560 $\pm$ 336	4605 $\pm$ 157	3137 $\pm$ 146
12.5-15.0	8940 $\pm$ 258	2523 $\pm$ 110	2022 $\pm$ 77
15.0-17.5	3747 $\pm$ 98	1421. $\pm$ 60	975 $\pm$ 49
17.5-20.0	2400 $\pm$ 211	821 $\pm$ 83	608 $\pm$ 77
20.0-30.0	1628 $\pm$ 59	786 $\pm$ 43	596 $\pm$ 42

Table 5.3: *Measured weighted yield with the statistical uncertainty for the* $\Upsilon(1S)$, $\Upsilon(2S)$ *and* $\Upsilon(3S)$ *resonance.*

The differential cross sections for $\Upsilon(1S)$, $\Upsilon(2S)$ and $\Upsilon(3S)$ are shown in Fig. 5.5 and 5.6. The uncertainties are the statistical and systematical ones added in quadrature, where the luminosity errors are not included. The systematic uncertainties are obtained in the same way as for the $J/\Psi(1S)$ meson.

The total production cross section for $\Upsilon(1S)$ in a transverse momentum range of 3 GeV/c $< p_T^{\Upsilon(1S)} < 30$ GeV/c and in the rapidity region of $|y^{\Upsilon(1S)}| < 2.0$ is measured with:

$$\sigma_{tot} = (4.96 \pm 0.06_{stat} \pm 0.47_{sys} \pm 0.20_{lumi})\ nb$$

The first uncertainty is the statistical, the second the systematical and the third one the uncertainty on the luminosity measurements. The systematic uncertainty is dominated by the systematic uncertainty due to the trigger efficiency + 7 % and - 10 %. The systematic uncertainty from the momentum scale correction is 3.7 % and the systematic uncertainty due to

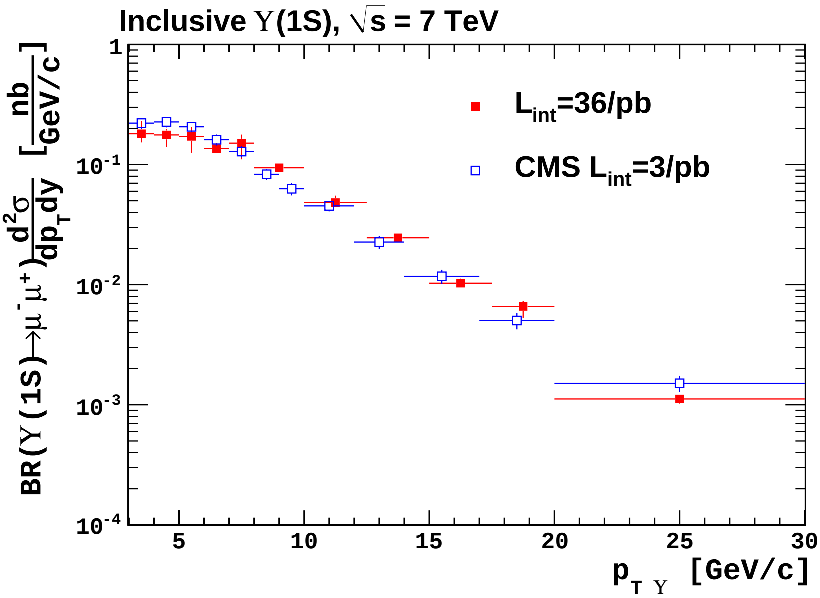

Figure 5.5: *Differential cross section for the Υ(1S) meson as a function of p_T for all rapidity regions in comparison to the CMS results obtained with 3 pb^{-1} [37].*

the reconstruction efficiency is in average less than 1 %. The obtained Υ(nS) cross section with their statistical and systematical uncertainties are listed in Table 5.4.

The measured total cross section in a rapidity range of $|y^{\Upsilon(1S)}| < 2.0$ and a transverse momentum range of 3 GeV/c $< p_T^{\Upsilon(1S)} <$ 30 GeV/c is compared to published CMS results performed with an integrated luminosity of 3 pb^{-1} for the unpolarized production scenario [37]:

$$\sigma_{tot} = (5.17 \pm 0.12_{stat} \pm 0.15_{sys} \pm 0.21_{lumi})\ nb$$

The results obtained in this analysis lie within an 1 σ range relative to the results obtained for 3 pb^{-1}. A comparison can also be seen in Fig. 5.5 and 5.6.

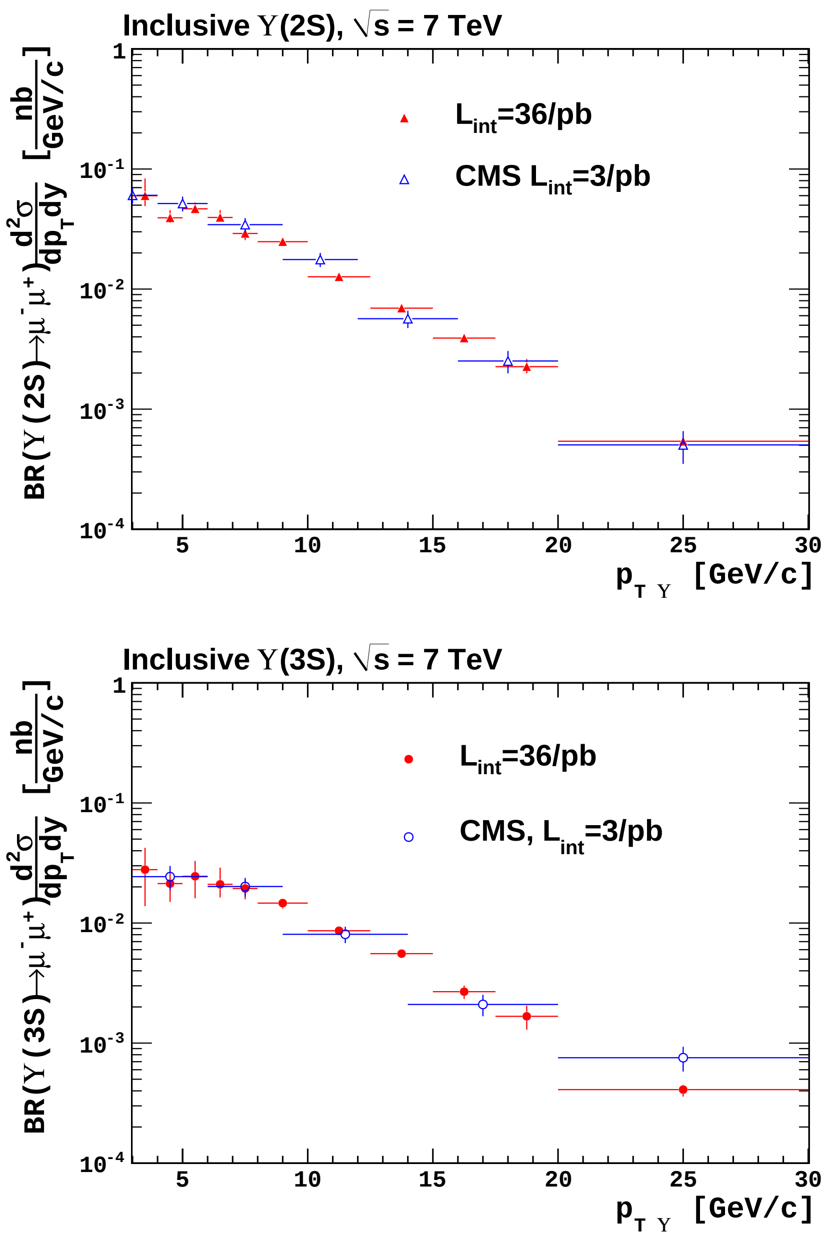

Figure 5.6: *Differential cross section for the* $\Upsilon(2S)$ *and* $\Upsilon(3S)$ *meson as a function of* p_T *for all rapidity regions in comparison to the CMS results obtained with* $3\,\mathrm{pb}^{-1}$ *[37].*

$p_T^{\Upsilon(nS)}$ [GeV/c]	$\Upsilon(1S)$ Xsec $\pm\ \sigma_{stat}$	$\sigma_{\text{reco eff}}$	$\sigma_{\text{trig eff}}$	$\sigma_{\text{pt corr}}$
3.0-4.0	0.1806 ± 0.0023	$^{+0.0045}_{-0.0204}$	$^{+0.0485}_{-0.0138}$	± 0.0123
4.0-5.0	0.177 ± 0.0043	$^{+0.0040}_{-0.0047}$	$^{+0.0030}_{-0.0289}$	± 0.0207
5.0-6.0	0.1719 ± 0.0034	$^{+0.0184}_{-0.0235}$	$^{+0.0085}_{-0.0290}$	± 0.0267
6.0-7.0	0.1358 ± 0.0018	$^{+0.0012}_{-0.0019}$	$^{+0.0150}_{-0.0099}$	± 0.0026
7.0-8.0	0.1509 ± 0.0126	$^{+0.0072}_{-0.0222}$	$^{+0.0164}_{-0.0270}$	± 0.0158
8.0-10.0	0.0941 ± 0.0011	$^{+0.0000}_{-0.0009}$	$^{+0.0054}_{-0.0057}$	± 0.0001
10.0-12.5	0.0483 ± 0.0009	$^{+0.0067}_{-0.0025}$	$^{+0.0015}_{-0.0017}$	± 0.0000
12.5-15.0	0.0246 ± 0.0007	$^{+0.0003}_{-0.0002}$	$^{+0.0011}_{-0.0005}$	± 0.0001
15.0-17.5	0.0103 ± 0.0003	$^{+0.0006}_{-0.0001}$	$^{+0.0004}_{-0.0002}$	± 0.0006
17.5-20.0	0.0066 ± 0.0006	$^{+0.0003}_{-0.0000}$	$^{+0.0000}_{-0.0011}$	± 0.0003
20.0-30.0	0.0011 ± 0.0000	$^{+0.0000}_{-0.0000}$	$^{+0.0000}_{-0.0000}$	± 0.0000

$p_T^{\Upsilon(nS)}$ [GeV/c]	$\Upsilon(2S)$ Xsec $\pm\ \sigma_{stat}$	$\sigma_{\text{reco eff}}$	$\sigma_{\text{trig eff}}$	$\sigma_{\text{pt corr}}$
3.0-4.0	0.0599 ± 0.0016	$^{+0.0050}_{-0.0027}$	$^{+0.0229}_{-0.0101}$	± 0.0023
4.0-5.0	0.0392 ± 0.0018	$^{+0.0015}_{-0.0027}$	$^{+0.0057}_{-0.0008}$	± 0.0013
5.0-6.0	0.0466 ± 0.0015	$^{+0.0037}_{-0.0012}$	$^{+0.0043}_{-0.0000}$	± 0.0011
6.0-7.0	0.0395 ± 0.0013	$^{+0.0011}_{-0.0014}$	$^{+0.0057}_{-0.0025}$	± 0.0002
7.0-8.0	0.0291 ± 0.0014	$^{+0.0000}_{-0.0026}$	$^{+0.0017}_{-0.0014}$	± 0.0012
8.0-10.0	0.0248 ± 0.0007	$^{+0.0001}_{-0.0000}$	$^{+0.0013}_{-0.0016}$	± 0.0002
10.0-12.5	0.0127 ± 0.0004	$^{+0.0005}_{-0.0005}$	$^{+0.0004}_{-0.0004}$	± 0.0001
12.5-15.0	0.0069 ± 0.0003	$^{+0.0000}_{-0.0000}$	$^{+0.0002}_{-0.0004}$	± 0.0001
15.0-17.5	0.0039 ± 0.0002	$^{+0.0001}_{-0.0000}$	$^{+0.0000}_{-0.0002}$	± 0.0002
17.5-20.0	0.0023 ± 0.0002	$^{+0.0000}_{-0.0000}$	$^{+0.0002}_{-0.0000}$	± 0.0001
20.0-30.0	0.0005 ± 0.0000	$^{+0.0000}_{-0.0000}$	$^{+0.0000}_{-0.0000}$	± 0.0000

$p_T^{\Upsilon(nS)}$ [GeV/c]	$\Upsilon(3S)$ Xsec $\pm\ \sigma_{stat}$	$\sigma_{\text{reco eff}}$	$\sigma_{\text{trig eff}}$	$\sigma_{\text{pt corr}}$
3.0-4.0	0.0278 ± 0.0021	$^{+0.0038}_{-0.0010}$	$^{+0.0134}_{-0.0134}$	± 0.0035
4.0-5.0	0.0213 ± 0.0016	$^{+0.0027}_{-0.0015}$	$^{+0.0019}_{-0.0045}$	± 0.0039
5.0-6.0	0.0245 ± 0.0013	$^{+0.0030}_{-0.0048}$	$^{+0.0060}_{-0.0047}$	± 0.0048
6.0-7.0	0.0210 ± 0.0013	$^{+0.0025}_{-0.0033}$	$^{+0.0068}_{-0.0006}$	± 0.0030
7.0-8.0	0.01939 ± 0.0018	$^{+0.0000}_{-0.0008}$	$^{+0.0011}_{-0.0004}$	± 0.0030
8.0-10.0	0.0147 ± 0.0007	$^{+0.0002}_{-0.0006}$	$^{+0.0006}_{-0.0010}$	± 0.0003
10.0-12.5	0.0086 ± 0.0004	$^{+0.0005}_{-0.0004}$	$^{+0.0003}_{-0.0003}$	± 0.0001
12.5-15.0	0.0056 ± 0.0002	$^{+0.0000}_{-0.0000}$	$^{+0.0001}_{-0.0000}$	± 0.0000
15.0-17.5	0.0027 ± 0.0001	$^{+0.0000}_{-0.0003}$	$^{+0.0002}_{-0.0000}$	± 0.0020
17.5-20.0	0.0017 ± 0.0002	$^{+0.0002}_{-0.0002}$	$^{+0.0002}_{-0.0002}$	± 0.0000
20.0-30.0	0.0004 ± 0.00	$^{+0.0000}_{-0.0000}$	$^{+0.0000}_{-0.0000}$	± 0.0000

Table 5.4: *Differential cross section for the $\Upsilon(nS)$ mesons for different $p_T^{\Upsilon(nS)}$ regions and $y^{\Upsilon(nS)}$<2.0 with the statistical and systematical uncertainties.*

The prompt production cross section results for the $\Upsilon(1S)$ resonance in comparison to theoretical predictions from NLO NRQCD calculation, where $\Upsilon(2S,3S)$ and $X_b^{1P,2P}$ feed-down contributions are all considered [39], are shown in Fig. 5.7. The uncertainties of the theoretical curves are due to the fits of the matrix elements and the uncertainties of scale dependence in the calculation. The theoretical predictions are in good agreement with the measured $\Upsilon(1S)$ cross section results.

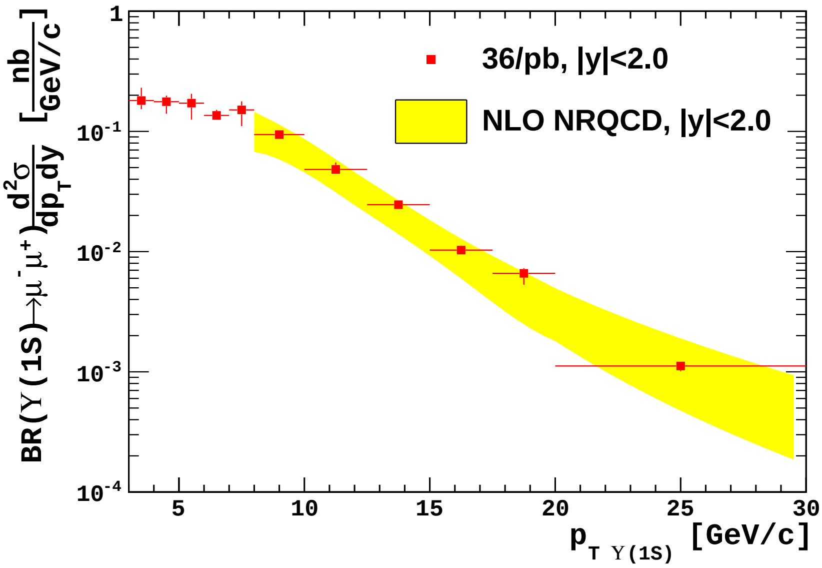

Figure 5.7: *Differential production cross section for the* $\Upsilon(1S)$ *meson as a function of* p_T *in comparison to NLO NRQCD predictions [39].*

CHAPTER 6

Conclusions

In this diploma thesis the inclusive production cross section of $J/\Psi(1S)$ and $\Upsilon(1S,2S,3S)$ with 36 pb^{-1} , measured with the CMS detector at LHC, is presented. The cross section is obtained by weighting the obtained number of $J/\Psi(1S)$ and $\Upsilon(1S,2S,3S)$ events by the kinematical acceptance of the CMS detector and the efficiencies related to instrumental effects. The acceptance is determined using an unpolarized MC sample and the efficiencies are all obtained via the data driven tag and probe method.

The differential cross sections for inclusive $J/\Psi(1S)$ and $\Upsilon(1S,2S,3S)$ production are presented in dependence of the transverse momentum of $J/\Psi(1S)$ and $\Upsilon(1S,2S,3S)$, respectively.

The total inclusive production cross section of $J/\Psi(1S)$ for 8 GeV/c $<p_T<$30 GeV/c and $|y| < 2.4$ is measured with $\sigma_{tot} = (50.61 \pm 0.04_{stat} \pm 3.09_{sys} \pm 2.02_{lumi})\ nb$. For $\Upsilon(1S)$ the measured total production cross section for 3 GeV/c $<p_T<$30 GeV/c and $|y| < 2.0$ is given by $(4.96 \pm 0.06_{stat} \pm 0.47_{sys} \pm 0.20_{lumi})\ nb$. The systematic uncertainty is dominated by the uncertainty due to the trigger efficiency.

The results are compared to former CMS results obtained with less integrated luminosity and agree within an 1.2 σ range for the measured $J/\Psi(1S)$ and an 1 σ range for the measured $\Upsilon(1S)$ total production cross section. Additionally the differential cross sections for $J/\Psi(1S)$ and $\Upsilon(1S)$ are compared to recent theoretical predictions from NLO NRQCD calculations. The theoretical predictions describe the data for p_T regions from 5 GeV/c on for the $J/\Psi(1S)$ results and from 8 GeV/c on for the $\Upsilon(1S)$ results.

Appendix

A Momentum Scale Corrections

The momentum scale correction of the muons is dependent in P_T, η , and φ and possess a charge-dependence. The correction is obtained by the following functions, whereby the used parameters can be found in table A.1 and A.2 [33].

charge$_\mu > 0$ **and** $\varphi > 0$ **:**

$$P_{T\mu}^{\mathrm{corr}} = (\mathrm{par}[0] + \mathrm{par}[9] \cdot \mathrm{EtaCorrection}(\eta_\mu) + \mathrm{par}[1] \cdot |\varphi| \cdot \sin(2 \cdot \varphi + \mathrm{par}[2])) \cdot P_{T\mu} \tag{A.1}$$

charge$_\mu > 0$ **and** $\varphi < 0$ **:**

$$P_{T\mu}^{\mathrm{corr}} = (\mathrm{par}[0] + \mathrm{par}[9] \cdot \mathrm{EtaCorrection}(\eta_\mu) + \mathrm{par}[3] \cdot |\varphi| \cdot \sin(2 \cdot \varphi + \mathrm{par}[4])) \cdot P_{T\mu} \tag{A.2}$$

charge$_\mu < 0$ **and** $\varphi > 0$ **:**

$$P_{T\mu}^{\mathrm{corr}} = (\mathrm{par}[0] + \mathrm{par}[9] \cdot \mathrm{EtaCorrection}(\eta_\mu) - \mathrm{par}[5] \cdot |\varphi| \cdot \sin(2 \cdot \varphi + \mathrm{par}[6])) \cdot P_{T\mu} \tag{A.3}$$

charge$_\mu < 0$ **and** $\varphi < 0$ **:**

$$P_{T\mu}^{\mathrm{corr}} = (\mathrm{par}[0] + \mathrm{par}[9] \cdot \mathrm{EtaCorrection}(\eta_\mu) - \mathrm{par}[7] \cdot |\varphi| \cdot \sin(2 \cdot \varphi + \mathrm{par}[8])) \cdot P_{T\mu} \tag{A.4}$$

par[0]	1.00094
par[1]	-0.000223852
par[2]	0.919236
par[3]	-0.000565047
par[4]	-0.296159
par[5]	-0.000220599
par[6]	2.27315
par[7]	-0.000759843
par[8]	-0.0191391
par[9]	0.490358

Table A.1: *Correction parameters used in the Momentum scale correction formula [33].*

$\lvert\eta_\mu\rvert$	EtaCorrection(η_μ)
$\lvert\eta_\mu\rvert < 0.2$	-0.00063509
$\lvert\eta_\mu\rvert < 0.4$	-0.000585369
$\lvert\eta_\mu\rvert < 0.6$	-0.00077363
$\lvert\eta_\mu\rvert < 0.8$	-0.000547868
$\lvert\eta_\mu\rvert < 1.0$	-0.000954819
$\lvert\eta_\mu\rvert < 1.2$	-0.000162139
$\lvert\eta_\mu\rvert < 1.4$	0.0026909
$\lvert\eta_\mu\rvert < 1.6$	0.000684376
$\lvert\eta_\mu\rvert < 1.8$	-0.00174534
$\lvert\eta_\mu\rvert < 2.0$	-0.00177076
$\lvert\eta_\mu\rvert < 2.2$	0.00117463
$\lvert\eta_\mu\rvert < 2.4$	0.000985705
$\lvert\eta_\mu\rvert < 2.6$	0.00163941

Table A.2: *Eta Correction parameters used in the Momentum scale correction formula [33].*

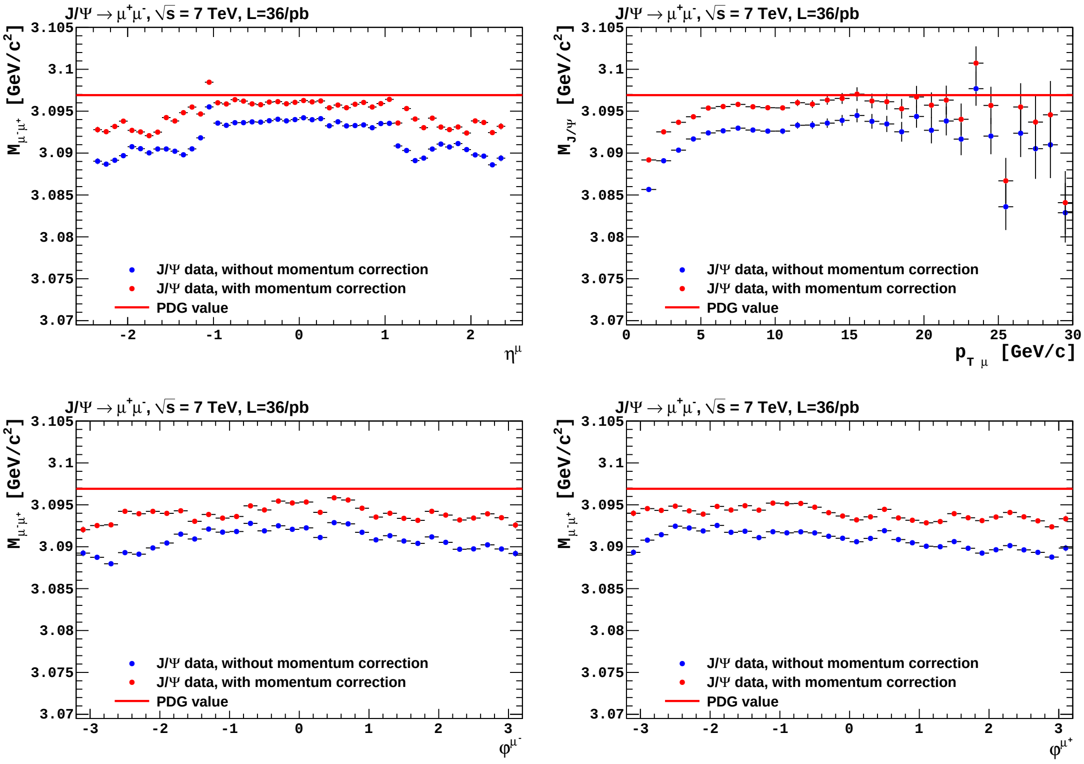

Figure A.1: *Momentum scale corrections using the* J/Ψ(1S) *resonance in dependence of* η, P_T *and* φ *of the muons.* φ *is plotted seperatly for the negative and the positive muons. The red line refers to the world average value [9] of the* J/Ψ(1S) *mass. The blue dots are the uncorrected and the red ones are the corrected data values.*

B Acceptance

p_T bin [GeV/c]	$\mathscr{A}(p_T)$
0.0-0.5	0.017
0.5-1.0	0.030
1.0-1.5	0.045
1.5-2.0	0.048
2.0-2.5	0.050
2.5-3.0	0.053
3.0-3.5	0.060
3.5-4.0	0.069
4.0-4.5	0.086
4.5-5.0	0.107
5.0-5.5	0.131
5.5-6.0	0.156
6.0-7.0	0.195
7.0-8.0	0.265
8.0-9.0	0.337
9.0-10.0	0.386
10.0-11.0	0.429
11.0-12.0	0.473
12.0-13.0	0.510
13.0-14.0	0.525
14.0-15.0	0.567
15.0-17.0	0.593
17.0-20.0	0.640
20.0-25.0	0.698
25.0-30.0	0.753

Table B.3: *Unpolarized acceptance in p_T bins for* $\mathrm{J}/\Psi(1\mathrm{S})$ *, integrated over $|y|$, where* $\mathrm{J}/\Psi(1\mathrm{S})$ *results are given for $|y| < 2.4$.*

p_T bin [GeV/c]	$\mathscr{A}(p_T)$
0 - 1	0.490
1 - 2	0.457
2 - 3	0.394
3 - 4	0.325
4 - 5	0.302
5 - 6	0.298
6 - 7	0.302
7 - 8	0.315
8 - 9	0.336
9 - 10	0.358
10 - 11	0.382
11 - 12	0.403
12 - 13	0.424
13 - 14	0.445
14 - 15	0.460
15 - 16	0.483
16 - 17	0.500
17 - 18	0.515
18 - 19	0.528
19 - 20	0.541
20 - 21	0.554
21 - 22	0.569
22 - 23	0.578
23 - 24	0.589
24 - 25	0.596
25 - 26	0.606
26 - 27	0.615
27 - 28	0.618
28 - 29	0.625
29 - 30	0.626

Table B.4: *Unpolarized acceptance in p_T bins for $\Upsilon(1S)$, integrated over $|y|$, where $\Upsilon(1S)$ results are given for $|y| < 2.4$.*

C Reconstruction Efficiency

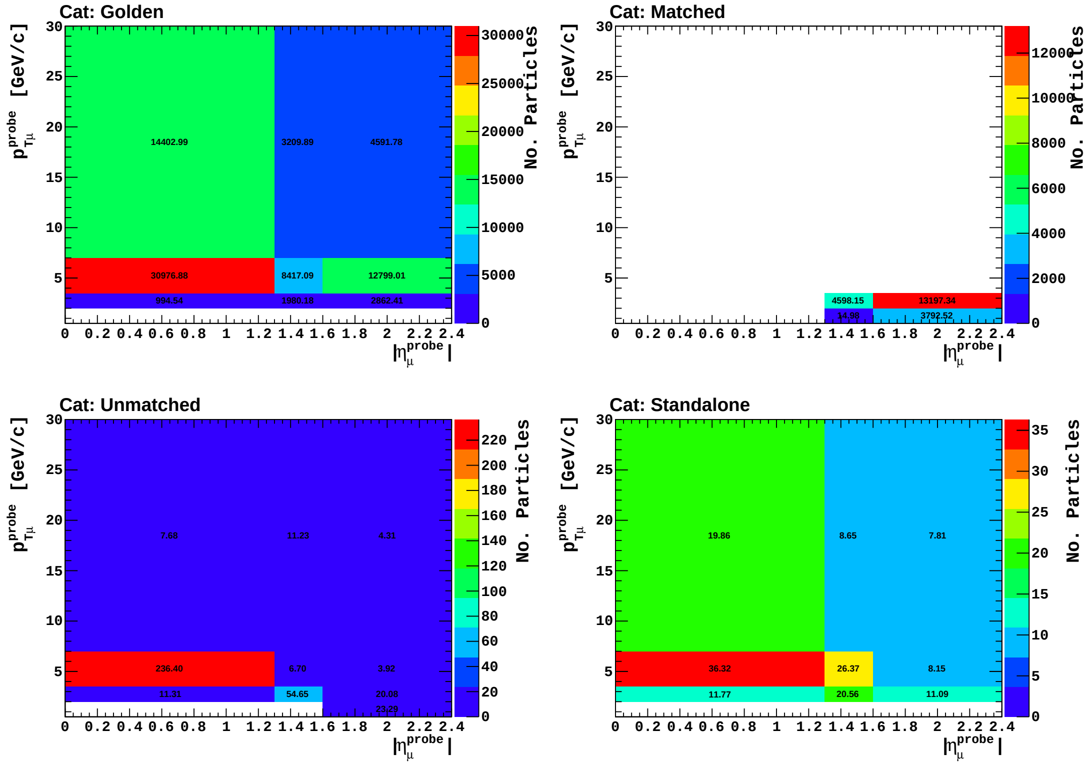

Figure C.2: *Number of* J/Ψ(1S) *events in the different categories used to obtain the tracking efficiency via tag and probe in data.*

p_T^μ [GeV/c]	$\lvert\eta^\mu\rvert < 1.3$	$1.3 < \lvert\eta^\mu\rvert < 1.6$	$1.6 < \lvert\eta^\mu\rvert < 2.4$
0.5-2.0	-	100 ± 0.0	100 ± 0.0
2.0-3.5	99.41 ± 0.17	99.76 ± 0.05	99.94 ± 0.02
3.5-7.0	99.94 ± 0.01	99.84 ± 0.03	99.97 ± 0.01
7.0-30.0	99.93 ± 0.02	99.87 ± 0.05	99.92 ± 0.3

Table C.5: *Tracking efficiency in % using the* J/Ψ(1S) *resonance determined by the tag and probe method with 36* pb^{-1} *of CMS data.*

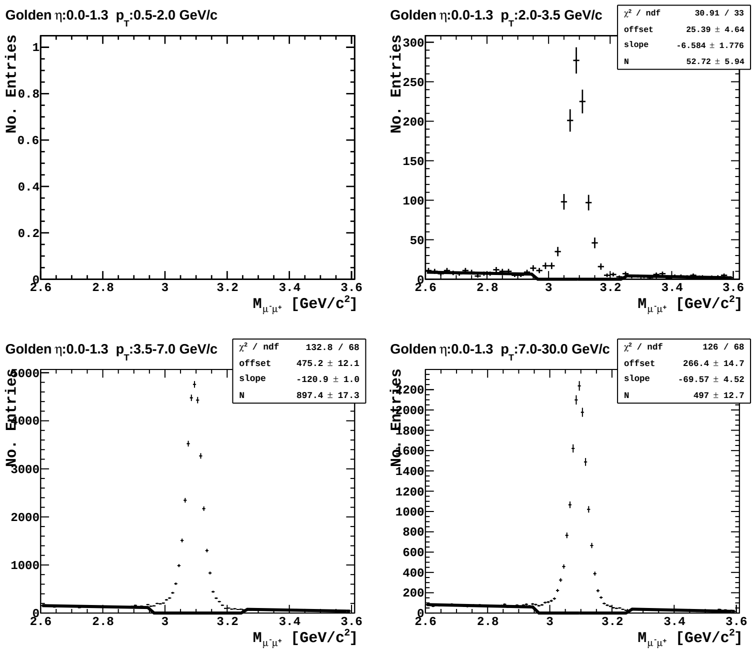

Figure C.3: *Fits used to obtain the tracking efficiency via tag and probe in data.*

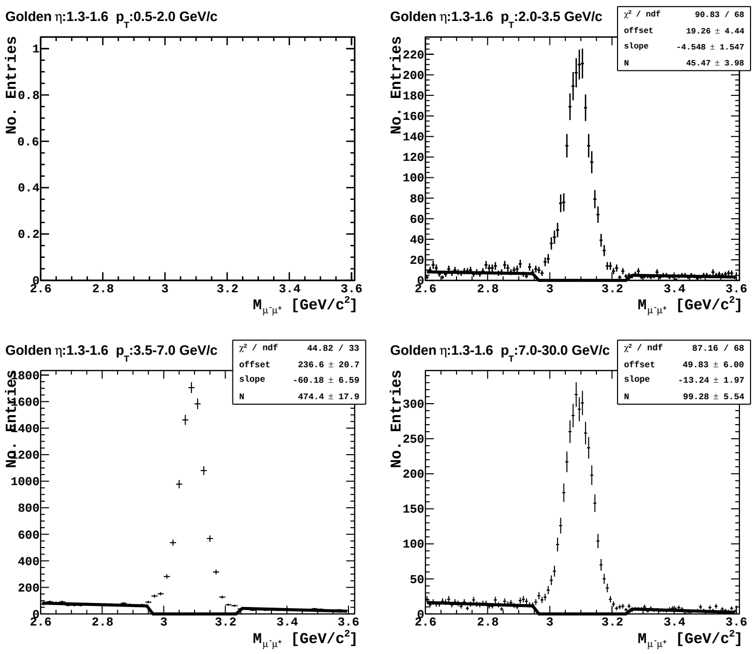

Figure C.4: *Fits used to obtain the tracking efficiency via tag and probe in data.*

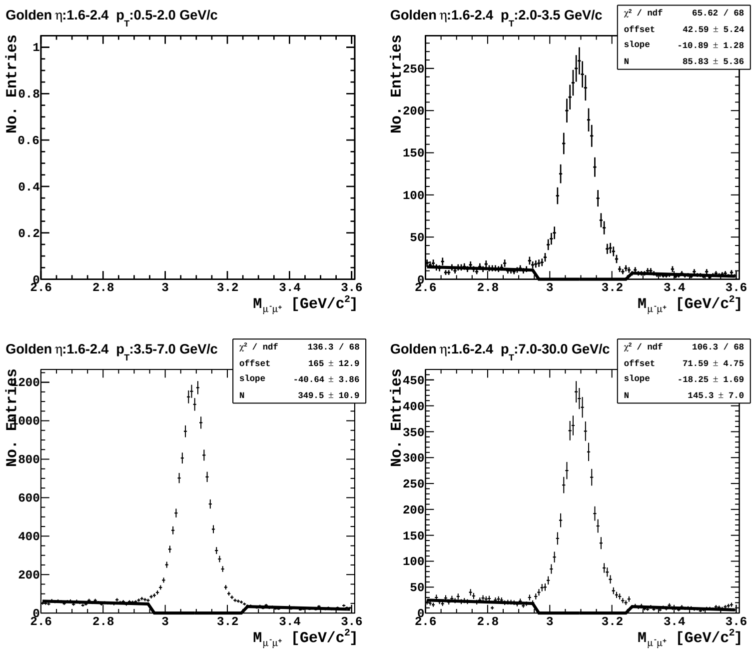

Figure C.5: *Fits used to obtain the tracking efficiency via tag and probe in data.*

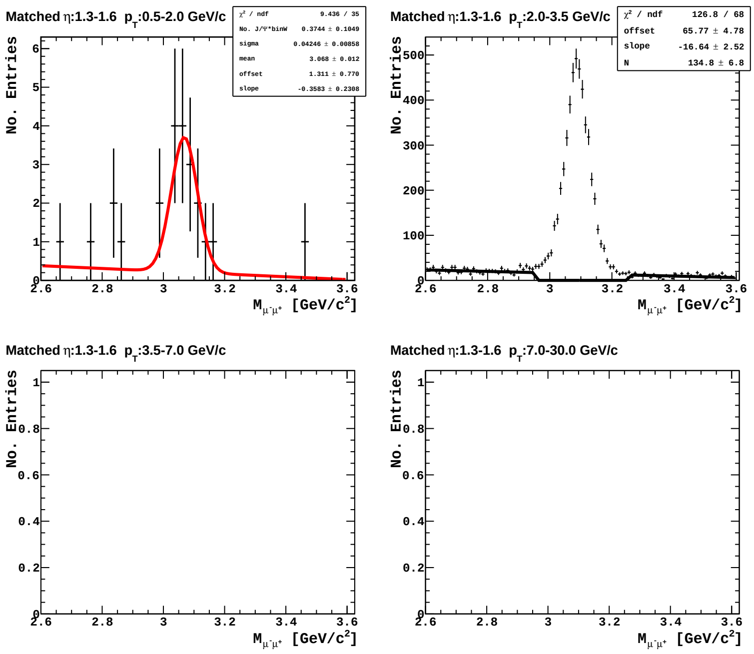

Figure C.6: *Fits used to obtain the tracking efficiency via tag and probe in data.*

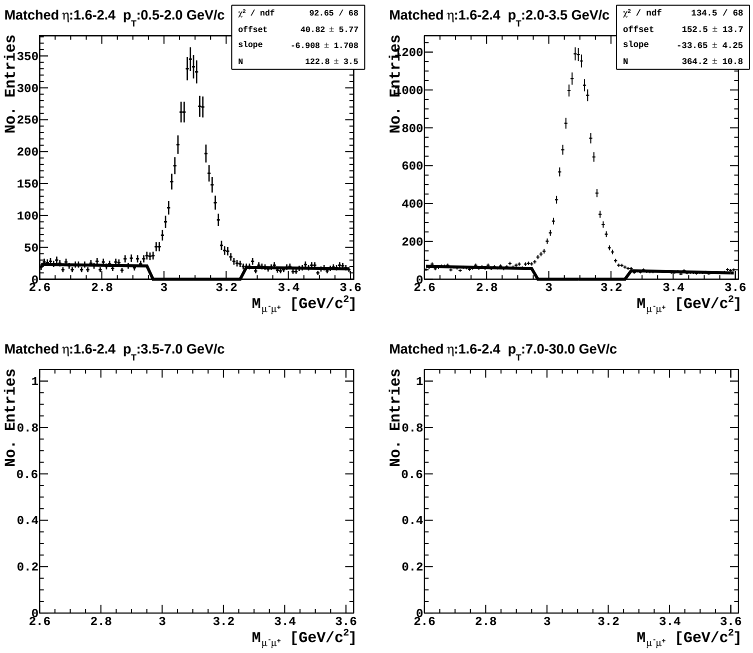

Figure C.7: *Fits used to obtain the tracking efficiency via tag and probe in data.*

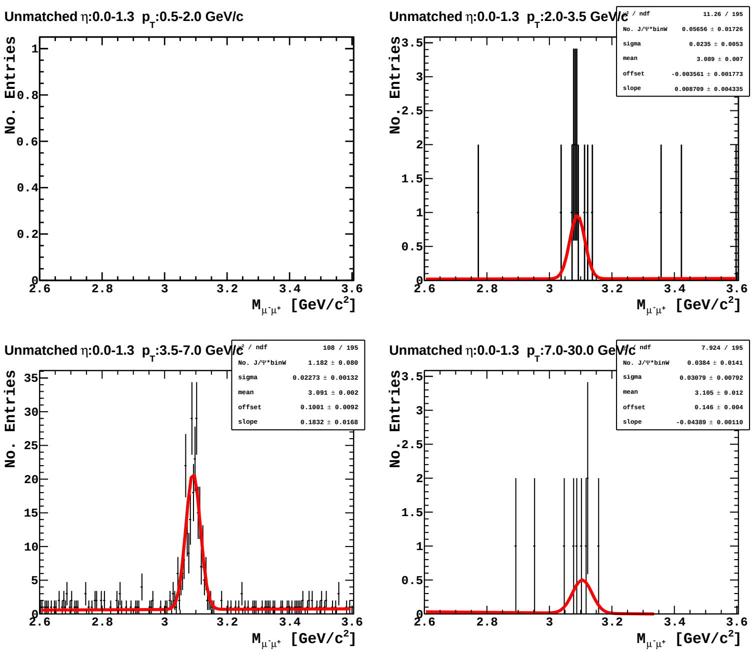

Figure C.8: *Fits used to obtain the tracking efficiency via tag and probe in data.*

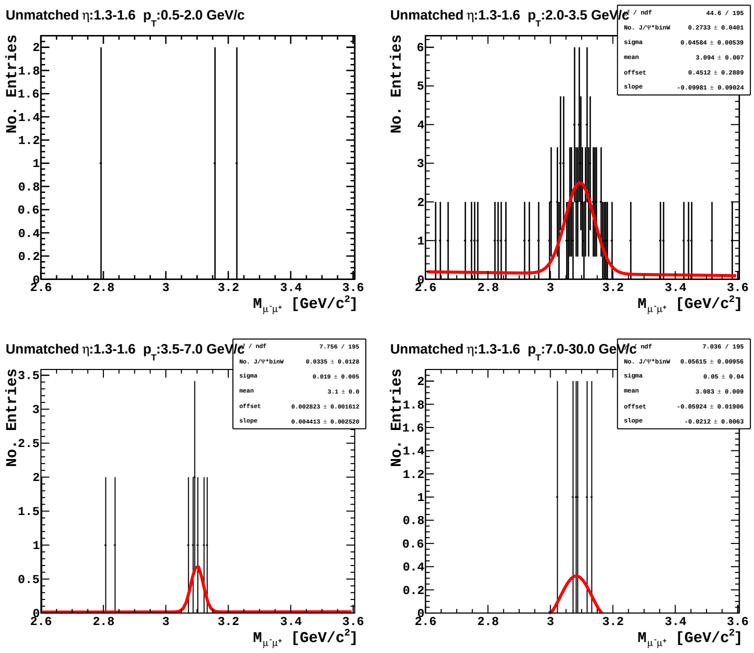

Figure C.9: *Fits used to obtain the tracking efficiency via tag and probe in data.*

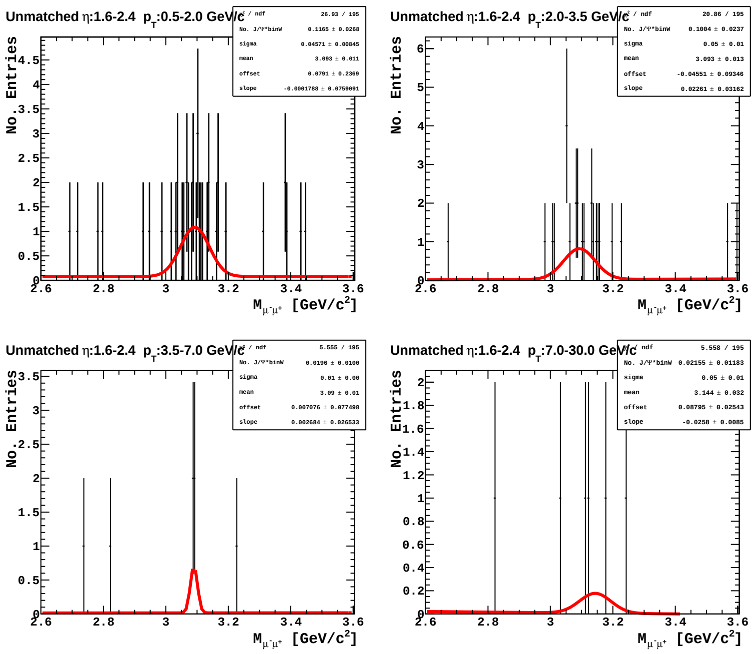

Figure C.10: *Fits used to obtain the tracking efficiency via tag and probe in data.*

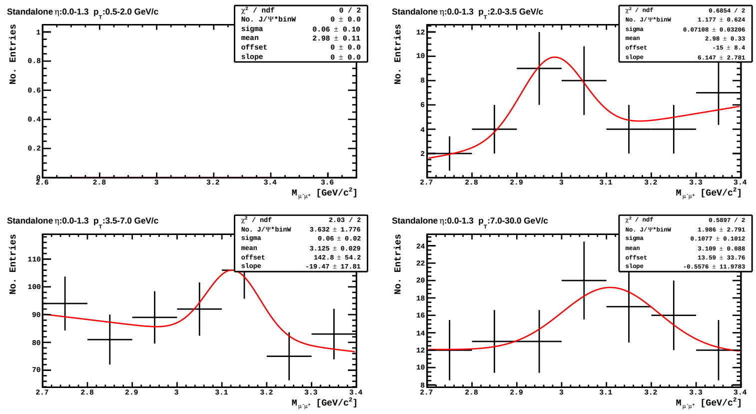

Figure C.11: *Fits used to obtain the tracking efficiency via tag and probe in data.*

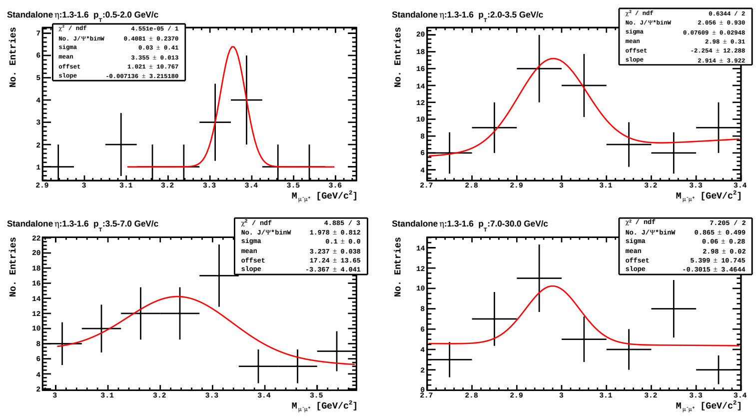

Figure C.12: *Fits used to obtain the tracking efficiency via tag and probe in data.*

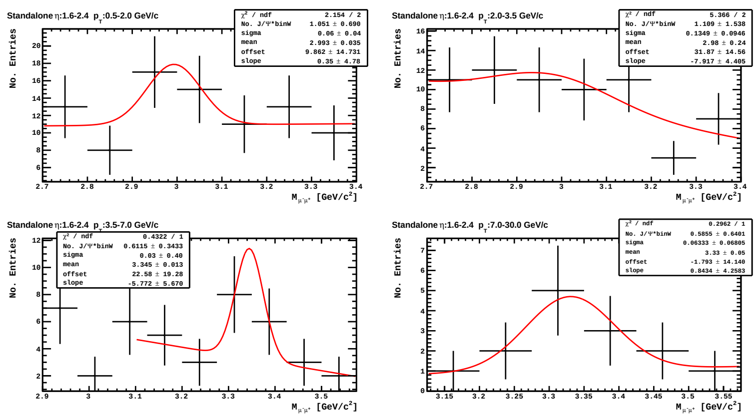

Figure C.13: *Fits used to obtain the tracking efficiency via tag and probe in data.*

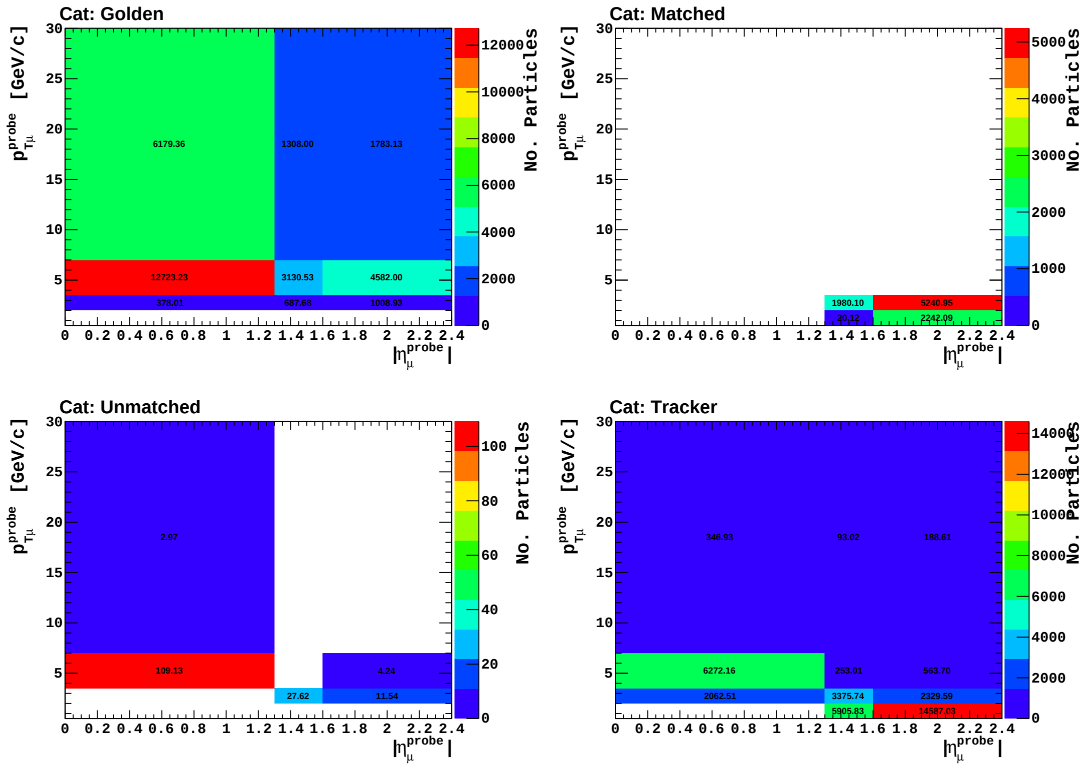

Figure C.14: *Number of* J/Ψ(1S) *events in the different categories used to obtain the standalone and matching efficiency via tag and probe in data.*

p_T^{μ} [GeV/c]	$\lvert\eta^{\mu}\rvert < 1.3$	$1.3 < \lvert\eta^{\mu}\rvert < 1.6$	$1.6 < \lvert\eta^{\mu}\rvert < 2.4$
0.5-2.0	-	0.34 ± 0.08	13.32 ± 0.26
2.0-3.5	26.82 ± 0.83	50.05 ± 0.61	75.73 ± 0.44
3.5-7.0	80.29 ± 0.22	96.12 ± 0.24	94.21 ± 0.24
7.0-30.0	97.27 ± 0.14	96.57 ± 0.35	94.98 ± 0.36

Table C.6: *Standalone efficiency in % using the* J/Ψ(1S) *resonance determined by the tag and probe method with 36* pb^{-1} *of CMS data.*

p_T^{μ} [GeV/c]	$\lvert\eta^{\mu}\rvert < 1.3$	$1.3<\lvert\eta^{\mu}\rvert < 1.6$	$1.6 < \lvert\eta^{\mu}\rvert < 2.4$
0.5-2.0	-	100	100
2.0-3.5	100	99.18 ± 0.15	99.84 ± 0.05
3.5-7.0	99.57 ± 0.04	100.0 ± 0.0	99.95 ± 0.02
7.0-30.0	99.98 ± 0.01	100.0 ± 0.0	99.92 ± 0.3

Table C.7: *Matching efficiency in % using the* $\mathrm{J}/\Psi(1\mathrm{S})$ *resonance determined by the tag and probe method with 36* pb^{-1} *of CMS data.*

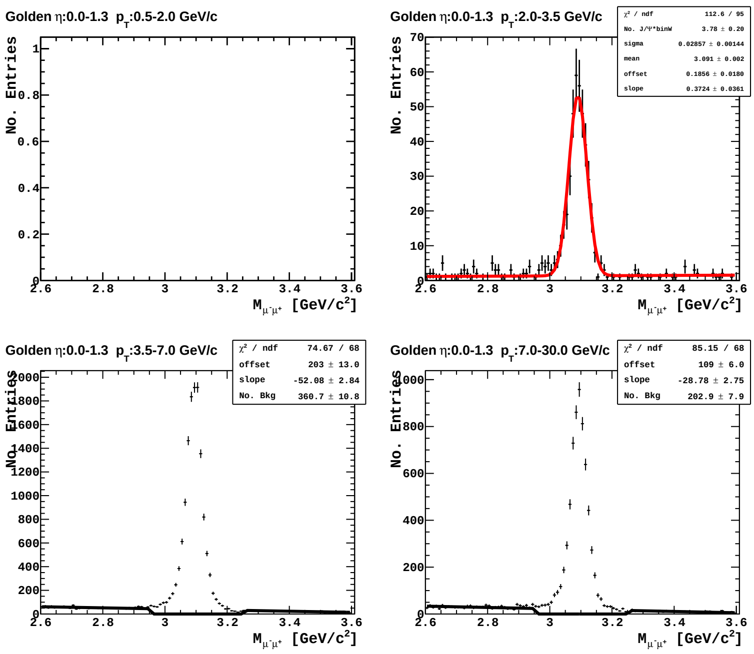

Figure C.15: *Fits used to obtain the standalone and matching efficiency via tag and probe in data.*

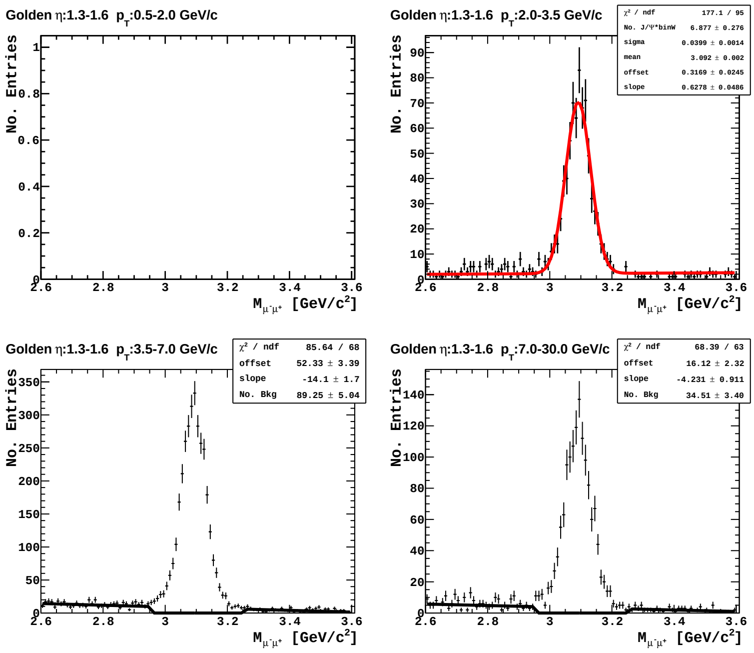

Figure C.16: *Fits used to obtain the standalone and matching efficiency via tag and probe in data.*

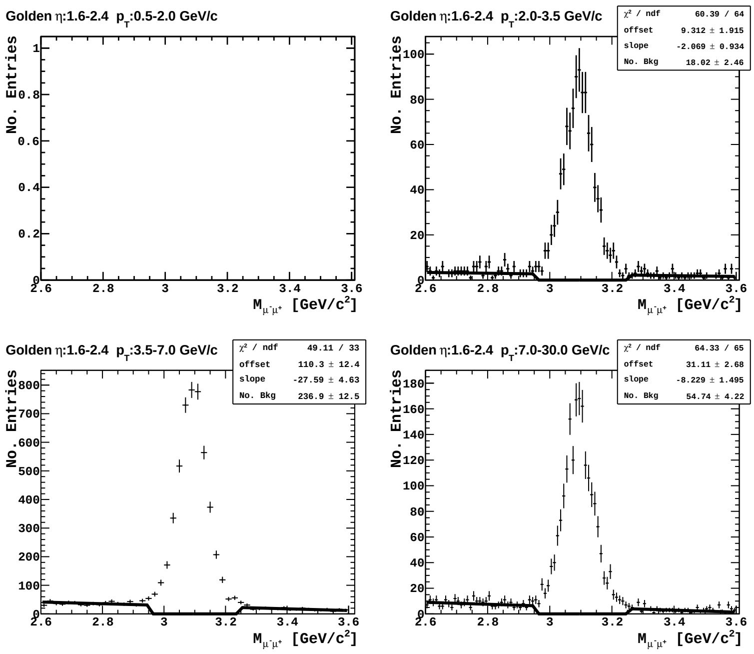

Figure C.17: *Fits used to obtain the standalone and matching efficiency via tag and probe in data.*

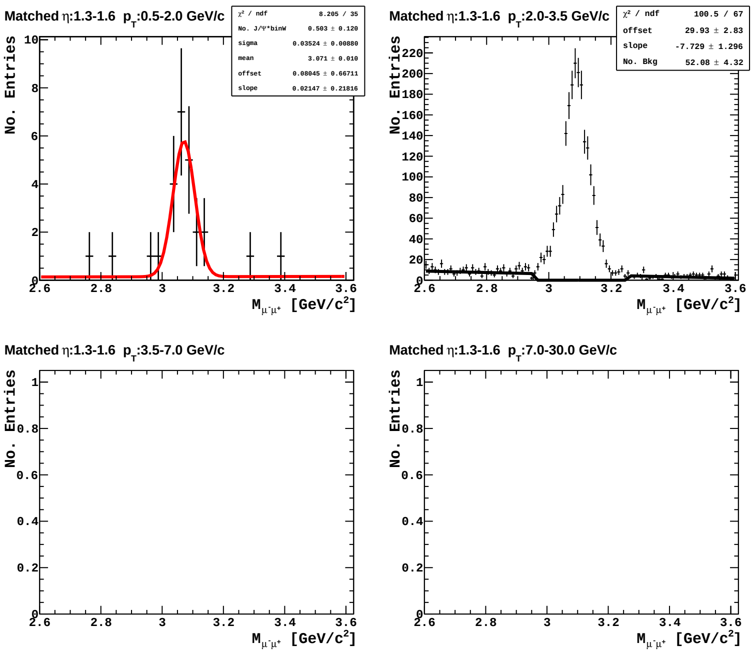

Figure C.18: *Fits used to obtain the standalone and matching efficiency via tag and probe in data.*

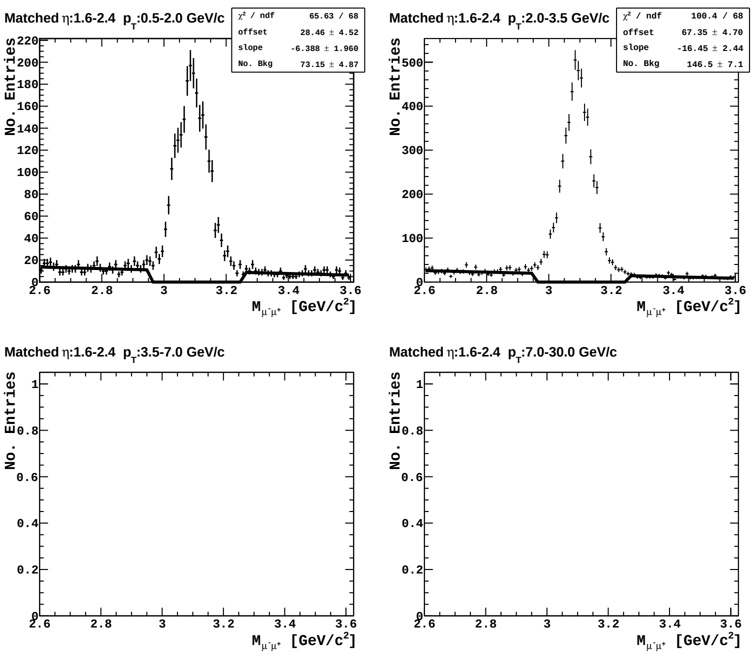

Figure C.19: *Fits used to obtain the standalone and matching efficiency via tag and probe in data.*

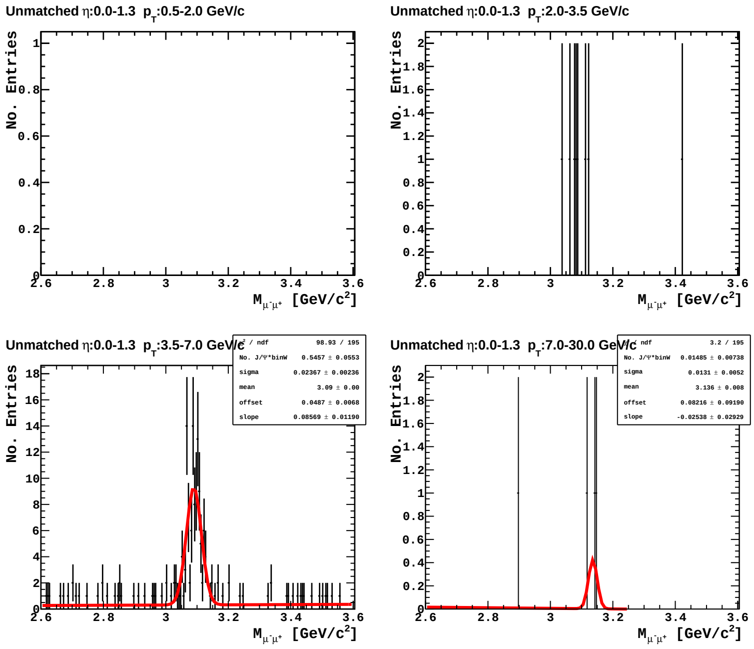

Figure C.20: *Fits used to obtain the standalone and matching efficiency via tag and probe in data.*

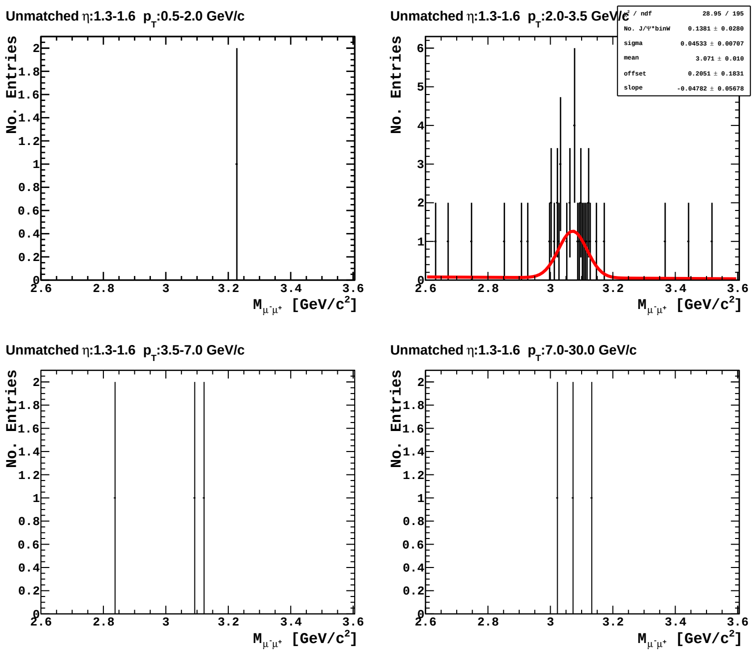

Figure C.21: *Fits used to obtain the standalone and matching efficiency via tag and probe in data.*

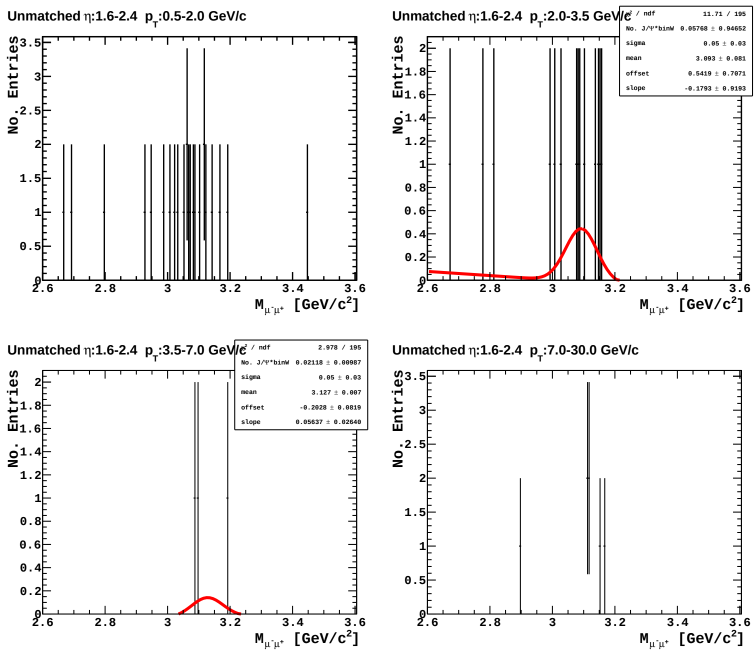

Figure C.22: *Fits used to obtain the standalone and matching efficiency via tag and probe in data.*

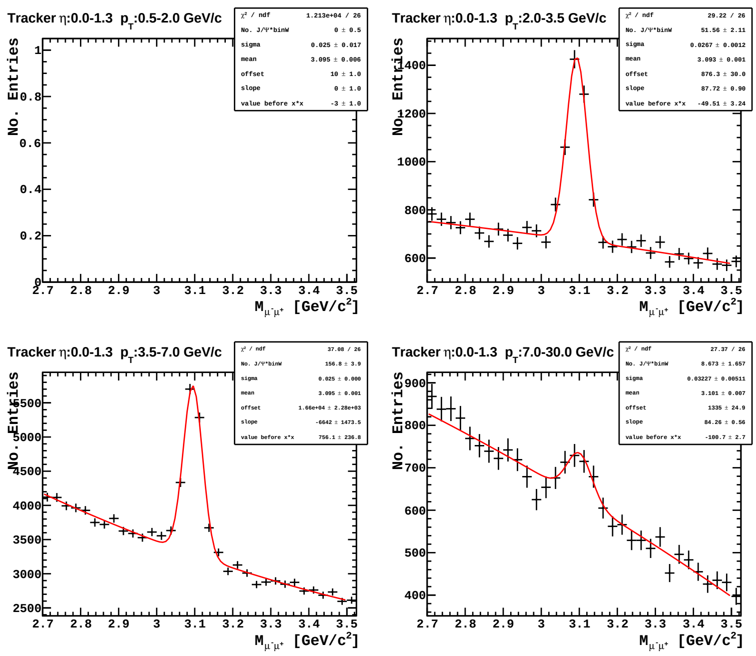

Figure C.23: *Fits used to obtain the standalone and matching efficiency via tag and probe in data.*

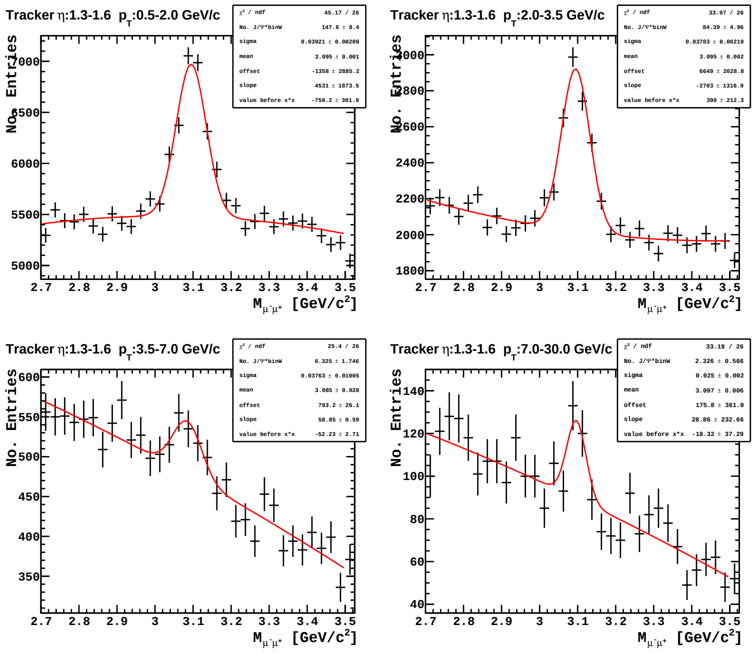

Figure C.24: *Fits used to obtain the standalone and matching efficiency via tag and probe in data.*

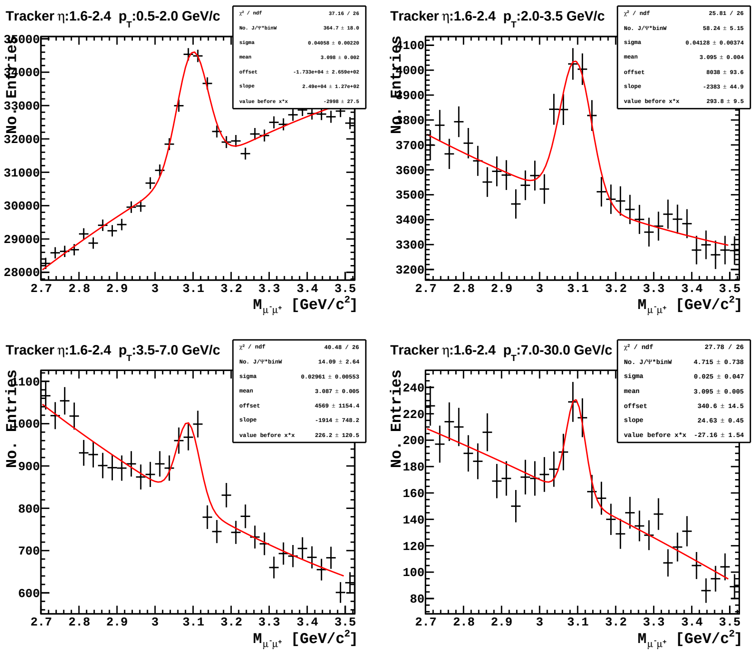

Figure C.25: *Fits used to obtain the standalone and matching efficiency via tag and probe in data.*

D Track Quality Cut Efficiency

The track quality cut efficiency gives the amount of $J/\Psi(1S)$ events, which survive the track quality cuts (see Table 4.2 in Section 4.1.1), divided by the total number of reconstructed $J/\Psi(1S)$ events. This track quality cut efficiency is obtained in the reconstruction efficiency. As a cross check it is also determined here using the tag and probe method. The **tag** muon and the **probe** muon are required to be global and tracker muon objects, where the tag muon fulfills all track quality cuts. The probe has an opposite charge sign compared to the tag muon and the dimuon invariant mass is in a mass window of 1 GeV/c^2 in comparison to the world average value [9]. Additional all kinematical acceptance cuts are required for the probe muon. The **selected probe** for the cut efficiency has to fullfill all track quality cuts.

The result of the cut efficiency is shown in Fig. D.26 in dependence of the p_T of the probe muon. The efficiencies exceed 94 % in all pseudorapidity regions and all transverse momentum bins and is in average around 97 %. A summary of the cut efficiency can also be found in Table D.8. The MC Truth is also shown in Fig. D.26 and deviate in average only by 1 % in comparison to data. The difference between data and MC Truth is taken as a systematic in the cut efficiency in Table D.8.

p_T^{μ} [GeV/c]	$\lvert\eta^{\mu}\rvert < 1.3$	$1.3 < \lvert\eta^{\mu}\rvert < 1.6$	$1.6 < \lvert\eta^{\mu}\rvert < 2.4$
0.5-3.5	94.00 ± 0.24 ± 1.09	96.88 ± 0.06 ± 0.32	95.62 ± 0.033 ± 1.02
3.5-7.0	96.48 ± 0.04 ± 0.74	97.04 ± 0.058 ± 1.00	95.95 ± 0.05 ± 0.24
7.0-10.0	97.93 ± 0.07 ± 0.69	97.19 ± 0.15 ± 0.84	96.34 ± 0.13 ± 0.36
10.0-15.0	97.98 ± 0.12 ± 0.62	97.36 ± 0.26 ± 0.81	96.46 ± 0.24 ± 0.57
15.0-20.0	97.46 ± 0.28 ± 0.96	96.51 ± 0.70 ± 1.51	96.95 ± 0.51 ± 0.75
20.0-30.0	96.96 ± 0.46 ± 1.75	97.68 ± 0.95 ± 0.13	96.01 ± 0.98 ± 0.71
0.5-30.0	96.80 ± 0.25 ± 1.05	97.11 ± 0.50 ± 0.89	96.22 ± 0.47 ± 0.65

Table D.8: *Track quality cut efficiency $\varepsilon_{CUT}(p_T,\eta)$ in % obtained by the tag and probe method for the $J/\Psi(1S)$ resonance in bins of η and p_T of the probe muon, where the first uncertainty is statistical and the second systematical.*

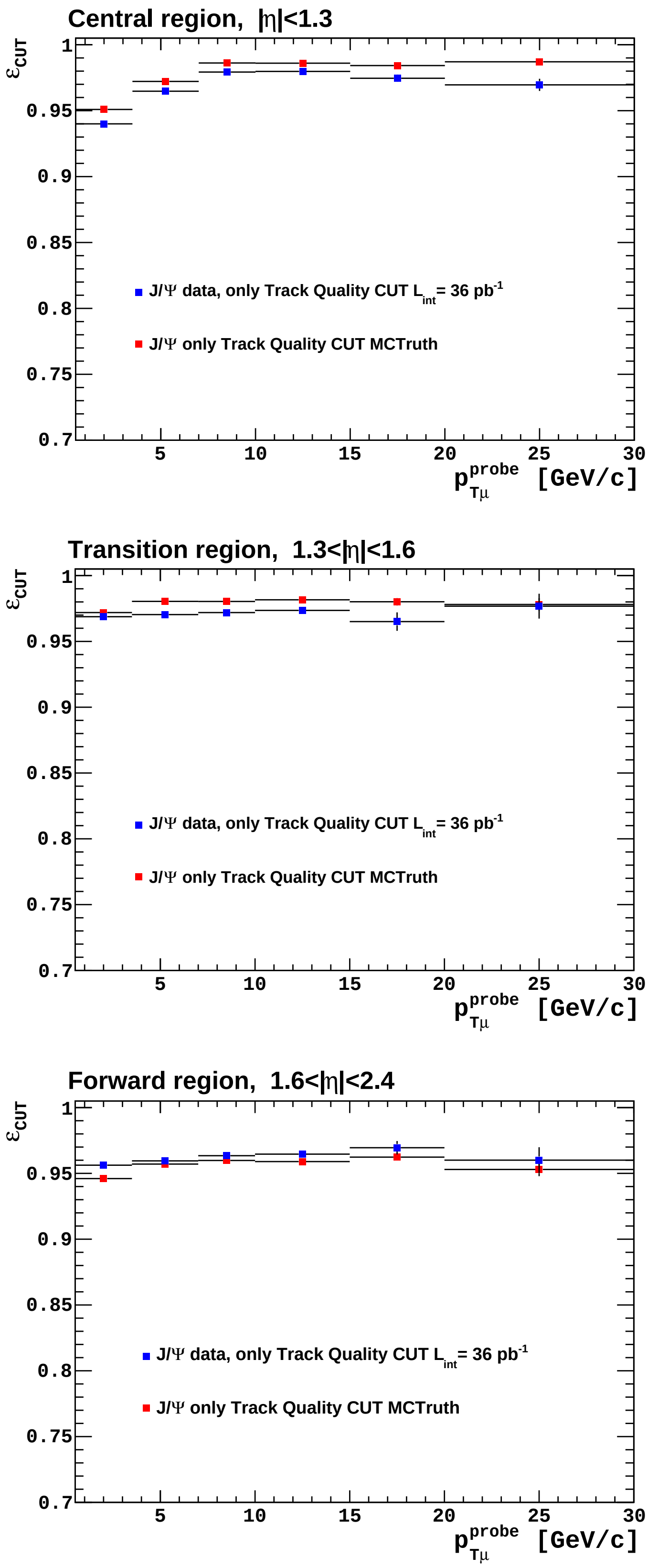

Figure D.26: *Track quality Cut efficiency using the* $J/\Psi(1S)$ *resonance determined by the tag and probe method with 36* pb^{-1} *of CMS compared to MC.*

E Trigger Efficiency

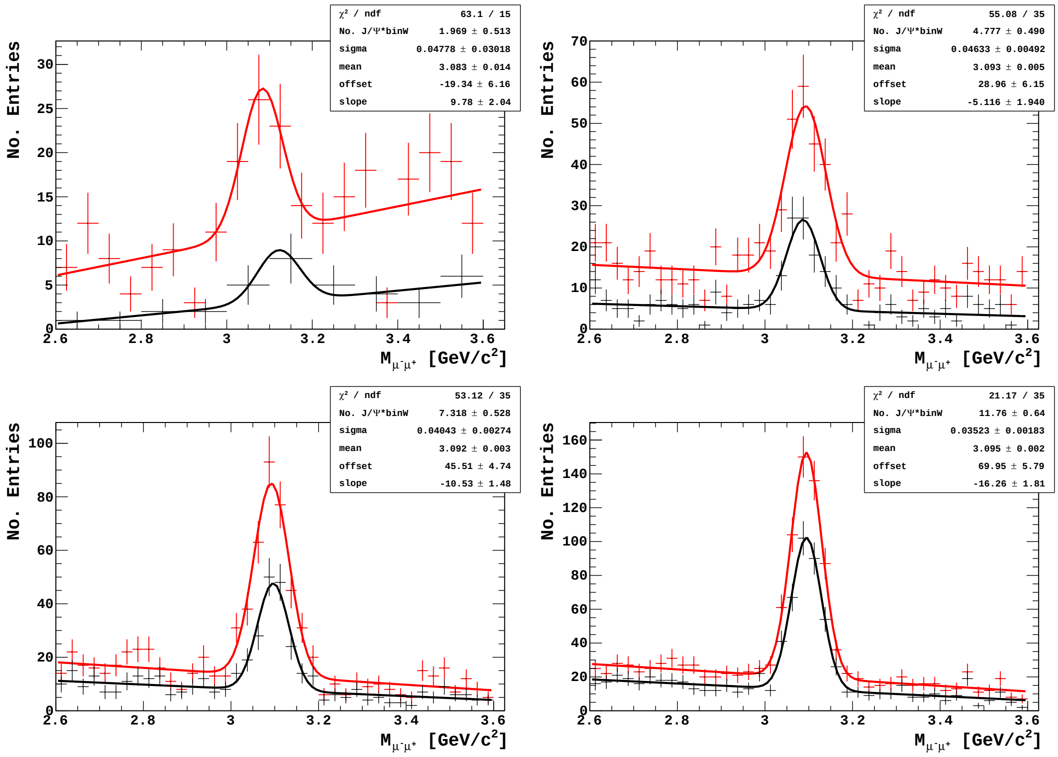

Figure E.27: *Fits used to obtain the* J/Ψ(1S) *trigger efficiency via data for the first four* p_T *bins, where the red points and line refer to the probes and the black ones to the selected probe.*

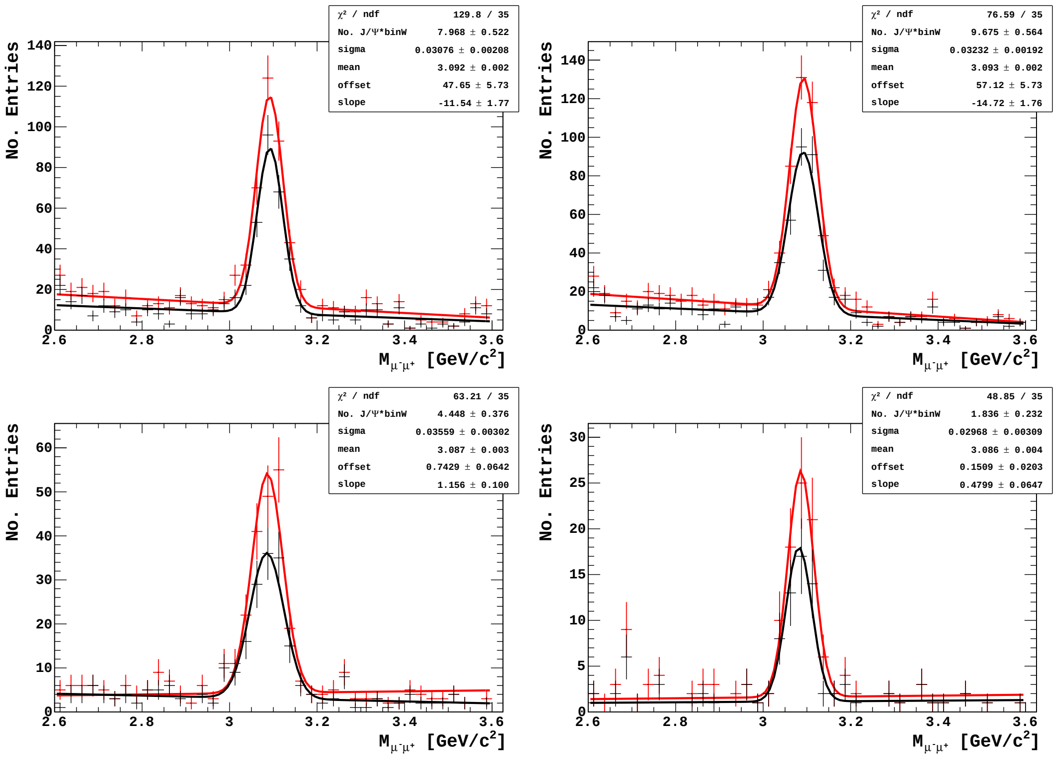

Figure E.28: *Fits used to obtain the* J/Ψ(1S) *trigger efficiency via data for the last four p_T bins, where the red points and line refer to the probes and the black ones to the selected probe.*

F J/Ψ(1S) Cross Section

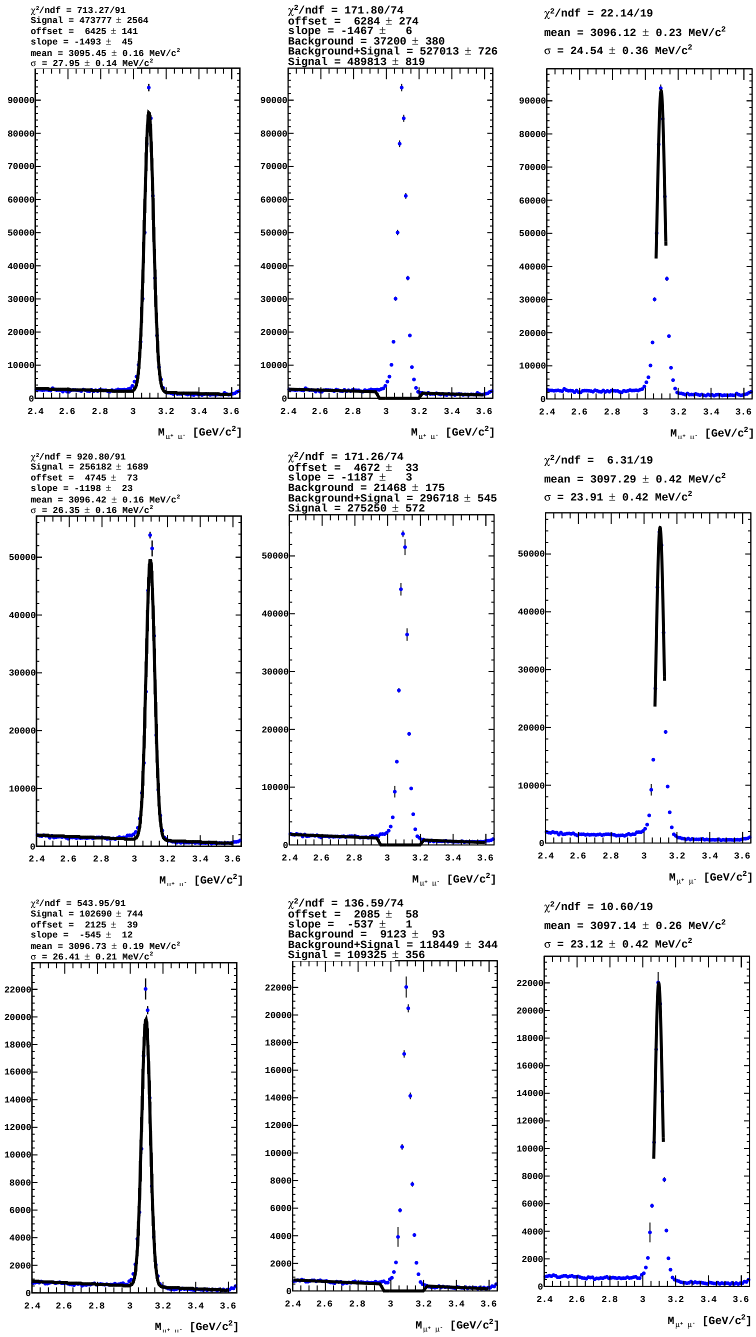

Figure F.29: *Fits used to obtain the* J/Ψ(1S) *inclusive production cross section for* $|y_{J/\Psi(1S)}| <$ 1.3. *In the following* $p_T^{J/\Psi(1S)}$ *bin size order: 8-10-12.5-15*

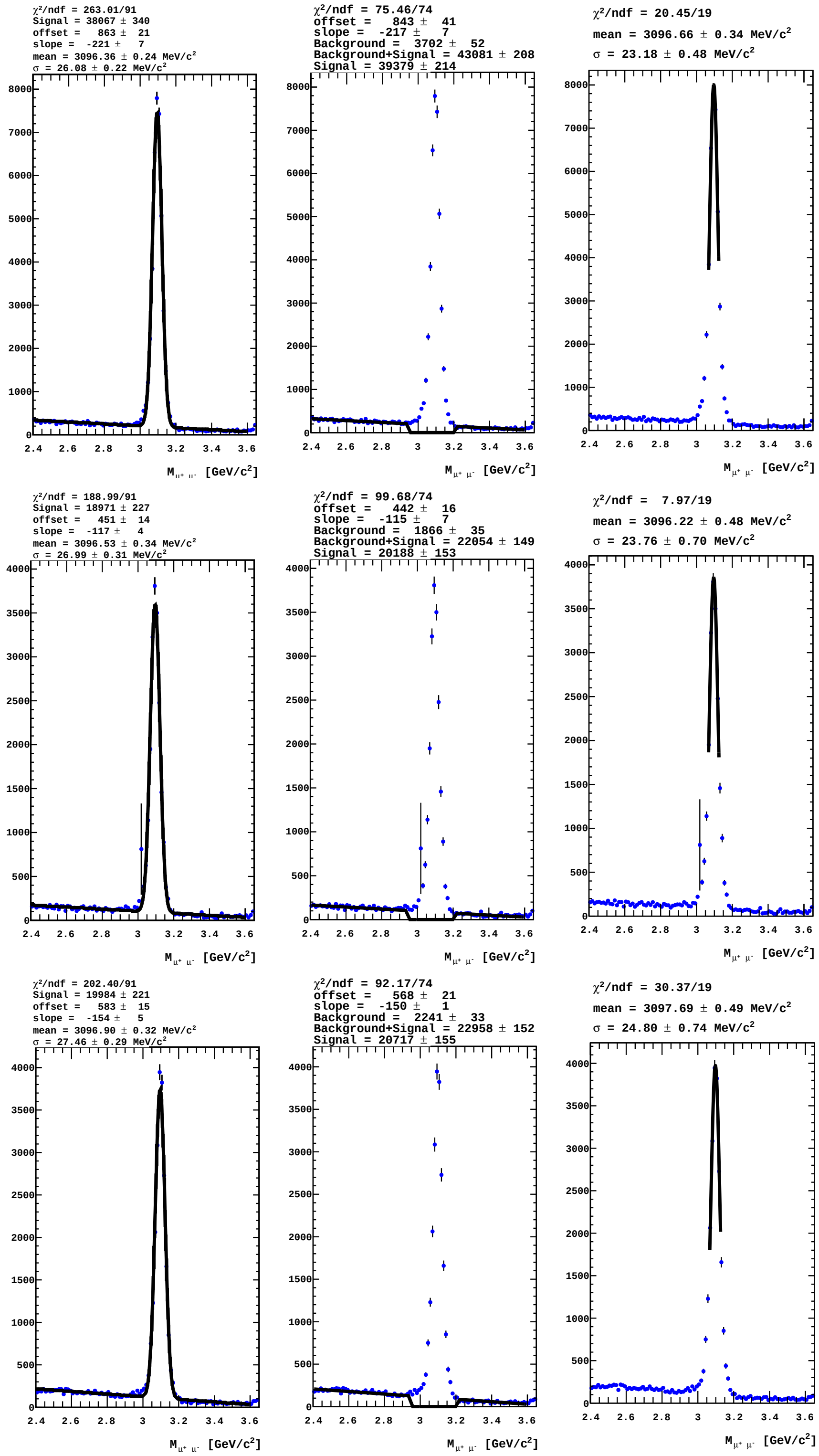

Figure F.30: *Fits used to obtain the* J/Ψ(1S) *inclusive production cross section for* $|y_{\mathrm{J}/\Psi(1\mathrm{S})}| < 1.3$. *In the following* $p_T^{\mathrm{J}/\Psi(1\mathrm{S})}$ *bin size order: 17.5-20-30.*

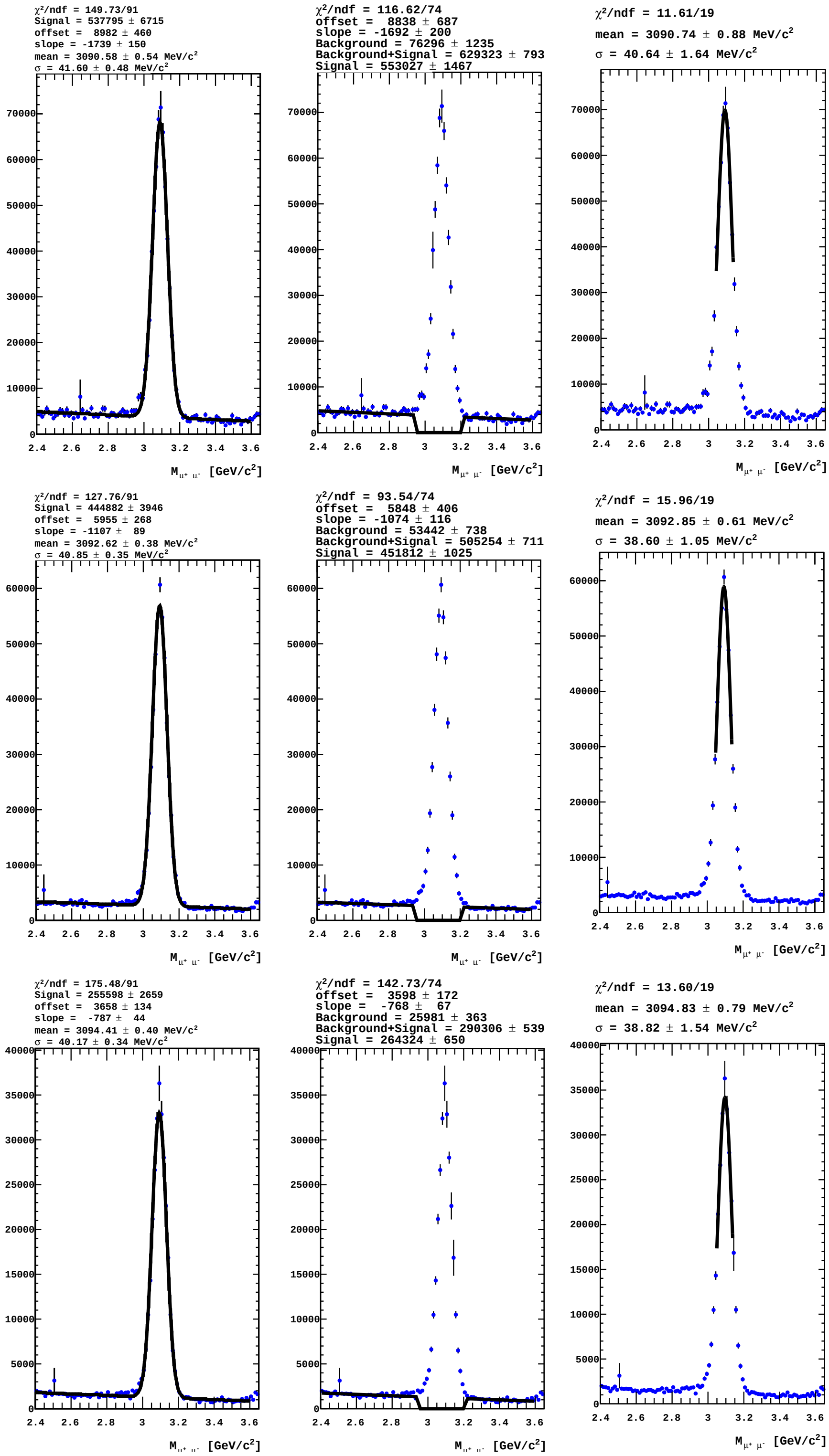

Figure F.31: *Fits used to obtain the* J/Ψ(1S) *inclusive production cross section for* $1.3 < |y_{J/\Psi(1S)}| < 1.6$. *In the following* $p_T^{J/\Psi(1S)}$ *bin size order: 5-6-7-8*

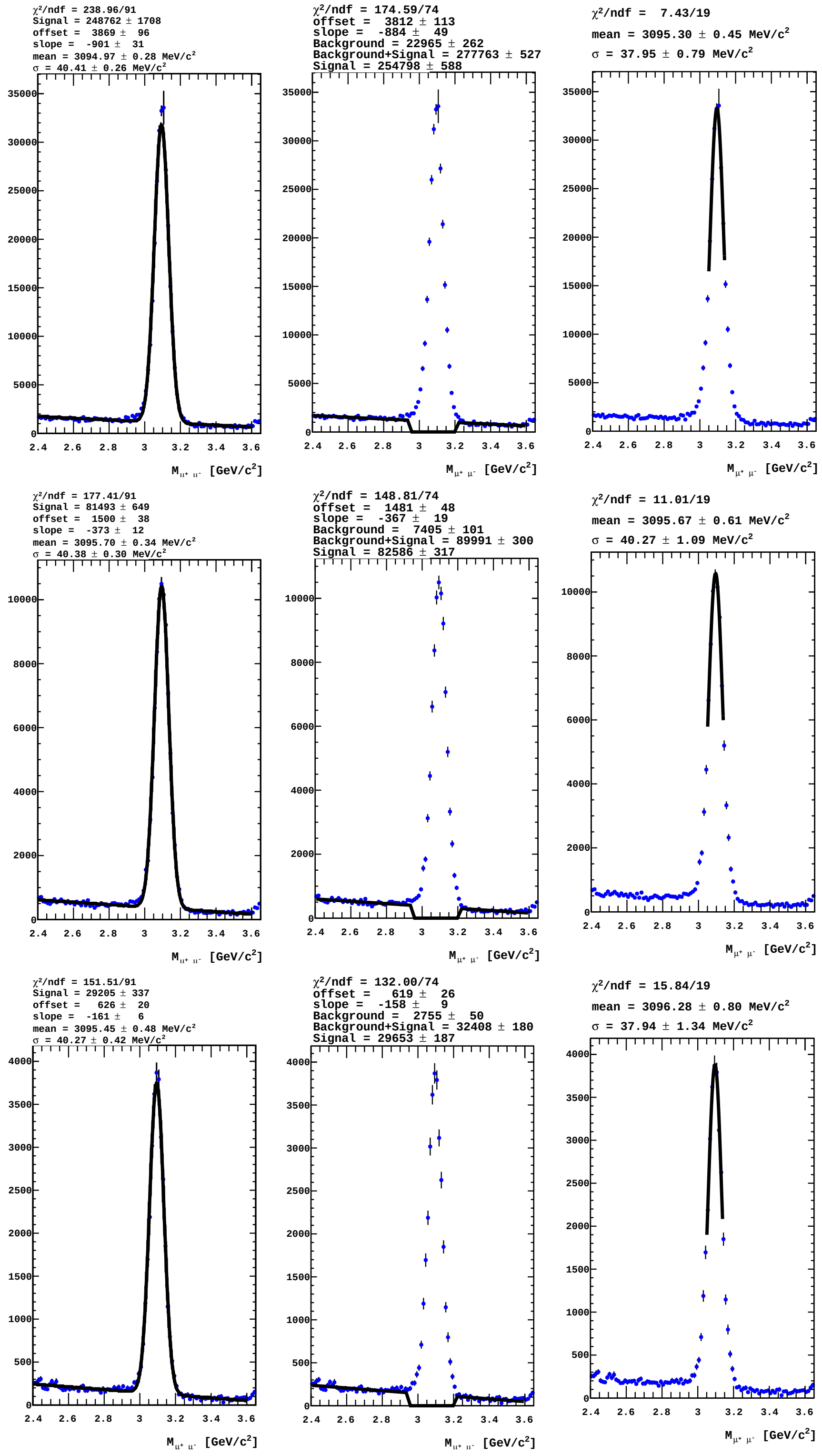

Figure F.32: *Fits used to obtain the* $J/\Psi(1S)$ *inclusive production cross section for* $1.3 < |y_{J/\Psi(1S)}| < 1.6$. *In the following* $p_T^{J/\Psi(1S)}$ *bin size order: 8-10-12.5-15*

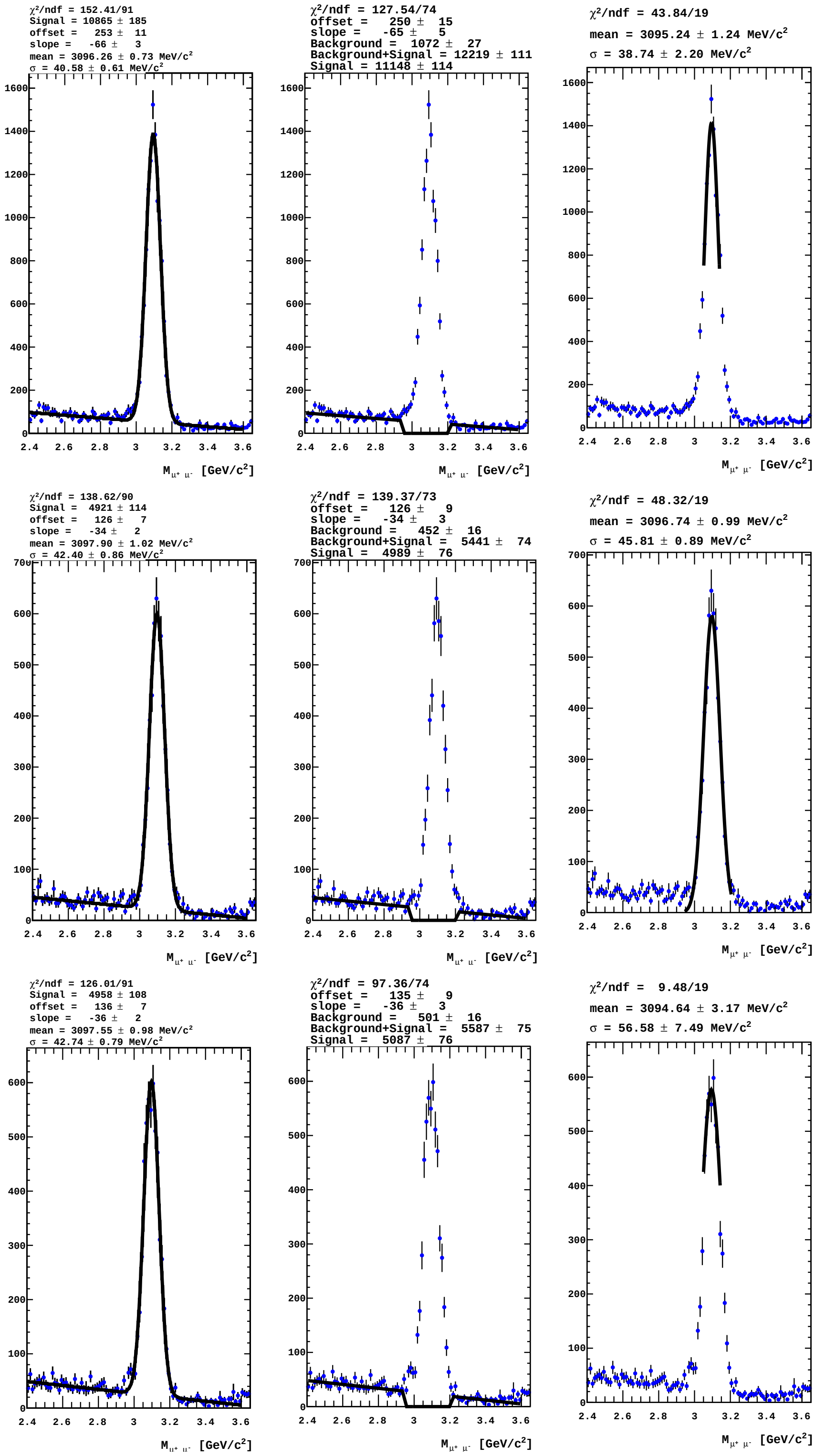

Figure F.33: *Fits used to obtain the* J/Ψ(1S) *inclusive production cross section for* $1.3 < |y_{J/\Psi(1S)}| < 1.6$. *In the following* $p_T^{J/\Psi(1S)}$ *bin size order: 15-17.5-20-30*

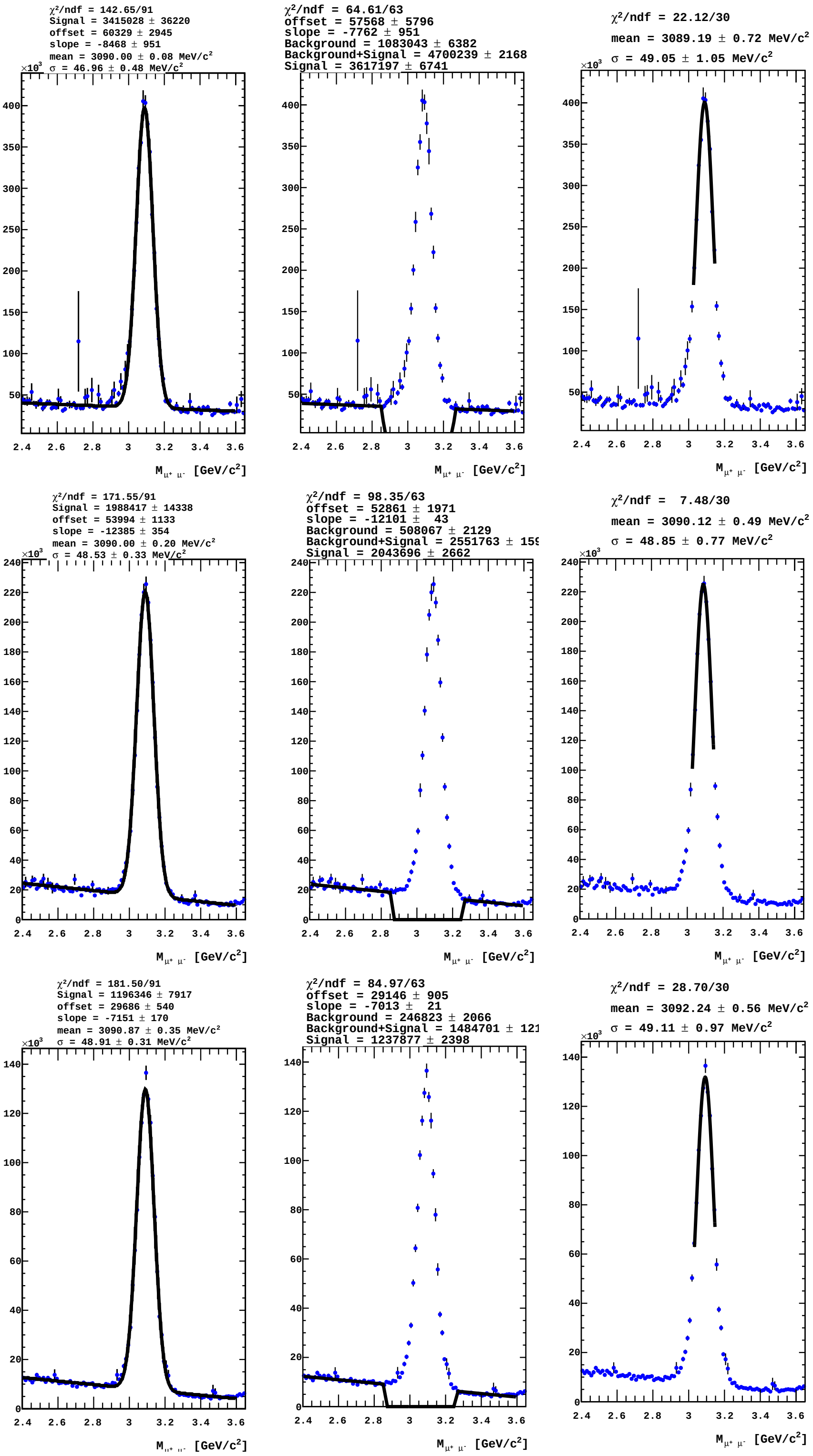

Figure F.34: *Fits used to obtain the* $\mathrm{J}/\Psi(1\mathrm{S})$ *inclusive production cross section for* $1.6 < |y_{\mathrm{J}/\Psi(1\mathrm{S})}| < 2.4$*. In the following* $p_T^{\mathrm{J}/\Psi(1\mathrm{S})}$ *bin size order: 3-4-5-6*

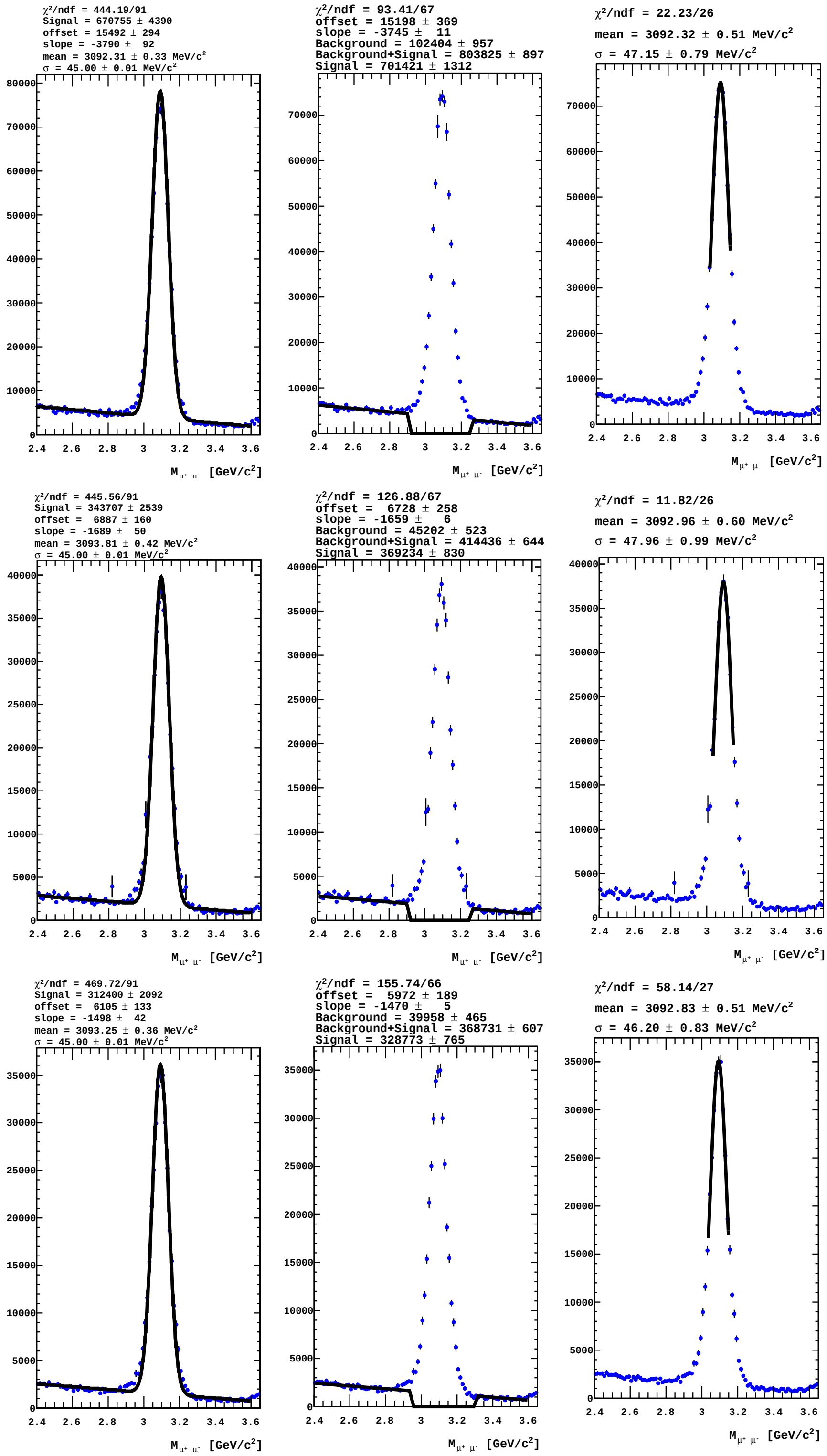

Figure F.35: *Fits used to obtain the* J/Ψ(1S) *inclusive production cross section for* $1.6 < |y_{J/\Psi(1S)}| < 2.4$. *In the following* $p_T^{J/\Psi(1S)}$ *bin size order: 6-7-8-10*

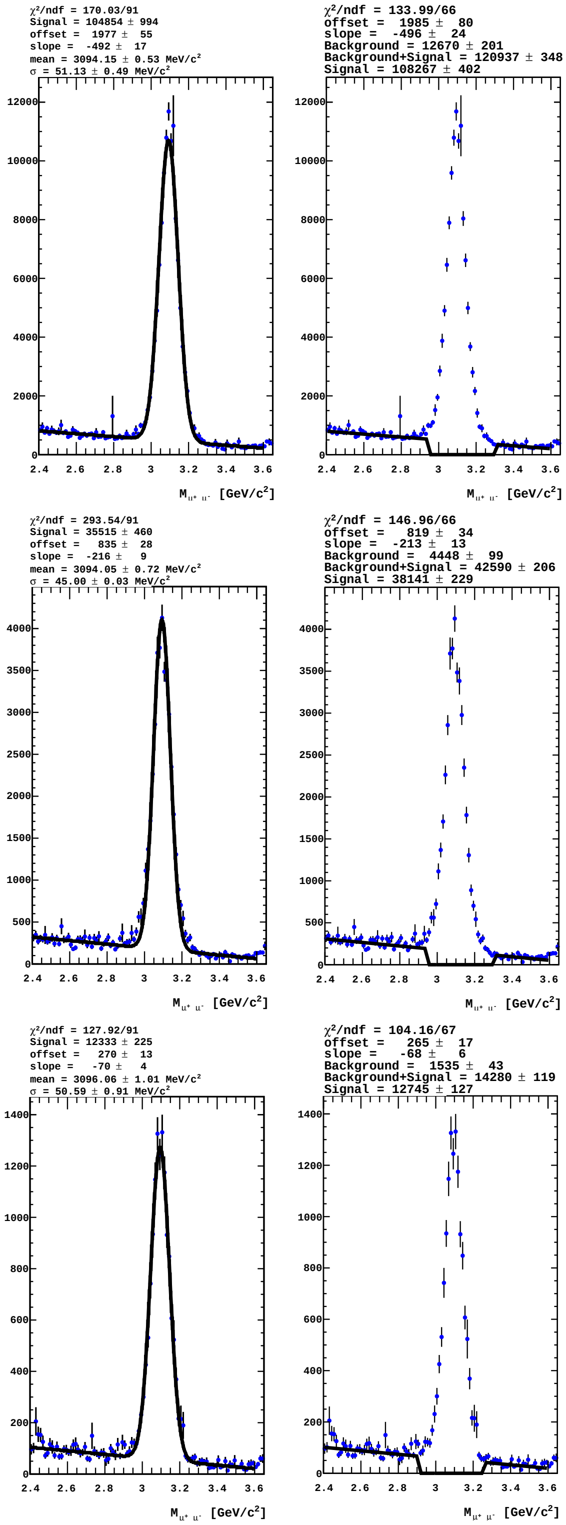

Figure F.36: *Fits used to obtain the* $J/\Psi(1S)$ *inclusive production cross section for* $1.6 < |y_{J/\Psi(1S)}| < 2.4$. *In the following* $p_T^{J/\Psi(1S)}$ *bin size order: 10-12.5-15-17.5*

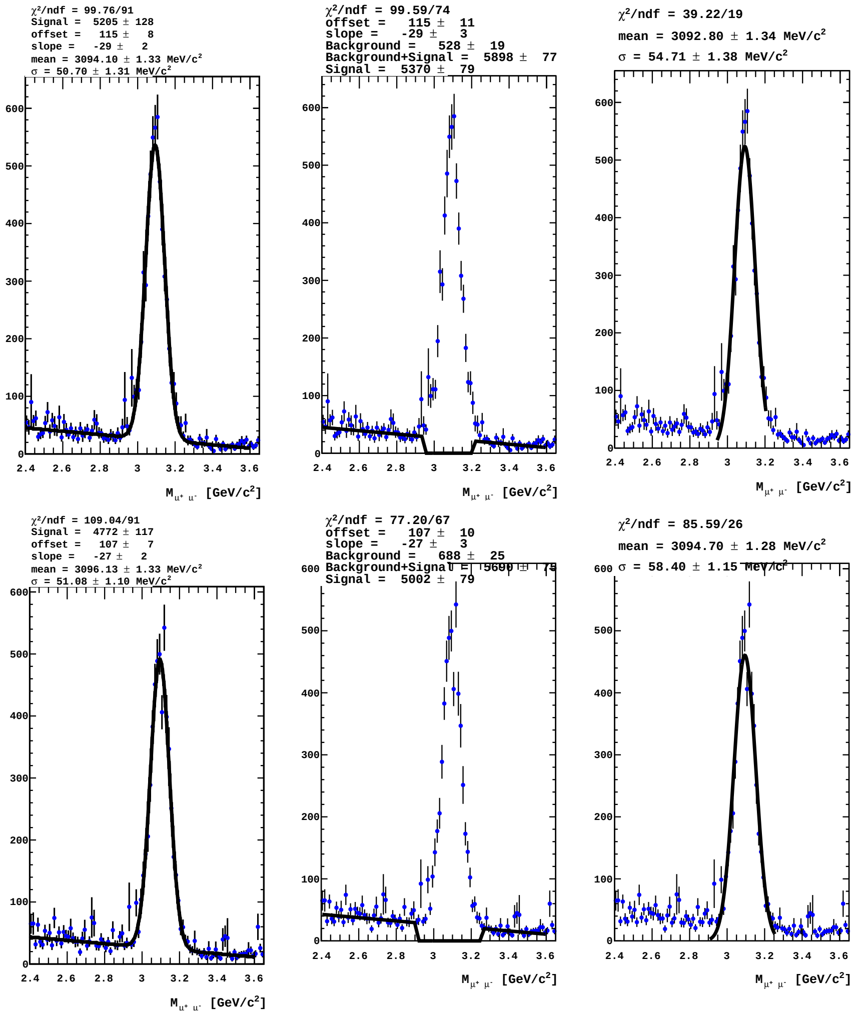

Figure F.37: *Fits used to obtain the* J/Ψ(1S) *inclusive production cross section for* $1.6 < |y_{\mathrm{J}/\Psi(1S)}| < 2.4$. *In the following* $p_T^{\mathrm{J}/\Psi(1S)}$ *bin size order: 17.5-20-30*

G Υ(1S) Cross Section

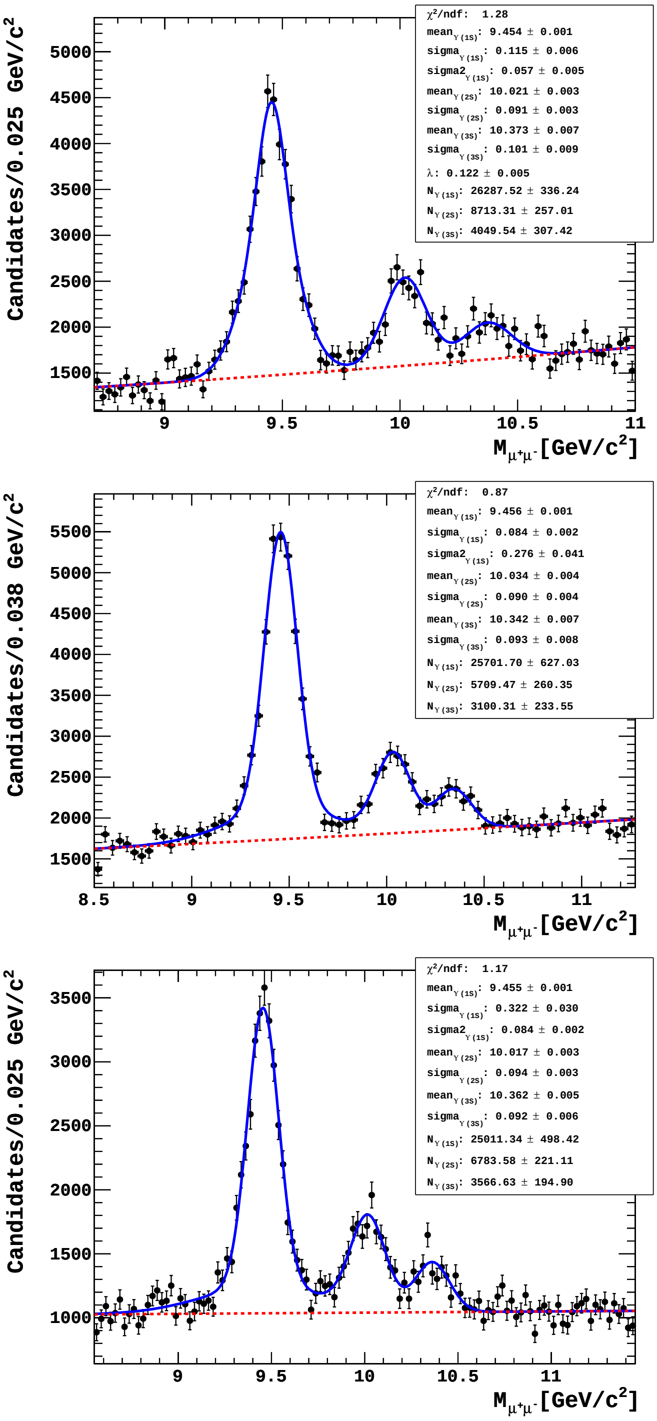

Figure G.38: *Fits used to obtain the* $\Upsilon(1S)$ *production cross section for* $|y_{\Upsilon(1S)}| < 2.0$. *In the following* $p_T^{\Upsilon(1S)}$ *bin size order: 3-4-5-6*

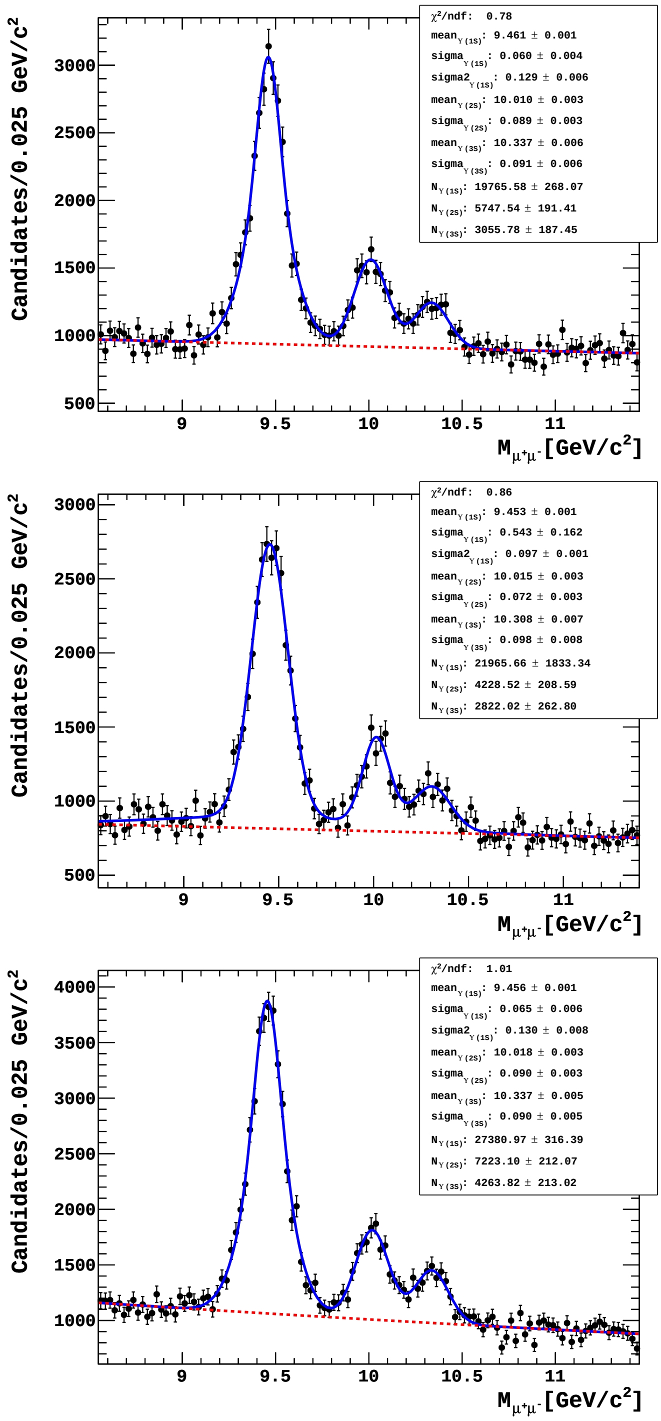

Figure G.39: *Fits used to obtain the* $\Upsilon(1S)$ *production cross section for* $|y_{\Upsilon(1S)}| < 2.0$. *In the following* $p_T^{\Upsilon(1S)}$ *bin size order: 6-7-8-10*

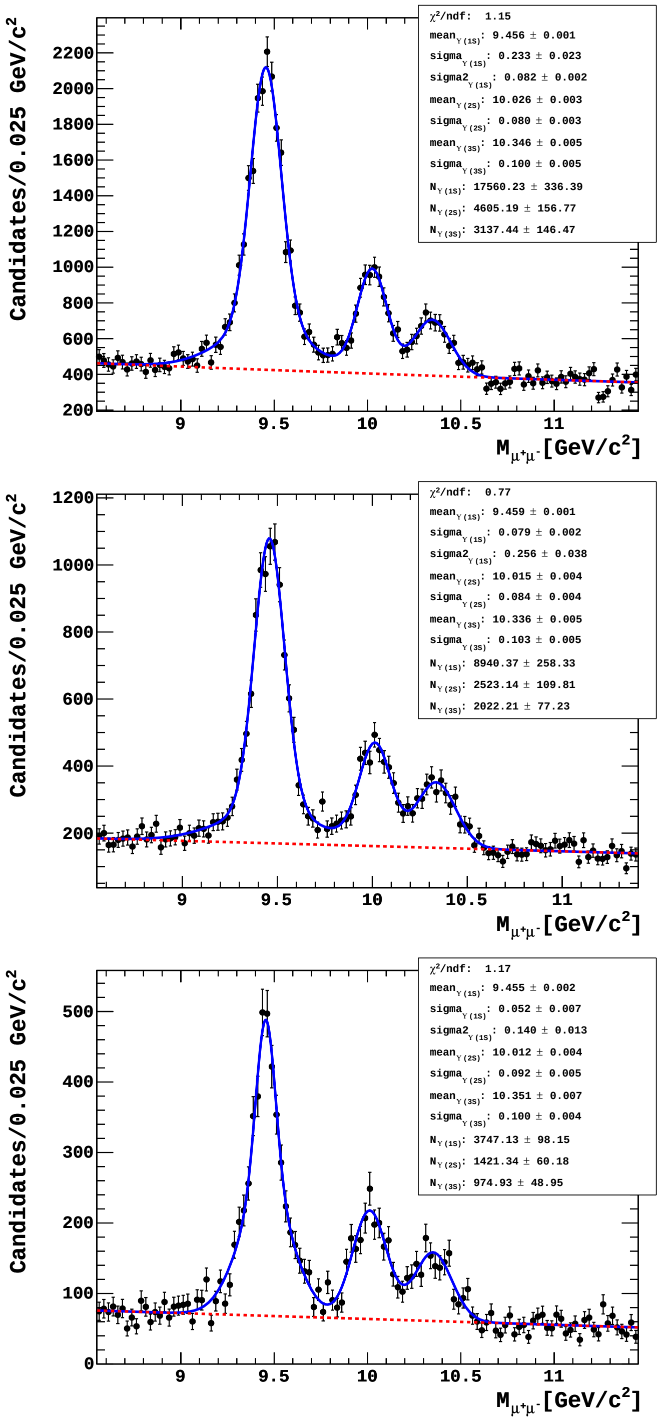

Figure G.40: *Fits used to obtain the* $\Upsilon(1S)$ *production cross section for* $|y_{\Upsilon(1S)}| < 2.0$. *In the following* $p_T^{\Upsilon(1S)}$ *bin size order: 10-12.5-15-17.5*

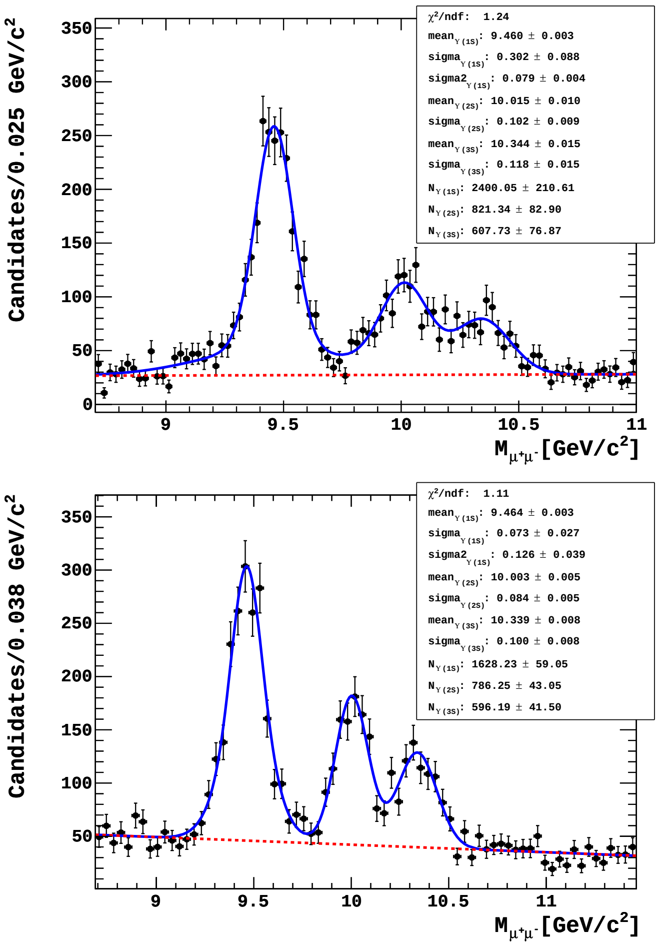

Figure G.41: *Fits used to obtain the* Υ(1S) *production cross section for* $|y_{\Upsilon(1S)}| < 2.0$. *In the following* $p_T^{\Upsilon(1S)}$ *bin size order: 17.5-20-30*

List of Figures

List of Tables

Bibliography

[1] J. J. Aubert et al. Experimental observation of a heavy particle j. *Phys. Rev. Lett.*, 33(23): 1404–1406, Dec 1974. doi: 10.1103/PhysRevLett.33.1404.

[2] J. E. Augustin et al. Discovery of a narrow resonance in e^+e^- annihilation. *Phys. Rev. Lett.*, 33(23):1406–1408, Dec 1974. doi: 10.1103/PhysRevLett.33.1406.

[3] J.D. Bjorken and S.L. Glashow. Elementary particles and su(4). *Phys.Lett.*, 11:255–257, 1964. doi: 10.1016/0031-9163(64)90433-0.

[4] Fred Gilman. The november revolution. In *Tenth Anniversary Symposium of the November revolution - SLAC Beam Line*, 1985.

[5] David Griffiths. *Introduction to Elementary Particle Physics*. 3. Wiley-VCH, 2008.

[6] The CDF Collaboration. j/ψ and $\psi(2s)$ production in $p\bar{p}$ collisions at $\sqrt{s} = 1.8$ tev. *Phys. Rev. Lett.*, 79(4):572–577, Jul 1997. doi: 10.1103/PhysRevLett.79.572.

[7] The CDF Collaboration. Polarizations of j/ψ and $\psi(2s)$ mesons produced in $p\bar{p}$ collisions at $\sqrt{s} = 1.96$ tev. *Phys. Rev. Lett.*, 99(13):132001, Sep 2007. doi: 10.1103/PhysRevLett.99.132001.

[8] Pietro Faccioli et al. Towards the experimental clarification of quarkonium polarization. *The European Physical Journal C - Particles and Fields*, 69:657–673, 2010. ISSN 1434-6044. URL http://dx.doi.org/10.1140/epjc/s10052-010-1420-5. 10.1140/epjc/s10052-010-1420-5.

[9] K. Nakamura et al. (Particle Data Group). Jpg 37, 075021, 2010. URL http://pdg.lbl.gov.

[10] E. Eichten and K. Gottfried. Heavy Quarks in e+ e- Annihilation. *Phys.Lett.*, B66:286, 1977. doi: 10.1016/0370-2693(77)90882-6.

[11] S. W. Herb et al. Observation of a dimuon resonance at 9.5 gev in 400-gev proton-nucleus collisions. *Phys. Rev. Lett.*, 39(5):252–255, Aug 1977. doi: 10.1103/PhysRevLett.39.252.

[12] Geoffrey T. Bodwin et al. Rigorous QCD analysis of inclusive annihilation and production of heavy quarkonium. *Phys.Rev.*, D51:1125–1171, 1995. doi: 10.1103/PhysRevD.51.1125,10.1103/PhysRevD.55.5853.

[13] Nora Brambilla et al. *Heavy Quarkonium Physics.* CERN, Geneva, 2005.

[14] Michael Kramer. Quarkonium production at high-energy colliders. *Prog.Part.Nucl.Phys.*, 47:141–201, 2001. doi: 10.1016/S0146-6410(01)00154-5.

[15] The CDF Collaboration. υ production and polarization in $p\bar{p}$ collisions at $\sqrt{s} = 1.8\ tev$. *Phys. Rev. Lett.*, 88(16):161802, Apr 2002. doi: 10.1103/PhysRevLett.88.161802.

[16] The D0 Collaboration. Measurement of inclusive differential cross sections for $\upsilon(1s)$ production in $p\bar{p}$ collisions at $\sqrt{s}$ = 1.96 tev. *Phys. Rev. Lett.*, 94:232001, 2005. doi: 10.1103/PhysRevLett.94.232001.

[17] CERN. Big science: The lhc in pictures, 2008. URL `http://bigscience.web.cern.ch/bigscience/en/lhc/lhc2.html`.

[18] The CMS Collaboration. Cms luminosity for 2010 collision data, 2010. URL `https://twiki.cern.ch/twiki/bin/view/CMSPublic/LumiPublicResults2010`.

[19] The CMS Collaboration. Cms physics technical design report, volume i: Detector performace and software. 2006. CERN-LHCC-2006-001.

[20] Rancoita P. G. Leroy Claude. *Principles of radiation interaction in matter and detection.* World Scientific, 2004.

[21] R. Brauer et al. Design and test beam performance of substructures of the CMS tracker end caps. CERN-CMS-NOTE-2005-025.

[22] J Ying et al. Study of an avalanche-mode resistive plate chamber. *J. Phys. G: Nucl. Part. Phys*, 26:1291,1298, 2000.

[23] The CMS Collaboration. Quarkonium studies with cms, . URL `https://twiki.cern.ch/twiki/bin/view/CMS/Quarkonia`.

[24] The CMS Collaboration. Muon reconstruction in the cms detector. *CMS AN 2008/097*, 2009.

[25] The CMS Collaboration. Swguidetrackermuons - update to cms analysis note 2008/097, . URL `https://twiki.cern.ch/twiki/bin/view/CMSPublic/SWGuideTrackerMuons`.

[26] Hermine K. Woehri et al. Cms meeting: Quarkonium wg meeting on efficiencies, 14 January 2011. URL http://indico.cern.ch/conferenceDisplay.py?confId=121619.

[27] The CMS Collaboration. Measurement of cms luminosity. *CMS PAS EWK-10-004*, 2010.

[28] S. Agostinelli et al. GEANT4: A simulation toolkit. *Nucl. Instrum. Meth.*, A506:250–303, 2003. doi: 10.1016/S0168-9002(03)01368-8.

[29] The CMS Collaboration. Fall 2010 cms montecarlo production (7 tev), 2010. URL https://twiki.cern.ch/twiki/bin/viewauth/CMS/ProductionFall2010.

[30] Carlos Lourenco. Cms trigger reviews meeting: Bph triggers, 30. November 2010. URL http://indico.cern.ch/conferenceDisplay.py?confId=114007.

[31] The CMS Collaboration. Muon identification in cms. *CMS AN-2008/098*, 2008.

[32] The CMS Collaboration. Measurement of momentum scale and resolution using low-mass resonances and cosmic ray muons. *CMS PAS TRK-10-004*, 2010.

[33] The CMS Collaboration. muon momentum scale calibration and momentum resolution fit, February 2011. URL https://twiki.cern.ch/twiki/bin/view/CMS/MuonScaleCalib.

[34] The CMS Collaboration. Cms quarkonium task force workspace, 2010. URL https://espace.cern.ch/cms-quarkonia/default.aspx.

[35] The CMS Collaboration. Towards a measurement of the inclusive $w \to \mu\nu$ and $z \to \mu^+\mu^-$ cross sections in pp collisions at $\sqrt{s}$ =14 tev. *CMS AN-2007/031*, 2008.

[36] The CMS Collaboration. J/psi prompt and non-prompt cross sections in pp collisions at $\sqrt{s} = 7$ tev. 2010. CMS-PAS-BPH-10-002.

[37] The CMS Collaboration. Upsilon production cross section in pp collisions at $\sqrt{s}$=7 tev. March 2011. arXiv:1012.5545.

[38] M. Butenschoen and B. Kniehl. J/psi production with nrqcd: Hera, tevatron, rhic and lhc. 2010. arXiv:1011.5619v1.

[39] Prof. Dr. Kuang-Ta CHAO Department of Physics Peking University China. Private communication, 2011.

Acknowledgement

First of all, I would like to thank my advisor, Prof. Dr. Stefan Schael for making this thesis possible and for guiding me through the process of the completion of this thesis. His enthusiasm for particle physics is inspiring.

Furthermore, I thankfully acknowledge Prof. Dr. Lutz Feld for being my co-corrector.

I am also truly grateful for the help, guidance and commitment of my supervisor Dr. Adrian Perieanu, whose consistent optimism always kept me going.

My sincere thanks goes to the whole CMS IB analysis team for their support and help - namely Dr. Giorgos Anagnostou, Natalie Heracleous, Otto Hindrichs, Dr. Andrei Ostapchuk, Dr. Dimitris Pandoulas, Dr. Adrian Perieanu, Prof Dr. Frank Raupach, Prof Dr. Stefan Schael, Hendrik Weber and Dr. Bruno Wittmer. The friendly atmosphere makes it a pleasure to be part of this team.

I would like to express my gratitude to the Quarkonian Working Group of the CMS Collaboration, especially Prof. Dr. Ian Shipsey, Dr. Nuno Leonardo and Dr. Fabrizio Palla, for giving me the opportunity to participate in their analysis even though I was just starting to work at the CMS experiment.

My special thanks goes to Bastian Beischer and Hendrik Weber for a lot of fruitful discussions and being such great office-mates.

I also express many thanks to the 11-45 Mensa crew, who make my lunch breaks a really enjoyable and distracting time.

Moreover I would like to thank my friends and fellow students Anja König, Alex Cozub-Poetica, Armin Böhmer, Daniel Gebauer and André Hoffmann for being at my side during these 5 years of physics studies.

Finally, I would like to sincerely thank my family and friends for believing in me, supporting and loving me.

Eidesstattliche Erklärung

Hiermit versichere ich gemäß 19 Abs. 6 DPO 2002, die vorliegende Arbeit selbständig verfasst und keine anderen als die angegebenen Quellen und Hilfsmittel benutzt, sowie Zitate kenntlich gemacht zu haben.

Aachen, 12.04.2011